Max Planck Institute for Solid State Research
Stuttgart University, Faculty of Chemistry

Application of In Situ X-ray Powder Diffraction in Solid State Processes Visualization

Tomče Rünčevski

Stuttgart, 2014

Application of In Situ X-ray Powder Diffraction in Solid State Processes Visualization

Von der Fakultät Chemie der Universität Stuttgart zur Erlangung der Würde eines Doktors der Naturwissenschaften (Dr. rer. nat.) genehmigte Abhandlung

Vorgelegt von

Tomče Runčevski

aus Bitola, Mazedonien

Hauptberichter:	Prof. Dr. R. E. Dinnebier
Mitberichter:	Prof. Dr. Th. Schleid
Mitprüfer:	Prof. Dr. S. Laschat

Tag der mündlichen Prüfung: 05. August 2014

Max-Planck-Institut für Festkörperforschung, Stuttgart

2014

Erklärung über die Eigenständigkeit der Dissertation

Ich versichere, dass ich die vorliegende Arbeit mit dem Titel „Application of *In Situ* X-ray Powder Diffraction in Solid-State Processes Visualization“ selbständig verfasst und keine anderen als die angegebenen Quellen und Hilfsmittel benutzt habe; aus fremden Quellen entnommene Passagen und Gedanken sind als solche kenntlich gemacht.

Tomče Runčevski Stuttgart, 17. June 2014

Declaration of Authorship

I hereby certify that the dissertation entitled “Application of *In Situ* X-ray Powder Diffraction in Solid-State Processes Visualization” is entirely my own work except where otherwise indicated. Passages and ideas from other sources have been clearly indicated.

Tomče Runčevski Stuttgart, 17. June 2014

Preface

X-ray powder diffraction is as a powerful tool for structural analysis of crystalline compounds which do not grow as single crystals, but a polycrystalline bulk. When applied under non-ambient conditions, or when data are collected at consecutive time intervals, X-ray powder diffraction can be readily turned into a valuable method for *in situ* following, visualizing and ultimately explaining a number of solid state processes and chemical reaction. In the scope of my PhD work, an attempt to demonstrate the power and applicability of *in situ* X-ray powder diffraction in studying the reactivity of the solid state was made. In a period of almost 3 years, various systems were investigated when submitted under different external stimuli to initiate specific process and/or reaction in the solid state. The results described in this thesis were done working on six (independent) research projects, presented herein as separate case studies. (It should be noted that in parallel to the work performed on these six projects, research was done in several other topics, part of which is already published in scientific journals and the references are given in CV, attached at the end of the thesis).

Посветено на тато, мама и Кате.

Acknowledgements

The research results presented in this thesis would not have been possible without the help of certain people, to whom I am gratefully thankful.

It was my supervisor, Prof. Dr. Robert E. Dinnebier, who introduced me to the field of powder diffraction and guided me in learning, critically thinking and solving problems. He gave me the chance to work on my own ideas and thought me how to realize them properly. For his continuous support, and for providing me with truly friendly and comfortable working environment, I am sincerely grateful.

I thank the members of the examination committee, Prof. Dr. Thomas Schleid and Prof. Dr. Sabine Laschat, for the evaluation of my Ph.D. thesis.

I would not be able to obtain many of the presented results without the fruitful collaboration with several research groups: many thanks go to Prof. Dr. Panče Naumov, Prof. Dr. Diego Sampedro, Prof. Dr. Petre Makreski and Dr. Gjorgji Petruševski, and all of other researchers mentioned and acknowledged at the end of each case study.

I acknowledge the members of scientific service group diffraction, Mr. Frank Adams, Ms. Christine Stefani, Dr. Melanie Müller, Dr. Oksana Magdysyuk and Mr. Martin Etter for their help and support. I am thankful for the help from my colleagues and friends Ms. Andrea Knöller, Ms. Nina Stitz and Ms. Katharina Kress.

I thank Ms. Sabine Paulsen and Ms. Brigit King for their help concerning administrative matter and Dr. Hans-Georg Libuda for introducing me to the IMPRS-AM.

Content

Appendix: Curriculum Vitae

1. Introduction

In view of the need to understand the features of crystalline matter, precise knowledge of its crystal structure stands at the frontier of solid state research. Nowadays, crystal structure determination based on diffraction by single crystals is brought to a level of advance that it could be argued that it is indeed a routine practice. (1) Nevertheless, there are numerous cases where good-quality single crystals are unattainable and the material crystallizes in form of a microcrystalline bulk. In cases as such, X-ray powder diffraction (XRPD) is the remaining alternative for structural studies. Besides revealing the geometrical structure of matter at atomic scale, XRPD provides plethora of information on the microstructure. In addition, as it probes the bulk of materials rather than a single crystal, it is a suitable method for quantitative studies of phase mixtures. Providing information on the crystal structure, microstructure and phase composition, XRPD is among the most powerful structural methods ever developed. (2)

Although the importance of XRPD in solid state chemistry and physics was readily recognized after its discovery, theis technique was rather sporadically used. The main reason for that was (and still is) the thorny way of data analysis. Unlike the case of single crystal (X-ray) diffraction, the random orientation of microcrystals in powder samples leads to the intrinsic problem of the method – accidental and systematic peak overlap caused by the fact that the 3D reciprocal lattice of the structure collapses onto a 1D diffraction pattern, significantly reducing the amount of the experimentally obtainable information. The peaks overlap is a challenging problem, yet there are many insightful strategies to get it overcome. The major developments in the field came in the second part of the 20th century with the progress in instrumentation for data collection (with new high-resolution diffractometers which reduce the accidental peak overlap), the discovery of digital computers (which heavily aided data manipulation and analysis), and the introduction of the revolutionary Rietveld refinement method (used for refining complicated, low symmetry crystal structures). (2) Thereafter, XRPD became a fast developing research field and it expanded to more exciting and challenging studies than phase analyses and simple crystal structure refinements.

The possibility of performing diffraction experiments under non-ambient conditions was also recognized at the very beginnings of the method. In 1921, Westgren collected diffraction data of iron and steel up to a temperature of 1273 K, (3a) whether Vegard (1929) performed XRPD study on α-N_2 at remarkably low temperature of 34 K. (3b) It is clear that XRPD data can be collected not only under different temperature, but also under other non-ambient conditions, including pressure, radiation, mechanical grinding and milling, drying, among others. (4) Similarly, in case of a reacting system (for example a slow solid-state reaction), powder diffraction data can be collected at consecutive time-points on the reaction course. Every diffraction pattern collected at a different (non-ambient) condition or at a different time-point contains information on the crystal structure(s) present in the system, the microstructure(s) and the relative phase composition of the sample. By analysing the changes of the scattered intensity, one can identify and observe the structural changes of matter (qualitative analysis) and the changes of their phase amounts (quantitative analysis), thus the mechanistic picture (how the atoms move) and the kinetic picture (how the phase quantity changes) become readily available. For that reason, *in situ* XRPD is a technique that comes nicely at hand in following, visualizing and observing diverse physical processes and chemical reactions happening in the solid state.

As mentioned before, the evident gain in popularity of *in situ* XRPD in the last few decades relays heavily on recent advances in instrumentation, especially in better radiation sources (new-generation synchrotrons and improved laboratory X-ray sources) and high-sensitivity X-ray detectors. (2) For a successful *in situ* XRPD experiment three experimental conditions should be met: high intensity (which translates in high scanning speed), high resolution (which allows tackling of structural details) and high energy (which permits sufficient penetration depth of radiation in the reaction chambers). In line with the technical developments, new strategies and methods for data analysis were derived and successfully applied. The Rietveld refinement method made the analysis of complicated patterns possible. Novel approaches for *ab initio* structure solution from powder diffraction data were introduced, for example the simulated annealing method, applicable for solving the crystal structures of big and complicated organic molecules. (2) The realization of these methods in user-friendly software eased the application of (*in situ*) XRPD, for example in the program suite TOPAS (which was almost exclusively used in this work). (5) The advances of these triggers of *in situ* XRPD are shortly reviewed in the second part of this Thesis: *in situ XRPD Data Collection and Analysis*.

In situ XRPD is a suitable technique for studying various systems undergoing different chemical reactions and physical processes when subjected to different external stimuli. To explore the versatility of the method, the chemical systems within the case studies presented in this thesis were chosen to be as diverse as possible, ranging from inorganic cementitious phases to organic molecules, from organometallics to pharmaceutically active compounds. Three processes were in the centre of attention: temperature induced dehydrations, photoinduced chemical reactions and polymorphic phase transformations. The data analyses revealed the underlying mechanistic pictures of these processes and the kinetic rates of the reactions. Detains on each case study are given in the third part: *Case Studies of Application of in situ XRPD*.

The *Conclusion* of the thesis points to the fact that *in situ* XRPD is indeed a powerful technique for structural investigations, qualitative as well as quantitative, in various fields in the realm of solid state sciences.

2. *In Situ* XRPD Data Collection and Analysis

2.1. Instrumentation for *In Situ* XRPD

XRPD data are collected in a very simple and convenient fashion – the scattered X-ray intensity is measured and plotted against a single independent variable, the 2θ Bragg angle. In the early days, XRPD data were recorded on X-ray films using variety of cameras and each film contained a series of concentric ring segments corresponding to one or more Bragg peaks. Today the film-technique (which is with undeniable historical significance) is completely replaced by powder diffractometers. A modern powder diffractometer provides a fully digitalized diffraction data, which is exceptionally well-suited for visualization, computerized processing and analysis. The advances in the last few decades of the 20th century transformed XRPD from a method familiar only to a few, to one of the most broadly used techniques, thanks to the introduction and popularity of laboratory powder diffractometers. The use of synchrotron radiation, which provides high-resolution diffraction data, made XRPD capable of revealing the fine details of the solid state nature of complicated polycrystalline materials. It should be noted that there are many comprehensive textbooks and articles reviewing the design, function and technical details of laboratory and synchrotron machines, a selection of which is given in reference (2).

Both, laboratory and synchrotron powder diffractometers are designed to operate either in **reflection (Bragg-Brentano)** or **transmission (Debye-Scherrer)** geometry (Fig. 2.1.1). It could be argued that the reflection geometry (with parafocusing Bragg-Brentano optics) is more popular among the laboratory diffractometers worldwide. This geometry is suitable for strongly absorbing samples (especially as there is no need for absorption correction for a sample with "infinite" thickness). It is most commonly used with conventional divergent-beam X-ray sources. Taking a full advantage of focusing divergent beams, it provides both high resolution and high diffracted intensity, making the setup capable for fast high-resolution data collection. Moreover, it requires straightforward sample preparation, as the crystalline powders are simply placed onto a flat plate. The flat plate can be subjected to a number of external stimuli (temperature, irradiation, vapour environment, etc.) to initiate a chemical reaction or a physical process. The flat plate Bragg-Brentano geometry, unfortunately, is very susceptible to preferred orientation of the powder particles, especially when the microcrystalline sample is in form of plates or needles. Therefore, the collected diffraction data is not always suitable to be used in *ab initio* crystal structure determination. The Debye-Scherrer transmission geometry, on the contrary, is appropriate and mostly used setup for collecting data for *ab initio* structure solutions directly form powder diffraction data. In this geometry, the sample is placed onto a thin film or preferably into a capillary, which is then rotated for better particles' statistics. Another advantage of the capillary method is the requirement of very small amounts of sample. This geometry is also suitable for *in situ* data collection, as the capillary (or the thin film) can be easily placed in a specially designed chamber to perform variable temperature studies, photoirradiation, gas loading etc. The data collection done during the research on the case studies presented in this thesis, was done almost exclusively using the capillary method.

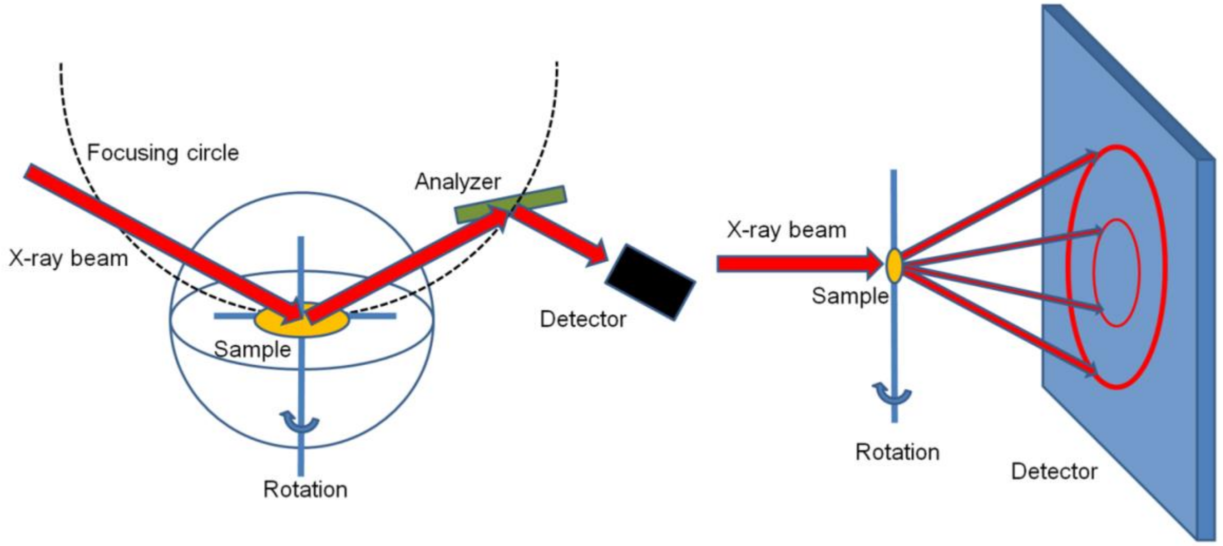

Figure 2.1.1. *A schematic representation of X-ray diffractometer operating in reflection (Bragg-Brentano, left panel) and transmission (Debye-Scherrer, right panel) geometry.*

Crucial component of any powder diffractometer is the **source of X-ray radiation**. Laboratory instruments most commonly use X-ray tubes, which consist of a stationary or rotating anode coupled with a cathode and placed in a sealed container under vacuum. The electrons are emitted by the cathode and accelerated towards the anode by a high electrostatic potential; the X-rays are generated by the impact of the electrons with the metal anode. Unfortunately, most of the energy supplied to the anode is converted into heat, and only a fraction of radiation consist the usable X-ray beam. Therefore, laboratory sources do not provide very high intensity of radiation, thus are not always suitable for *in situ* following of fast or ultrafast processes. Very high intensities of X-ray radiation can be achieved as a side product of accelerated particles in synchrotron facilities (such as the Diamond Light Source in Ditcod, ESRF in Grenoble, DESY in Hamburg and many others; a list of published papers on the characteristics is given in the references). (6) For a comparison, Fig. 2.1.2 schematically presents the available brilliance of laboratory and synchrotron generated X-rays (brilliance is defined as number of photons per second per square millimetre per square milliradian per 0.1% bandwidth), which shows how superior the synchrotron generated radiation is, compared to common laboratory X-ray sources.

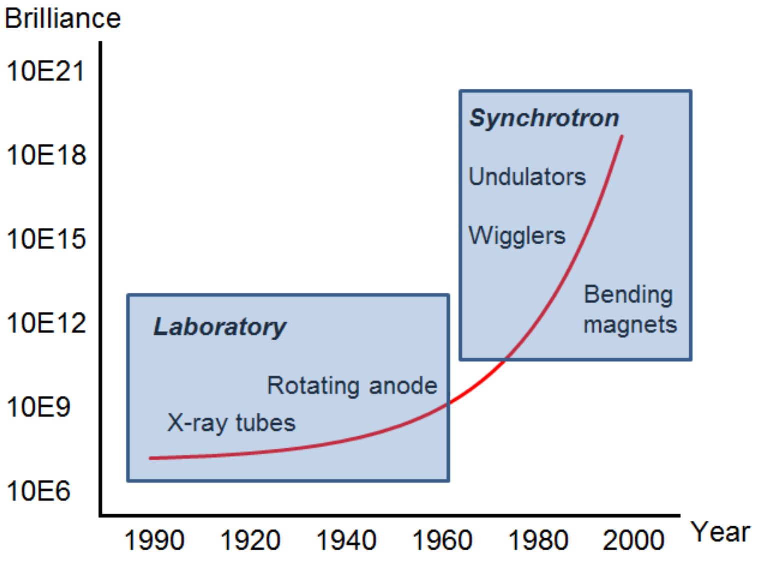

Figure 2.1.2. *Schematic representation of the development of the available brilliance of X-rays generated from different laboratory and synchrotron sources achieved over time.*

The intensity of X-ray radiation is crucial for *in situ* studies, as it limits the scanning speed of data collection. It is needless to say that the time of data collection must be at the same time-scale, or preferably lower, compared to the time-scale of the chemical/physical process studied; otherwise the (short-lived and/or metastable) intermediate states cannot be detected. The importance of scanning speed can be recognized, for example, in following of the radiation induced phase transition of rubidium triflate, where different amount of structural information can be extracted when the diffraction data are collected at different scanning speed (5 min/scan, 1 min/scan and 30 sec/scan), as shown in Fig. 2.1.3. (7)

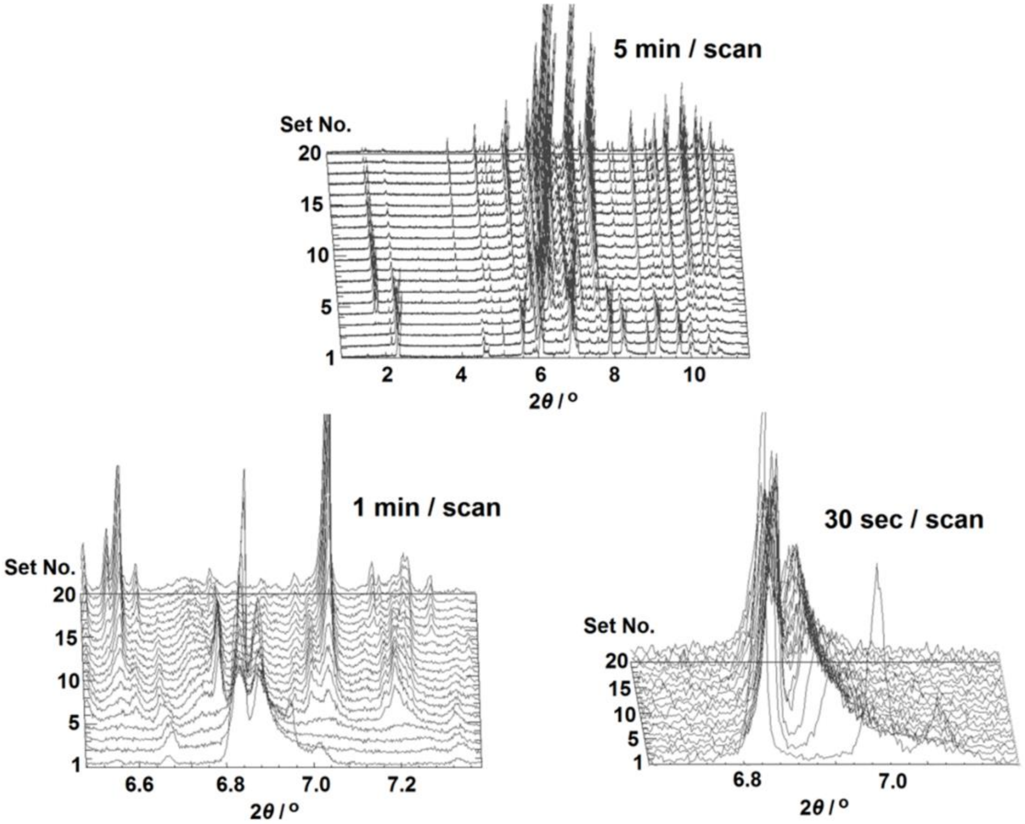

Figure 2.1.3. *Radiation-induced phase transition of rubidium triflate (measured at the beamline ID31, ESRF) showing the importance of intensity (scanning speed) in data collection. (7)*

When using a **synchrotron generated X-ray radiation**, the combination of brilliance and excellent vertical collimation provides collection of data with substantially improved signal-to-noise ratio and much higher resolution compared to data collected with laboratory diffractometers. With high-resolution data the problem of accidental peak overlap is much alleviated, allowing more unambiguous extraction of scattered intensity. Better separation of the accidently overlapped Bragg peaks is critical at any level of data analysis (indexing, structure solution, Rietveld refinement, qualitative and quantitative phase analysis etc.), especially in successful determination of lattice parameters. High resolution data are of outmost importance for *in situ* observation of chemical reactions, as often the reactant and the product have reflections at similar 2θ positions, and is critical to have them resolved. The need for high resolution is even more visible in *in situ* monitoring of second order phase transitions where the splitting of Bragg reflections can lead to very small differences in 2θ values. Figure 2.1.4 presents powder diffraction patterns of lithium potassium triflate, collected on a laboratory diffractometer and at two synchrotrons (NSLS and ESRF), showing significantly different degree of peaks resolution and different peak shapes, depending on the instrumental setup. (6, 7)

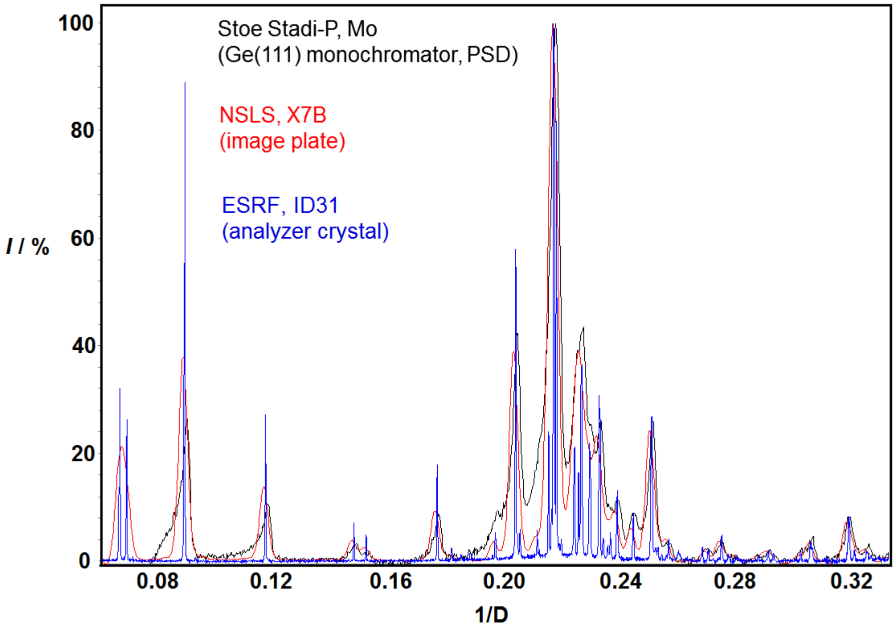

Figure 2.1.4. *Powder diffraction patterns of lithium potassium triflate collected at a laboratory diffractometer and at two synchrotrons, showing different resolution and peak shape. (7)*

For performing an *in situ* XRPD experiment, the **sample environment** needs to be modified to allow variation of the experimental conditions. Most of the commercial powder diffractometers and synchrotron setups can be easily upgraded to execute data collection at non-ambient conditions. In some cases, no instrumental modifications are needed, for example a slow degradation reaction of a crystalline solid can be followed by time, with the sample simply placed in capillary or on a flat plate. For temperature-variable experiments the sample holder can be placed inside a heating/cooling oven or next to a hot/cold air blower, as presented in Fig. 2.1.5a-d. For following photoinduced reactions (such as photodimerisations), the processes can be initiated using a UV irradiation photochamber, an example of which is schematically presented in Fig. 2.1.5e, and a picture is given in Fig. 2.1.5f. There is a huge number of different reaction chambers designed for various types of reactions. They include (but are not limited to) high-pressure diamond anvil cells, humidity chambers, setups allowing *in situ* milling and grinding, gas-loading devices, and many others. (8)

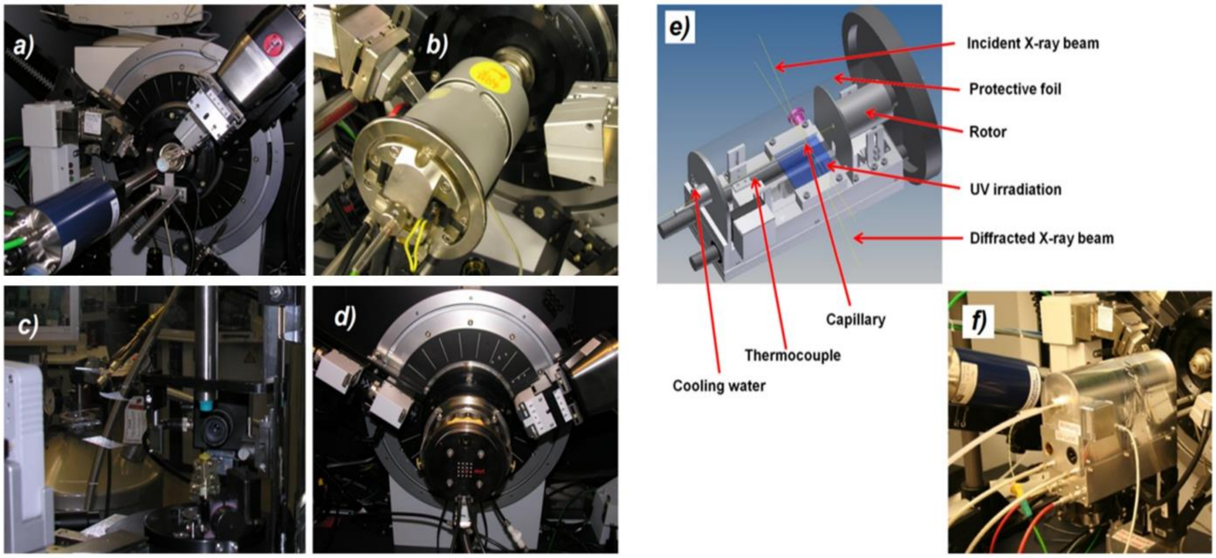

Figure 2.1.5. *Photographs of a) cold air blower and b) heating oven placed on an instrument in transmission geometry. c) Cold air blower placed on a different setup of transmission geometry. d) Heating/cooling oven placed on an instrument in reflection geometry. e) Schematic representation of a UV irradiation chamber for in situ photodiffraction and f) photograph of the UV irradiation chamber on a diffractometer in transmission geometry.*

When the design of such a chamber is in concern, the ability of X-rays to penetrate its walls (or windows), reach the sample, get scattered, and leave the chamber, deserves special attention. For this purpose, tuneable high-energy and high-intensity radiation is needed. Different metal anodes provide X-rays with different energies. Most commonly used anodes are made of Cu (X-rays with λ = 1.5406 Å), Mo (X-rays with λ = 0.7093 Å) and Ag (X-rays with λ = 0.5599 Å). Other, commercially available anodes are made of Co, Cr, Fe, Mn, Ni, etc. Synchrotron sources provide X-rays wavelengths spanning a wide spectrum. Moreover, their wavelength can be changed readily (this can be also exploit to diminish the effects of X-ray absorption). In addition to tunability, synchrotron radiation is characterized by immensely higher intensity, which makes it a very favourable choice for *in situ* studies. Figure 2.1.6 presents an example of synchrotron generated, tuneable-energy X-rays to probe the inside of a reacting system. (8e)

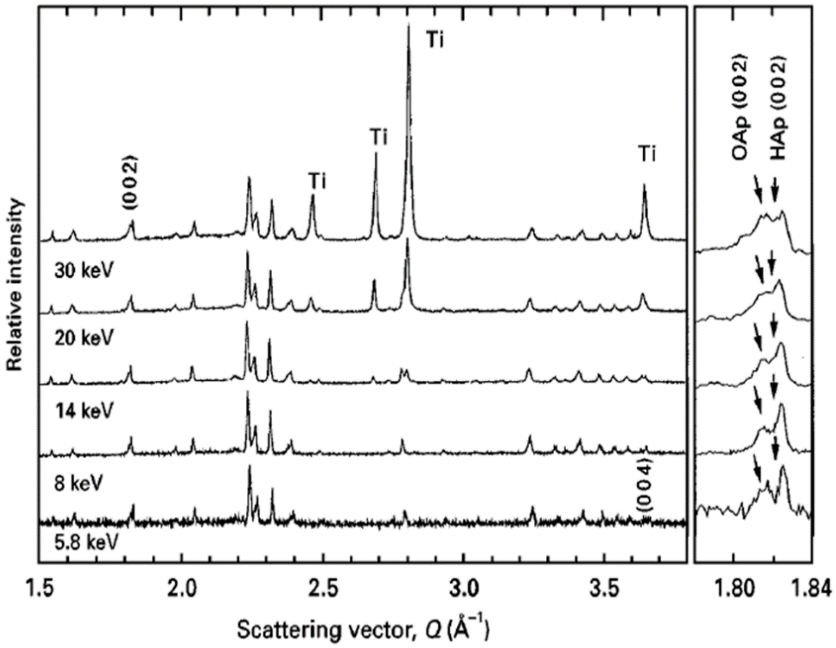

Figure 2.1.6. *Powder diffraction patterns of oxyapatite/hydroxyapatite coatings on titanium substrate collected using different radiation energies showing the importance of high-energy radiation for tuning the penetration depth. (7e)*

Recent developments of *in situ* powder diffraction enormously benefited from the introduction of new **X-ray detectors**, capable of precise and high-speed detection of scattered X-ray intensity. X-ray detectors fall in two broad categories: ratemeters and true counters. In the ratemeter detectors, the readout is performed after a hardware integration, which results in an electrical current or a voltage signal proportional to the number of photons detected. In the true counters, individual photons are counted as they hit the detector. Another systematization of detectors is based on whether the detector is designed to resolve the location where on the surface the photon has been absorbed. Gas proportional, solid-state and scintillation detectors do not allow spatial resolution, thus are known as point detectors. They register only the intensity of the diffracted beam, counting one point at a time. The detected scattered intensity is ascribed to a certain Bragg angle by analysing the relative position of the detector to both the sample and the incident beam. Detectors which allow spatial resolution of the diffracted intensity in one direction are known as line detectors. For example, the position sensitive detector (PSD) falls in this class, as it measures the diffracted beam along a single line. Finally, detectors which register the scattered intensity onto a 2D surface are called area detectors, such as the charge coupled devices (CCD) and image plate detectors (IPD). Area detectors are the most suitable choice for *in situ* XRPD, as they are stationary and need short exposition time for to register diffracted intensity, thus very high-speed data collection can be achieved. It should be noted, however, that the cost to pay for high-speed data collection is inevitable lowering of the resolution.

It can be argued that a synchrotron X-ray source coupled with a high sensitive area detector, and a sample holder adapted to induce a process or reaction, is a preferred setup for an *in situ* diffraction study. The combination of continuous wavelength spectrum, high intensity and intrinsic collimation of the synchrotron radiation is advantageous over any laboratory source. Nonetheless, laboratory diffraction undoubtedly plays an important role in the development of *in situ* crystallographic studies. It is available “in house” and it is needed for all preliminary experiments. With the recent advances in laboratory radiation sources, and the use of high-sensitive silicon chip detectors, high resolutions both in 2θ (well-resolved, high-intensity diffraction peaks) and in scanning speed (many collected diffraction patterns in a unit of time) can be achieved. As shown in some of the case studies presented in this thesis, a number of chemical processes and reactions can be successfully followed *in situ* in the laboratory.

2.2. Approaches for Crystal Structure Solution and Refinement from Powder Diffraction Data

Crystal structure determination (from XRPD), most generally spoken, can be divided in three stages: *a) Determination of the lattice parameters, unit cell symmetry and space group, b) solution and c) refinement of the crystal structure*. Once the unit cell content and its symmetry has been established, the structure solution process can be initiated. The solution procedures, at their core, are based on *global optimization* methods, yielding a structural model close to the true structure. Thereafter, if that model is a sufficiently good representation of the actual structure, it can be subjected to *local optimization* methods, or refinement of its fine details. After convergence of the refinement, the crystal structure can be considered as being solved and refined.

Shortly after the discovery of X-ray diffraction, the possibility structurally to investigate crystalline materials was recognized. It could be even said that many of the very first *ab initio* crystal structure determinations were done from XRPD. The solutions were performed after manually (from first principles) finding the lattice parameters and assigning the space group. Among the first reported cases are those of UCl_3, solved in the 1940s by locating the heavy atom in the unit cell and then estimating the chlorines positions, (9a); β-Po solved by manual direct phasing procedure, (9b); and UO_2Cl_2, solved by the Patterson technique in the 1960s. (9c)

Every stage of the structure solution procedure had enormous benefit of the introduction of computers. The determination of lattice parameters and the assignment of the space group became possible for low symmetry materials only after the development of the so-called **indexing** algorithms realized in commercially available programs. (10) These algorithms use accurately determined diffraction peak positions to generate many lattice parameters sets that are consistent to them. As a result, a number of possible lattice parameters are obtained and a variety of figures of merit can be used to rank among the solutions. Once the correct lattice is found, its space group is assigned by identifying the systematic absences of reflections in the indexed powder pattern. Due to systematic and accidental peak overlap, many times it is not possible to assign the space group uniquely, and it might be needed to carry on structure solution in all possible space groups.

Once the lattice parameters and space group have been determined, the pattern is considered to be fully indexed. That is, to every experimentally observed reflection a corresponding *hkl* index is ascribed. The next sept is precise determination of the intensity of every reflection peak. In most cases, the execution of this task is not straightforward due to the presence of peaks overlap. As a response, the **pattern decomposition** techniques have been developed. The seminal work in this field was carried by Pawley and Le Bail. (11) These techniques adopt a least-squares procedure to fit a calculated profile to the experimental diffraction data without the use of structural model. Generally, the lattice and peak shape parameters, the zero-error and the background parameters are refined.

Within the last few decades close attention was paid on the development of new methods and algorithms for structure solution form powder diffraction data. The techniques for solving a crystal structure can be divided in three groups: *a) conventional reciprocal space methods, b) conventional direct space methods and c) unconventional reciprocal, direct and dual-space methods*.

Before to apply any **reciprocal space methods**, the powder diffraction pattern must be deconvoluted and the integrated intensities of as many as possible individual Bragg reflections to be determined with maximum precision. (12) This is crucial owning to the fact that these methods are based exclusively on the observed structural factors. Among the most famous of them is the *Patterson technique*, which is also called the heavy-atom method because it works best when some of the atoms in the unit cell are markedly heavier, compared to the others (thus having much higher X-ray scattering ability). This method is based on sequential, iterative generation of maps, where the squared structure amplitudes are employed as coefficients in the Fourier transformation. The Patterson map shows the distribution of the interatomic vectors in the unit cell. By analysing the Patterson function, a structural model can be obtained in direct space. Another reciprocal space method is the *direct phase angle determination technique*, which is based on generating the probable phases that were lost during the data collection. The experimentally observed structure amplitudes are normalized and employed together with computed phases in the Fourier transformation, generating E-maps, which are in fact direct images of the electron density distribution function. The maxima of the density distribution should correspond to the positions of the atoms in the unit cell. This procedure is repeated iteratively, and with every correct positioning of an atom, the subsequent electron density map becomes a more accurate representation of the crystal structure. After the crystal structure is solved by either of these methods, it is then subjected to a Rietveld refinement.

The intensities of individual Bragg reflections are often “hidden” in the powder diffraction pattern, thus the reciprocal space methods are not always applicable. The **direct space methods**, on the contrary, are used without the need of knowing the observed structural factors *a priory*. Most of them are, actually, trial-and-error techniques, in which a most probable model of the crystal structure is built and then refined against the experimentally observed powder pattern. These approaches require extensive crystallographic, chemical and physical knowledge, prior to any structure solution process. There is no established step-following procedure for structure solutions for these methods, as every case is with individual characteristics. The following are some general hints:

- In case of simple inorganic materials the possibility of finding an isostructural compound (a compound which has partially or completely different chemical composition but identical or similar stoichiometry and crystal structure) should be first explored.
- The special positions in the respective space groups with given multiplicities can be correlated to the previously established unit cell content (based on additional chemical and physical experiments, e.g. density measurements, spectroscopic investigations, gravimetry). Using these correlations, the number of possible space groups can be significantly narrowed, and in some cases a partial model can be built.
- Obtaining a partial model using known crystal structures of similar or related compounds (for example, structures with well-defined frameworks or layers).
- In cases where the crystal structure is simple or the building blocks are known, systematic search or geometrical modelling of possible trial structures can be undertaken.

Certainly, direct space methods are very applicable in structures derived by close packing of incompressible spheres (for example the structures of the elements), where the small number of existing possibilities can be systematically explored. This is also the case for simple crystal structures built of only few atoms.

Conventional reciprocal and direct space methods have severe limitations, and in many cases are inapplicable. Reciprocal space methods require high-resolution powder patterns with well-resolved Bragg reflections, whether direct methods require extensive prior knowledge on the crystal structure. Therefore, unknown crystal structures with complicated powder patterns often cannot be solved by either of them. It is not surprizing that although these methods are known for more than half a century, structure solution from powder diffraction data remained to be a niche technique as long as the beginning of the 1990s, when the **unconventional direct, reciprocal and dual space methods** were introduced. (13, 14) *Genetic algorithm* is one example of unconventional direct space optimization technique based on the evolution principle. (13a) It is designed to let only the members that fit best into the environment to survive. It is based on an iterative procedure, where complex processes equivalent to mating, mutation and natural selection are employed. The system, that is the crystal structure, is divided into fragments which "survive" or "die" depending on how they affect the fit of the calculated pattern to the experimentally observed scattered intensity. *Maximum entropy* and *maximum likelihood method* are based on Bayesian estimation theory, which is often used to derive the most probable values of missing data in a set. (13b) In XRPD, these methods can be used to restore the lost phase angles and to estimate the relative intensities of overlapped reflections. These approaches result in solving the phase problem, thus are unconventional reciprocal space methods. *Charge flipping algorithm* is a dual-space method (working in the reciprocal and the direct space simultaneously) and it modifies the electron density below a certain level, by "flipping the charge" or changing the sign of the electron density. (13c,d) It is an interesting method for being truly *ab initio*: the electron density is represented by a grid and not by atoms, thus no prior knowledge on the atom type, charge, composition etc. is necessary.

The unconventional direct space method of **simulated annealing (SA)** has been almost exclusively used for to solve the crystal structures presented in this thesis, and is arguably among the most used methods in the powder crystallographic community. (14a) It is a direct space method, as no attempt is made to extract the individual intensities of Bragg reflections. Instead, huge numbers of random trial structures (solutions) are generated by the Monte Carlo algorithm, (14b). Their powder patterns are simulated and then systematically compared to the experimental data. Namely, for every possible combination of x y z fractional coordinates in the unit cell (that is for every structure), a characteristic powder pattern can be simulated and compared to the experimentally observed one. The difference between them can be measured by a certain figure-of-merit, for example the R_{wp}. When R_{wp} is plotted against the fractional coordinates, the region with lowest values should ideally represent the solution. For example, in Fig. 2.2.1, R_{wp} is plotted as a function of two fractional coordinates in the unit cell (variation of the third fractional coordinate is assumed, but not presented in the plot). In the figure, three trial models are given: the starting (random) model; model corresponding to a local minimum; and model close to the true crystal structure, corresponding to the general minimum.

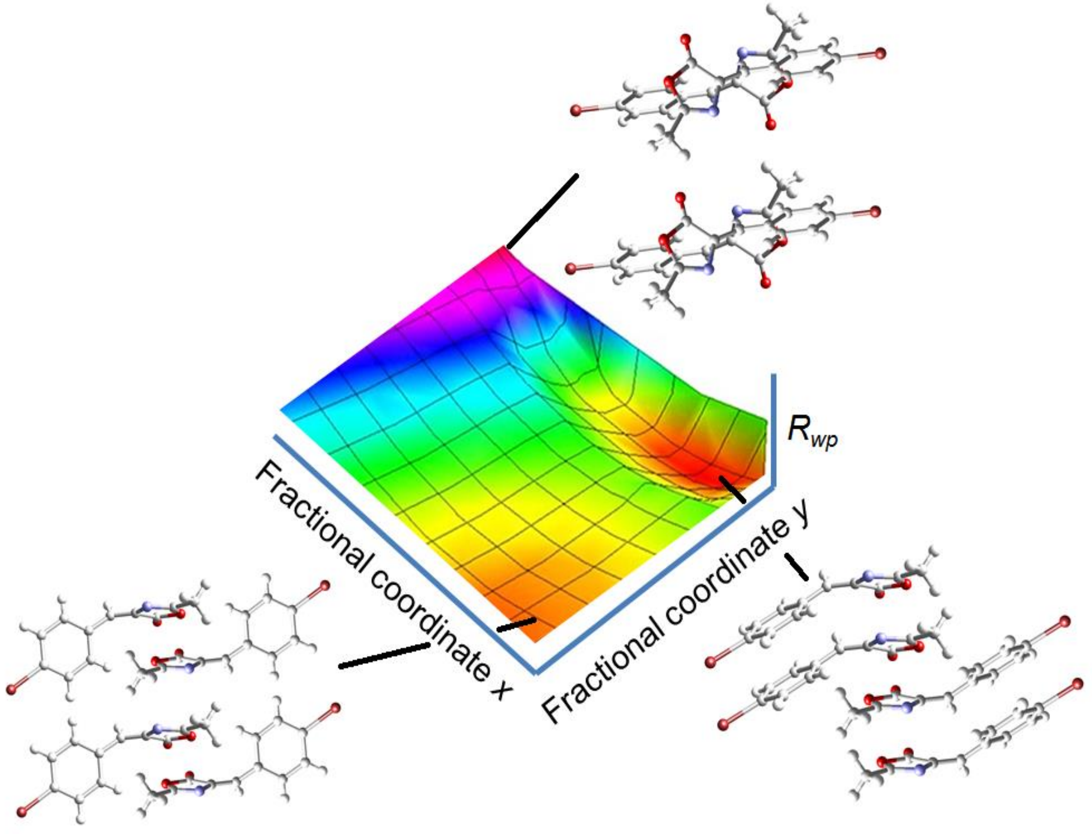

Figure 2.2.1. *Variation of the value of the R_{wp} as a function of the positions of the atoms in the crystal structure (the variation of the z coordinate is not shown). The upper model presents a random crystal structure, the model down left presents a local minimum, whereas the model down right presents the general minimum (corresponding to the correct solution).*

At the beginning of the SA procedure, the first structure (x_i) is chosen to be at random position and series of subsequent structures are then generated, with each structure derived from the previous one (x_{i+1}). New structures are produced by gradually changing the fractional coordinates and are considered as trial structures (x_{trial}). In the SA runs a trial structure is accepted or rejected using the Metropolis importance sampling procedure. (12c) A given trial structure is accepted or rejected based on a difference Z between the R_{wp} for the trial structure and R_{wp} for x_i:

$$Z = R_{\mathrm{wp}}(x_{\mathrm{trial}}) - R_{\mathrm{wp}}(x_{\mathrm{i}}).$$

If $Z \leq 0$, the trial structure is accepted as a new structure. If $Z \geq 0$, the trial structure is accepted as new structure with probability A or rejected with probability R:

$$A = e^{-Z/S} \text{ and } R = 1 - e^{-Z/S},$$

where S represents an appropriate scaling of Z. the value of S is systematically decreased by controlling an appropriate attenuation factor. The initial value of S is chosen so that virtually all trials are accepted, and as the value of S decreases the number of accepted structures decreases too, until the best structure solution is found. The working scheme of S must be modified in a way to be able to escape local minima.

The principles of SA can be explained by making an analogy with the process of forming a solid from a melt by constant cooling or annealing. At very high temperatures the atoms are allowed to move randomly and the potential energy of the system is considerably high. There are two ways to solidify the melt – by quenching and by slow cooling. If the melt is quenched, the atomic configuration gets immediately frozen, forming a glass phase with relatively high energy. If slow cooling is applied the atoms of the melt slowly move and "explore" the energy landscape, eventually adopting the configuration with lowest energy (the crystalline state). This thermodynamic reasoning can be readily applied in structure solution from powder diffraction data, where the variable structural parameters are the fractional coordinates of the unit cell, and the energy landscape is the given R-figure. In Fig. 2.2.1 it can be seen that the figure-of-merit surface, beside a global minimum, contains local minima. As mentioned before, the minimisation algorithm must also allow random steps in the uphill direction in the landscape to allow the system to escape possible local minima. The amount of uphill steps should be gradually decreased (by addition of an attenuation factor) on the course of the structure solution process, so that a minimization towards the global minimum may happen. Therefore, the procedure resembles the slow cooling of a melt where the lowering of the temperature acts as an attenuation factor. One example of SA runs is presented in Fig. 2.2.2, where the crystal structure of codeine phosphate sesquihydrate is solved.

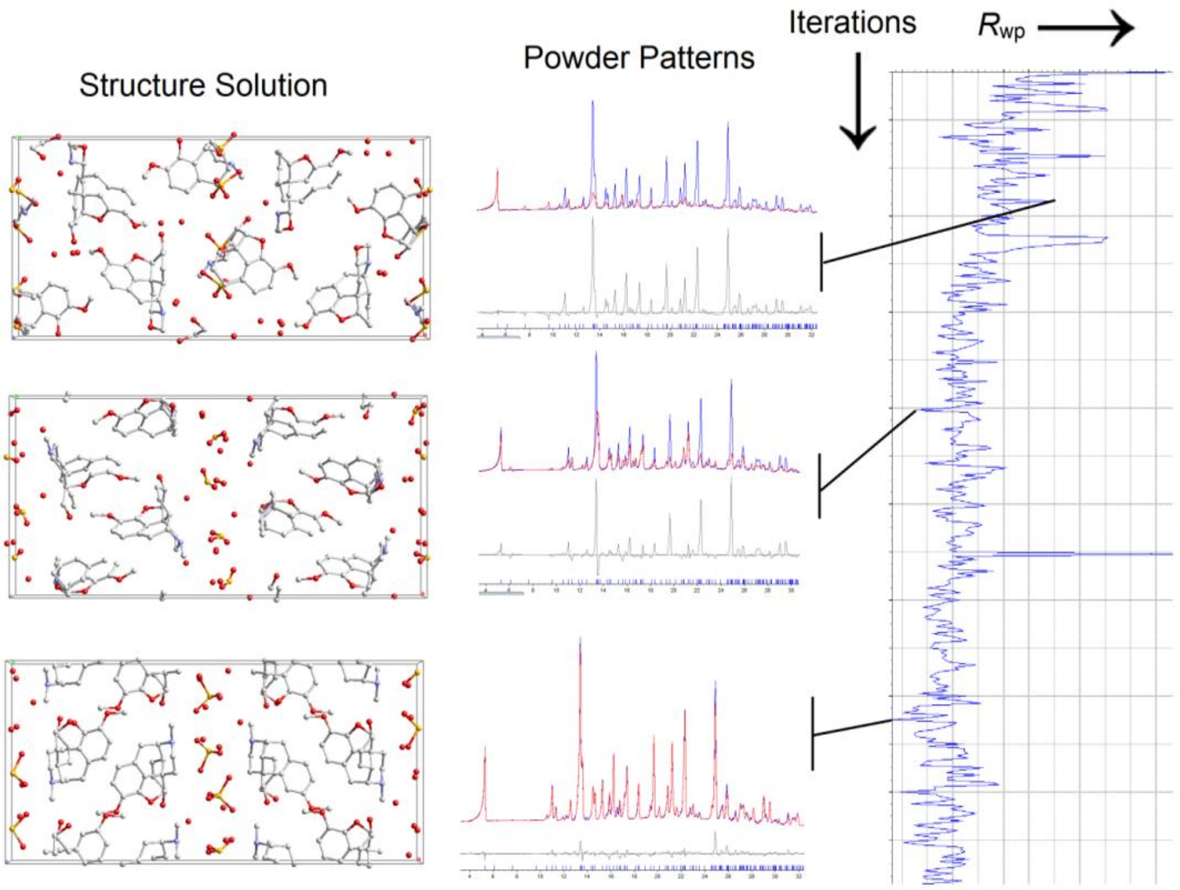

Figure 2.2.4. *One example of the applicability of the SA method: the first solution is far from the real crystal structure, thus the corresponding* R_{wp} *value is high. The second solution represents a local minimum (wrong solution, but with relatively low* R_{wp} *value) and the third solution represents the global minimum, or the correct solution, later confirmed by Rietveld refinement. The structure solution was performed by the software TOPAS. (5)*

Taken into account that the chemical systems sometimes contain large number of atoms in their asymmetric units, the computational cost of exploring every relative position of every single atom is very high and the optimization procedure can take unacceptably long time. This problem can be tackled by introducing **constraints and restraints** on the number of parameters and/or on their values, and only chemically possible and plausible models are explored. Naturally, during the structure solution process, the parameters that define the unit cell, peak-shape, background etc. should be kept fixt as they can be reasonably accurately determined by full-pattern decomposition methods, which need no prior structural model. The scale factor, however, should be refined during the SA runs. In case of molecular crystals, application of the rigid body approach additionally reduces the computational time. Very often a part of the structure has a well-defined stereochemical feature, for example in the crystal structure of one oxazolone molecules, the aromatic ring is always flat and all of its C–C bonds have the same length. This information can be provided and used in the SA runs by describing the known molecular fragment, for example the one presented in Fig. 2.2.3.

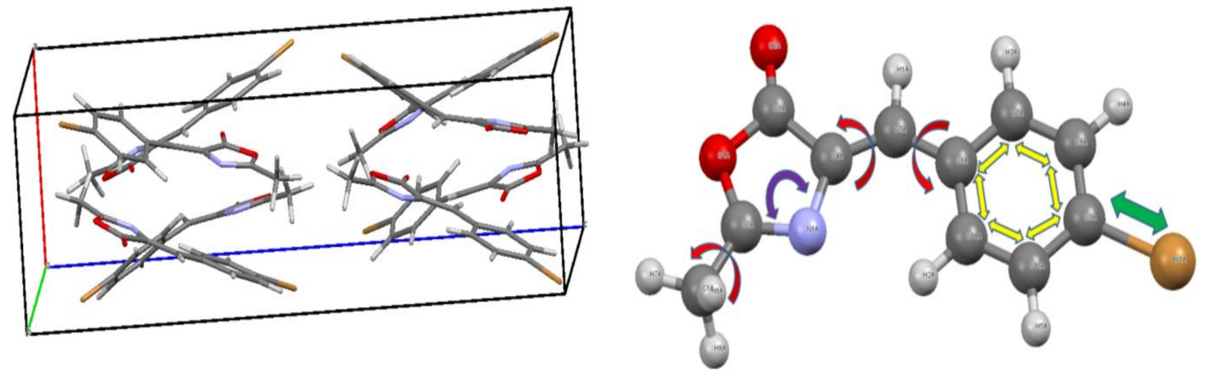

Figure 2.2.3. *(Left) Example of a crystal packing formed by oxazolone organic molecules. (Right) A molecule with known geometry, which can be refined by varying the three torsion angles (red arrows), the bond angles (one example is given in violet colour) and bond lengths, which are refined independently (for example the C–Br bond with green arrow) or collectively (for example the aromatic C–C bonds with yellow arrows).*

Instead applying free refinement of the positions of all atoms of the molecule, the known fragments can be described as **rigid bodies** placed in the asymmetric unit, which is infinitely repeated in space by means of the space group symmetry elements. The position of the rigid body within the crystal packing can be precisely determined by refining the translation and rotation vectors. The internal structure of the molecules can be refined by varying three different types of parameters: bond lengths, bond angles and torsion angles. This procedure heavily reduces the number of variable parameters. Namely, instead of free variation of three parameters for each of the 6 carbon atoms in the benzene ring (18 variables), only the translations (3 variables) and rotations (3 variables) together with joint variation of the C–C distances (1 variable) are refined. Therefore, in place of using 18 parameters, only 7 are needed. The reduction in number of parameters increases rapidly with increasing the number of atoms and rigidity of the molecule. For the free variation of all atoms in the molecule presented in Fig. 2.2.3 as much as 69 parameters are needed, if a rigid body is used only 22. Once the rigid body is established, only its translation, radiation and torsion parameters are varied, taken that the bond lengths and angles have approximately known values, which will be subsequently refined using the Rietveld method.

Once the solution of the crystal structure is finalized, the very final step is refining the model. In 1969, H. M. Rietveld proposed a new method for refining complex patterns by means of least-squares curve-fitting procedure of the entire powder pattern. (15a) This method, today known as "**Rietveld refinement**", caused a true revolution in the field of XRPD and it is extensively used ever since. Comprehensive and detailed reviews on the method are given in reference (15). Rietveld realized that a neutron powder pattern can be considered as a smooth curve that consists of peaks with Gaussian shape, superimposed on top of a smooth background (Fig. 2.2.4). A possible way of extracting large amount of information from that curve is to write a mathematical expression to represent the observed intensity at every step of the pattern:

$$Y_c = Y_b + \sum Y_{hkl}$$

Where the first term, Y_b, is the contribution from the background and the second term is a sum of each Bragg reflections (Y_{hkl}) that are positioned continuously along the powder pattern step. Both components are represented by suitable mathematical formulations that embody both the crystalline and noncrystalline features of the pattern. The least-squares refinement minimizes the difference between the observed and simulated whole pattern, rather than separate, individual reflections, enabling refinement of complex crystal structures with very complicated powder patterns. The model function is parameterized by the crystal structure and by the diffraction experiment. The crystal structure is described by a suitable collection of parameters that give the arrangement of atoms in the unit cell (atomic fractional coordinates), their thermal displacement motions and the probability that each atom occupies a given position (site occupancies). A second set of parameters describes the powder diffraction pattern's profile *via* lattice parameters, peak profile parameters and background coefficients (frequently introduced as Chebyshev polynomials). Additionally, a scale factor which relates the calculated structure factors to the observed values is added. When needed, other parameters are included and refined, describing for example preferred orientation or texture of the powder particles, absorption of X-ray intensity or other effects.

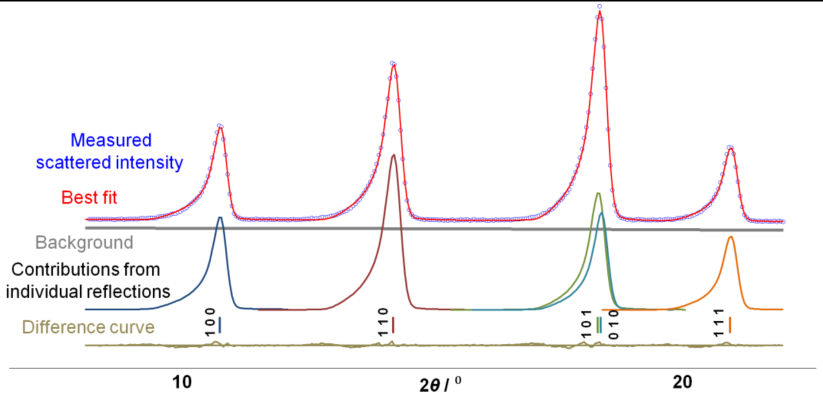

Figure 2.2.4. *Example of a diffraction powder pattern showing the scattered intensity (blue dots) and the fitted curve or calculated diffraction pattern (red line) composed of contributions from each Bragg reflection (differently coloured peaks) positioned above a continuous flat background (grey line).*

It is not an exaggeration to state that the Rietveld refinement provoked true renaissance of powder crystallography. Vast amount of crystal structures of different compounds were, and still are, refined using starting models of approximate, similar or known crystal structures. In the early days, this was particularly useful in cases of simple inorganic structures and intermetallics, which build isostructural compounds. The refinement of the composition of nonstoichiometric phases and solid solutions became readily available. Soon after it was shown that the Rietveld method can be also applied in cases of complicated inorganic and organic systems, when a good starting model of the crystal structure is available.

Today, almost every crystal structure solution is finalized by Rietveld refinement. The Rietveld method found many different applications. One example is the *quantitative Rietveld phase analysis*, which is a powerful tool in determination of the relative phase amounts, and is a routine technique in many laboratories in academia and industry. (2) Another example is the 2D refinement or the so-called *parametric Rietveld analysis*, in which Rietveld refinement is performed simultaneously on a number of powder patterns, so the number of refined parameters is heavily reduced and significant "non-crystallographic" parameters can be derived (such as rate of reactions, expansion coefficients, coefficients in phase transition analyses, among others). (16)

References

(1) a) Y. Waseda, E. Matsubara, K. Shinoda, *X-Ray Diffraction Crystallography: Introduction, Examples and Solved Problems*, Springer, 2011; b) D. W. Bennett, *Understanding Single-Crystal X-Ray Crystallography*, Wiley-VCH, 2010.

(2) a) R. E. Dinnebier, S. J. L. Billinge, *Powder Diffraction : Theory and Practice*, RSC Publishing, 2008; b) V. K. Pecharsky, P. Y. Zavalij, *Fundamentals of Powder Diffraction and Structural Characterization of Materials, Second Edition*, Kluwert Academic Publishers, 2003; c) A. Clearfield, J. Reibenspies, N. Bhuvanesh, *Principles and Applications of Powder Diffraction*, Wiley-Blackwell, 2008; d) G. Will, *Powder Diffraction: The Rietveld Method and the Two Stage Method to Determine and Refine Crystal Structures from Powder Diffraction Data*, Springer, 2006; e) W. I. F. David, K. Shankland, L. B. McCusker, Ch. Baerlocher, *Structure Determination from Powder Diffraction Data,* IUCr Monographs on Crystallography, 13, 2002.

(3) a) A. Westgren, *Iron Steel Ins.,* 1921, **CIII**, 5; b) L. Vegard, *Z. Phys.*, 1929, **58**, 497.

(4) The list of references on *in situ* powder diffraction is very long and still growing. Some examples are: a) P. Norby, *J. Am. Chem. Soc.*, 1997, **119**, 5215; b) R. E. Dinnebier, S. Carlson, M. Hanfland, M. Jansen, *Am. Mineral.*, 2003, **88**, 996; c) A. F. Mabied, M. Müller, R. E. Dinnebier, S. Nozawa, M. Hoshino, A. Tomita, T. Sato and S. Adachi, *Acta Crystallog.*, 2012, **B68**, 424; d) T. Friščić, I. Halasz, P. J. Beldon, A. M. Belenguer, F. Adams, S. A. J. Kimber, V. Honkimäki, R. E. Dinnebier, *Nature Chem.*, 2013, **5**, 66; e) R. I. Walton, D. O'Hare, *Chem. Commun.*, 2000, 2283.

(5) TOPAS version 4.2, 2007, Bruker-AXS, Karlsruhe, Germany.

(6) a) S. P. Thompson, J. E. Parker, J. Marchal, J. Potter, A. Birt, F. Yuan, R. D. Fearn, A. R. Lennie, S. R. Street, C. C. Tang, *J.Synchrotron Rad.*, 2011, **18**, 637; b) S. P. Thompson, J. E. Parker, J. Potter, T. P. Hill, A. Birt, T. M. Cobb, F. Yuan, C. C. Tang, *Rev. Sci. Instrum.*, 2009, **80**, 075107; c) A. N. Fitch, *J. Res. Natl. Inst. Stand. Tech.*, 2004, **109**, 133.

(7) L. Hildebrandt, R. E. Dinnebier, M. Jansen, *Inorg. Chem.*, 2006, **45**, 3217.

(8) The list of references on reaction chambers and devices designed for *in situ* powder diffraction is very long and still growing. Some examples are: a) A. Jayaraman, *Rev. Mod. Phys.*, 1983, **55**, 65; b) H. Hashizume, S. Shimomura, H. Yamada, T. Fujita, H. Nakazawa, O. Akutsu, *Powder Diffraction*, 1996, **11**, 288; c) I. Halasz, S. A. J. Kimber, P. J. Beldon, A. M Belenguer, F. Adams, V. Honkimäki, R. C. Nightingale, R. E. Dinnebier, T. Friščić, *Nature Protocols*, 2013, **9**, 1; d) A. Soleimani-Dorcheh, R. E. Dinnebier, A. Kuc, O. Magdysyuk, F. Adams, D. Denysenko, T. Heine, D. Volkmer, W. Donner, M. Hirscher, *Phys. Chem. Chem. Phys.*, 2012, **14**, 12892; e) K. A. Gross, C. C. Berndt, P. Stephens, R. E. Dinnebier, *J. Mat. Sci.*, 1998, **33**, 3985.

(9) a) W. H. Zachariasen, *Acta Crystalogr.*, 1948, **1**, 265; b) W. H. Zachariasen, F. H. Ellinger, *Acta Crystalogr.*, 1963, **16**, 369; c) P. C. Debets, *Acta Crystalogr.*, 1968, **B24**, 400.

(10) a) J. W. Visser, *J. Appl. Crystallogr.*, 1969, **2**, 89; b) P. –E. Werner, L. Eriksson, M. Westdahl, *J. Appl. Crystallogr.*, 1985, **18**, 367; c) A. Boultif, D. Louër, *J. Appl.*

Crystallogr., 1991, **24**, 987; d) R. Shirley, *Data Accuracy for Powder Indexing*, Natl. Bur. Stand. (US) Spec. Publ. No. 567, 1980.

(11) a) G. S. Pawley, *J. Appl. Cryst.*, 1981, **14**, 357; b) A. Le Bail, *Mater. Res. Bull.*, 1988, **23**, 447.

(12) a) A. L. Patterson, *Phys. Ref.*, 1934, **46**, 372; b) M. M. Woolfson, *Acta Crystalog.*, 1987, **A43**, 593.

(13) a) K. Shankland, W. I. F. David, T. Csoka, *Zeit. Krist.* 1997, **212**, 550; b) G. Bricogne, C. J. Gilmore, *Acta Crystalogr.*, 1990, **A46**, 284; c) G. Ozlányi, A. Süto, *Acta Crystallog.*, 2004, **A60**, 134; d) J. Karle, H. Hauptman, *Acta Crystallog.*, 1956, **9**, 635; e) Y. G. Andreev, G. S. MacGlashan, P. G. Bruce, *Phys. Rev.*, 1997, **B55**, 12011; f) K. D. M. Harris, M. Tremayne, *Chem. Mater.*, 1996, **8**, 2554.

(14) a) Y. G. Andreev, G. S. MacGlashan, P. G. Bruce, *Phys. Rev.*, 1997, **B55**, 12011; b) M. P. Allen, D. J. Tildesley, *Computer Simulation of Liquids*, Oxford University Press, 1987; c) K. Metropolis, S. Ulam, *J. Am. Stat. Assoc.*, 1949, **44**, 335.

(15) a) H. M. Rietveld, *J. Appl. Cryst.*, 1969, **2**, 65. b) R. A. Young, *The Rietveld Method*, IUCr/OUP: Oxford, 1993; c) R. J. Hill, I. C. Madsen, *Powder Diffraction*, 1987, **2**, 146; d) L. B. McCusker, R. B. Von Dreele, D. E. Cox, D. Louër, P. Scardi, *J. Appl. Cryst*allogr., 1999, **32**, 36; e) R. B. Von Dreele, *J. Appl. Cryst*allogr., 1997, **30**, 517.

(16) a) G. W. Stinton, J. O. S. Evans, *J. Appl. Crystallogr.* 2007, **40**, 87; b) A. F. Mabied, M. Mueller, R. E. Dinnebier, S. Nozawa, M. Hoshino, A. Tomita, T. Sato, S. Adachi, *Acta Crystallogr.* 2012, **B68**, 424; c) I. Halasz, R. E. Dinnebier, R. Angel, *J. Appl. Crystallogr.*, 2010, **43**, 504; d) O. V. Magdysyuk, M. Muller, R. E Dinnebier, C. Lipp, T. Schleid, *J. Appl. Crystallogr.*, 2014, **47**, 701.

3. Case Studies of Application of *In Situ* XRPD

3.1. Crystal Structure of Calcium Hemicarboaluminate and *In Situ* Monitoring of its Transformation into Carbonated Calcium Hemicarboaluminate

One of the main phases formed at the beginning of carbonation reactions of cementitious materials is the calcium hemicarboaluminate. At atmospheric conditions this phase gradually reacts with the carbon dioxide and transforms into carbonated a calcium hemicarboaluminate. The crystal structures of these phases are of high importance to the building and construction industry, and they were solved and refined using synchrotron XRPD data. The analyses show that they both are composed of the same positively charged main layers, but differ in the structure of the negatively charged interlayers, where CO_2 *is part of the structure in form of its carbonate anion. The carbonation reaction was carefully followed by analysis of the in situ collected diffraction data.*

3.1.1 Introduction

Calcium aluminate cements promises many practical applications due to their remarkable ability to rapidly develop strength and their high chemical resistance. On hydration, they form so-called AFm phases, (1–4) a hydrated tetracalcium aluminate compounds belonging to the lamellar double hydroxide family. These phases are composed of positively charged main layers and negatively charged interlayers. The main layers, with a chemical formula $[Ca_4Al_2(OH)_{12}]^{2+}$, are "universal" within the AFm family in respect to their chemical composition and crystal structure. On the contrary, the interlayer region is characterized by pronounced diversity in the composition and structural features. It can accommodate one, two or three different types of anions, forming primary, secondary or tertiary interlayered structures, respectively. In the primary phases the anion can be a carbonate, sulfate, chloride, iodide, nitrate, among others. (1) Several cases of binary phases were published, with sulfate and chloride, chloride and carbonate, bromide and chloride, or hydroxide and carbonate as anions. (2) Examples of a ternary AFm phase containing sulfate, carbonate and hydroxide are also described in the literature. (3) Of particular interest are the carbonated AFm phases, taken that they appear as first carbonation products of many Portland cements. The crystal structure of the main phase of these carbonation products, the calcium hemicarboaluminate (Hc), remained unsolved half a century after its discovery. (4) Only the unit cell parameters were reported (a = 5.77 Å, c = 49.16 Å) assuming the *R*3*c* or *R*–3*c* as the most probable space groups. (1a) There are several reasons for this scarce crystallographic knowledge, including the crystal habit characteristics (micrometer sized thin plates not suitable for single crystal diffraction, Fig. 3.1.1), the pronounced stacking faults, preferred orientation, and other defects in the structure.

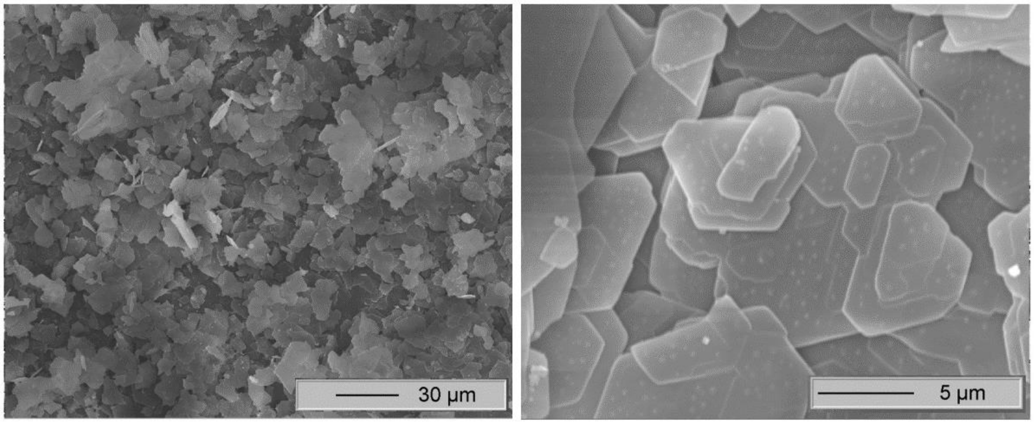

Figure 3.1.1. *SEM images of thin, hexagonal, uniaxial negative plates of the Hc-cHc phases.*

Taken that Hc is a very important phase to the construction industry, efforts were paid on detailing its crystal structure. Surprisingly, the reaction paste crystallized in a two phase mixture containing both the Hc and a further carbonated analogue, the calcium hemicarboaluminate (cHc). It was shown that Hc is not stable at atmospheric conditions and it gradually transforms into the cHc phase. The crystal structures of these phases were solved by synchrotron XRPD and the Hc-to-cHc reaction was monitored by *in situ* collected diffraction data.

3.1.2 Results and Discussion

The crystal structure of the Hc phase was solved and refined in the trigonal *R*–3*c* space group. It is composed of typical AFm main layers, where the aluminium cation is coordinated by six oxygen atoms forming a regular octahedron. The aluminium octahedra are arranged in a hexagonal primitive net, interconnected by calcium cations (Fig. 3.1.2a). Each calcium cation is coordinated by seven oxygen atoms; six of them belong to the main layer and one oxygen atom to a water molecule from the interlayer. These oxygen atoms form a polyhedron, which can be considered as a capped trigonal antiprism (Fig. 3.1.2b). The main layers are arranged perpendicularly to the *c*-axis (Fig. 3.1.2c). In the Hc phase, the interlayer region is composed of carbonate and hydroxide anions positioned in the middle of the interlayer, and water molecules bonded to the calcium cations of the main layers. For each aluminium cation, there are 0.25 carbonate and 0.5 hydroxide anions in the interlayer, providing electroneutrality. The carbonate anions are ordered and placed perpendicular to the three-fold symmetry axis running parallel to the crystallographic *c*-axis. The hydroxide anions are located on a general position, disordered around the carbonate anion. Because of the low occupancy and the disorder, the positions of the hydroxide group cannot be freely refined using the Rietveld method. In order to find their most probable positions, difference Fourier maps were generated, using a starting model containing the atoms of the main layers, the bonded water molecules in the interlayer, and the carbonate group with fixed occupancy of 0.25. Two sections of the generated difference electron density map are shown in Fig. 3.1.3. By closer inspection of the map neither positive, nor negative electron density can be observed around the carbon atom, implying correctly refined occupancy, whether positive electron density above and below the positions of the carbonate group is evident. Hydroxide anions were introduced in the model, at the position in the difference map with the most prominent excess of electron density, which resulted in a significant drop of the *R*-factor values (for example, the R_{wp} value drop down by 2 %). For the final refinements, the position and occupancy of the OH^- groups were kept fixed. Taken the disorder in the interlayer structure, and the statistical distribution into account, it can be assumed that the local symmetry of the crystal structure is significantly lower.

The Hc phase crystallized in a mixture with cHc, which was found to be its carbonated analogue. This phase has the same main layers as the Hc and, as expected, it differs in the interlayer structure. The crystal structure of cHc was solved by deriving the difference Fourier map, generated by the same starting model as in the case of the Hc phase. Inspection of the map showed pronounced excess of electron density around the positions of the carbonate atoms, indicating underestimated content of the carbonate group (Fig. 3.1.4). After refining the carbonate occupancy to a value of 0.4, the difference Fourier map showed neither significant positive, nor negative electron density around the carbonate anions, indicating a correctly refined crystal structure. To ensure electroneutrality, the occupancy of the hydroxide anions was reduced to a value of 0.2.

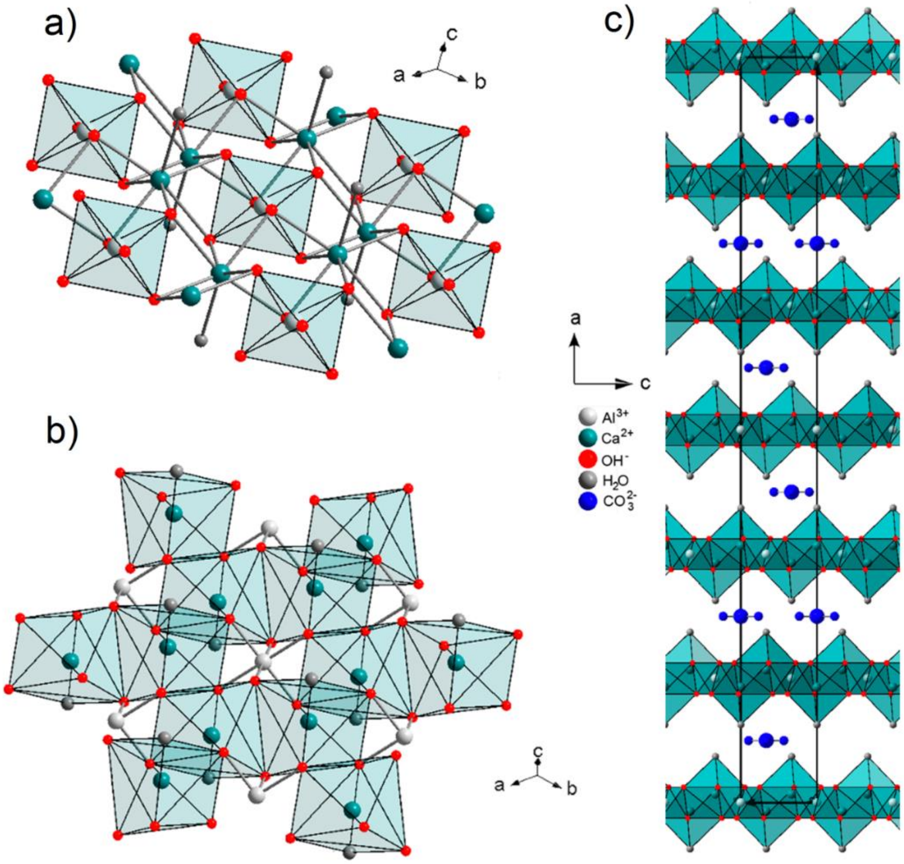

Figure 3.1.2. *Crystal structure of the Hc phase featuring the main layers built by a) aluminium octahedra and b) calcium capped trigonal antiprisms. c) In the packing diagram only the carbonate groups and the water molecules are shown, whereas the disordered* OH^- *anions and the hydrogen atoms are omitted for clarity.*

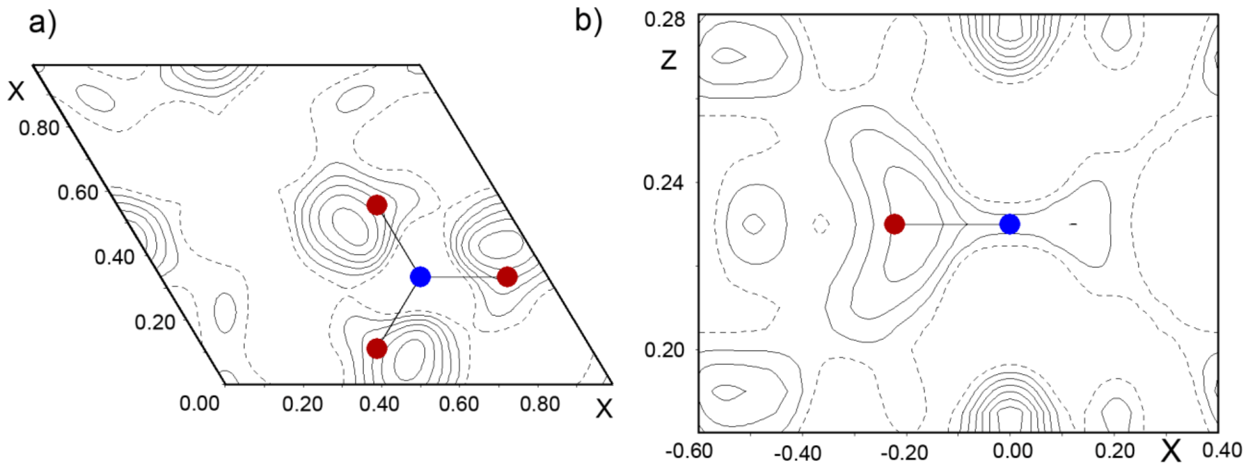

Figure 3.1.3. *2D difference electron density maps of the Hc phase. The positive contour levels start from 0 e/Å^3 with a step of 0.03 e/Å^3. a) Projection perpendicular to the z-axis (z = 0.095), with the carbonate group (carbon in blue, oxygen in red) imposed on the projection at z = 0.083. b) Projection perpendicular to the y-axis (y = 0).*

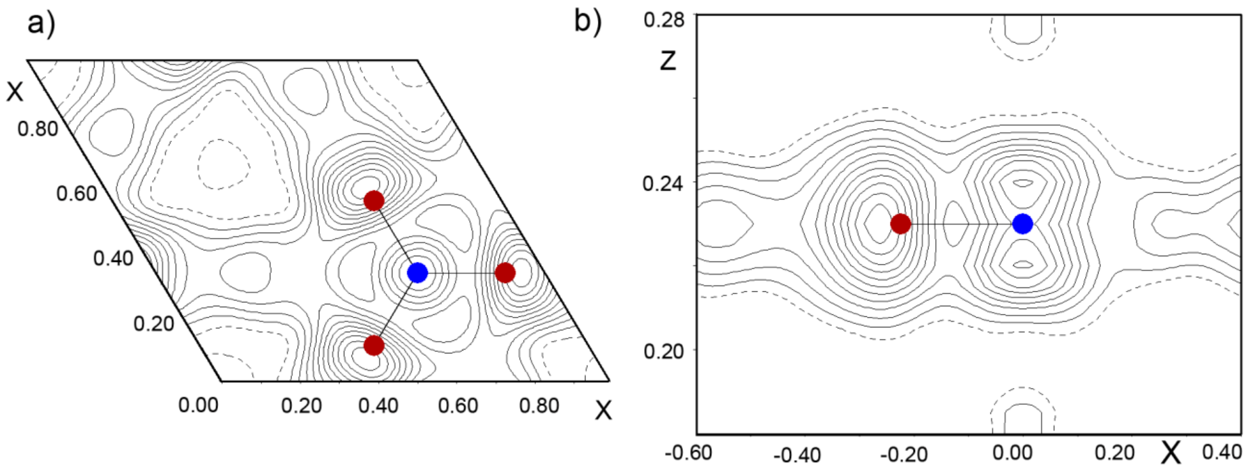

Figure 3.1.4. *2D difference electron density maps of the cHc phase. The positive contour levels start from 0 e/Å^3 with a step of 0.03 e/Å^3. a) Projection perpendicular to the z-axis (z = 0.095), with the carbonate group (carbon in blue, oxygen in red) imposed on the projection at z = 0.083. b) Projection perpendicular to the y-axis (y = 0).*

In situ diffraction data collection of the Hc-cHc system eased the structures solutions to a great extent. Namely, at room temperature the system crystallized in a mixture of four phases where Hc and cHc were found to be the major components (with 62.6 % and 33.8 % respectively). The other two phases with known crystal structures can be regarded as impurities (tricalcium dialuminium oxide hexahydrate, 16592-ICSD, and calcium carbonate, 20179-ICSD). Simultaneous, *ab initio* crystal structure solution of two unknown structures is a very difficult task, if not impossible. By *in situ* data collection on heating it was found that Hc gradually transforms into cHc in atmosphere with small amounts of carbon dioxide present in the capillary (at standard atmosphere the Hc phase directly transformed into the monocarboaluminate, Mc), as presented in in Fig. 3.1.5. By increasing the temperature over 333 K, Hc reacted with CO_2 giving cHc, which thus became the only major phase in system. The crystal structure of cHc was solved and refined at temperature of 347 K, and after that the known solution was used for handling the room temperature pattern and solving the crystal structure of the Hc phase.

3.1.3 Conclusions

The crystal structures of the two phases formed at the beginning of carbonation reactions of many Portland cements, the calcium hemicarboaluminate and its carbonated analogue, were solved and refined by XRPD using *in situ* synchrotron radiation. It was found that at ambient conditions they simultaneously crystallize in a mixture after drying the reaction paste. Their crystal packings are composed of positively charged main layers and negatively charged interlayers. The interlayer region accommodates statistically distributed carbonate and hydroxide anions. In the Hc phase, on every aluminium cation there are 0.25 carbonate anions and 0.5 hydroxide anions. By partial carbonation of the Hc phase the cHc phase is formed, in which there is a larger amount of carbonate anions (0.4) on account of the amount of hydroxide anions (0.2). The *in situ* XRPD analysis unambiguously showed that by increasing the temperature (in atmosphere with a reduced amount of carbon dioxide) the Hc phase completely transforms into the cHc phase.

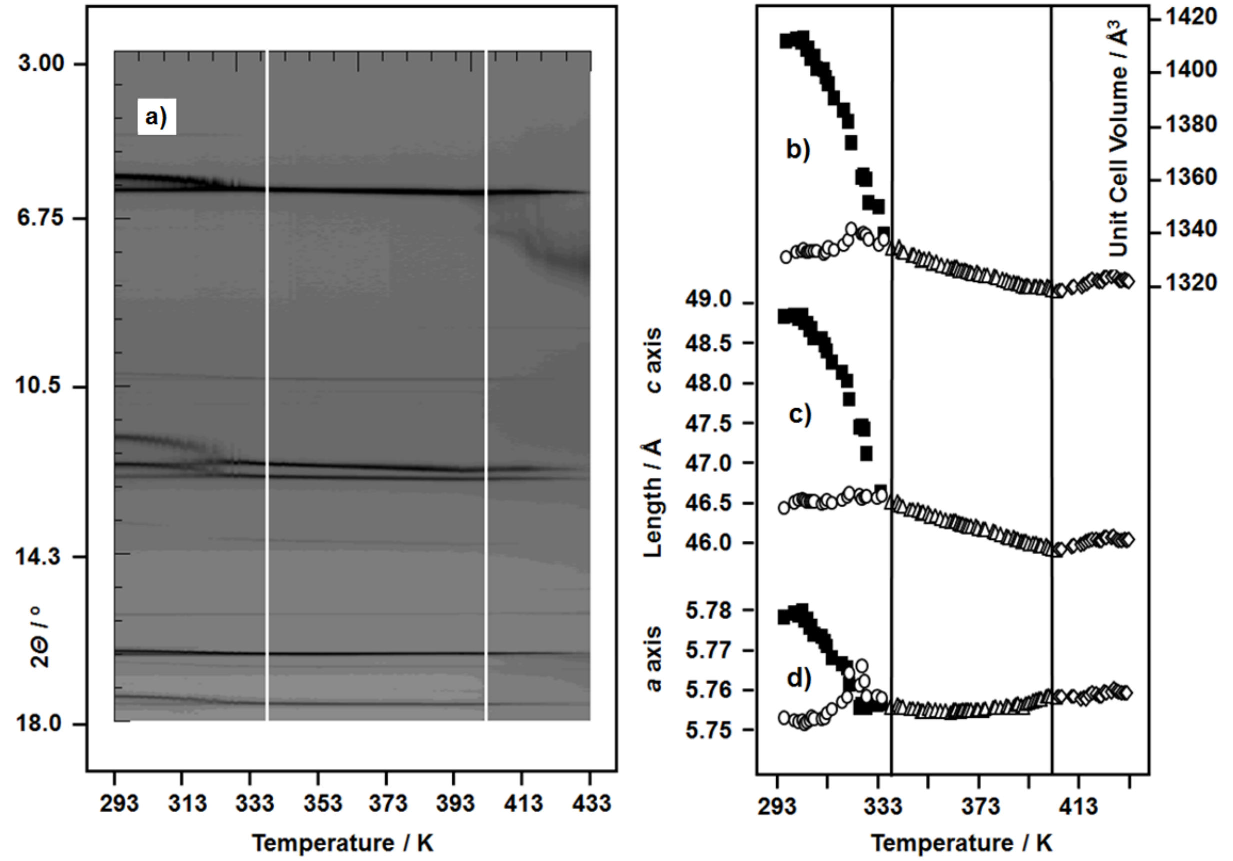

Figure 3.1.5. *a) 2D projection of the observed scattered synchrotron X-ray intensity as a function of temperature and diffraction angle. The changes in the values of the b) unit cell volume, c) c-axis and d) a-axis are plotted.*

3.1.4 Experimental Section

Instrumentation

For the determination of the crystal structures of Hc and cHc, powder diffraction data (Fig. 3.1.6 and Table 3.1.1) were collected at the I11 beamline located at the British synchrotron facility Diamond Light Source. The wavelength of radiation was determined from silicon standard to be 0.826405 Å. Diffraction data were collected in the temperature range from 297 K to 433 K. The scans at were written continuously with 2 K/min and 14 s/frame.

Sample Purity and Preparation

Finely powdered samples were placed in quartz capillaries (providing limited contact to the atmosphere). Reacting with limited amounts of CO_2 on heating, Hc completely transformed into the cHc phase. The analysis of the powder data collected at 293 K indicated that the sample consists of the two major phases (Hc and cHc) and impurities of $H_{12}Al_2Ca_3O_{12}$ (16592-ICSD) and $CaCO_3$ (20179-ICSD) present together in less than 4 weight % of the total amount.

Structure Solution and Rietveld Refinement

The extinctions of reflections found in the powder patterns indicated $R{-}3c$ as the most probable space group, which was later confirmed by a Rietveld refinement. (5a) The peak profiles and precise lattice parameters were determined by a Pawley fit (5b) using the fundamental parameter approach of TOPAS Version 4.2. (5c) Chebyshev polynomials were used for describing the background. The same procedure was repeated on the data collected at temperature of 347 K, where the cHc phase was the only phase present in the system (Fig. 3.1.5).

At the beginning of the crystal structure solution the atomic coordinates of the main layer atoms were taken from a related structure as a model. (5d) The solution was completed with finding the structure of the interlayer, performed by inspecting the difference Fourier maps. For the Rietveld refinement, all profile and lattice parameters as well as the atomic positions were refined, except of the parameters of the hydroxide oxygen atoms. The anisotropy of width and asymmetry of the Bragg reflections was successfully modelled by applying symmetry adapted spherical harmonics of eight’s order to Gaussian, Lorentzian and exponential distributions, which were then convoluted with the geometrical and instrumental contributions to the final peak profile. Despite the use of capillary in Debye-Scherrer geometry, a small amount of preferred orientation was detected, which probably originated from the plate like form of the crystallites and it was adequately described by the use of symmetry adapted spherical harmonics. The origin of the complex peak profile is quite likely related to occurrence of stacking faults of the layer structure and variations of the content of dissipated water in different domains. Rietveld refinements were done on the diffraction patterns collected at 297 K and 347 K (Fig. 3.1.6). The refinement data and the final agreement factors (*R*-values) are listed in Table 3.1.1.

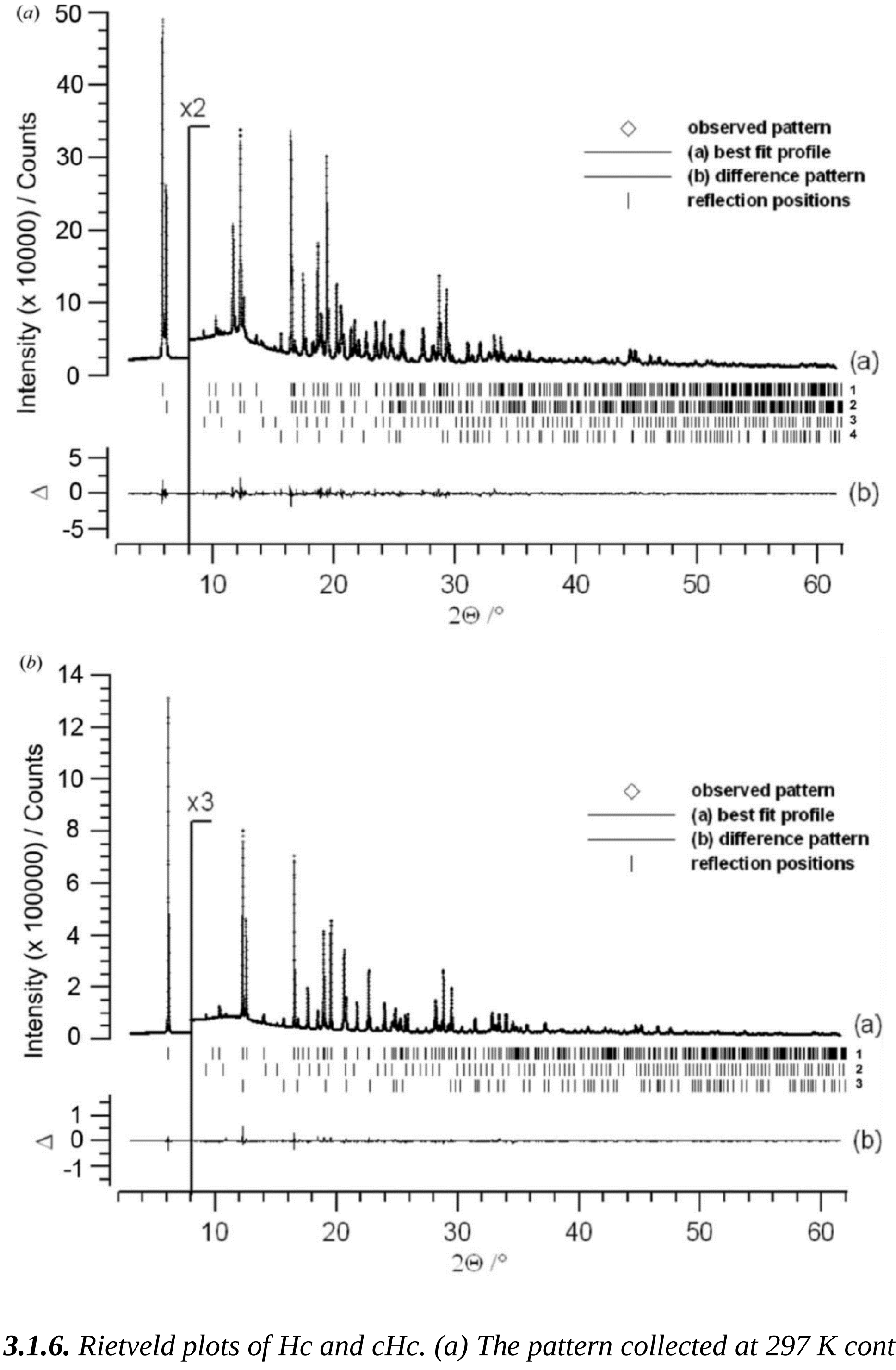

Figure 3.1.6. *Rietveld plots of Hc and cHc. (a) The pattern collected at 297 K contains two major phases, Hc and cHc, and impurities of* $H_{12}Al_2Ca_3O_{12}$ *and* $CaCO_3$ *(reflection positions 1, 2, 3, 4 respectively). (b) At 347 K only one major phase is present, cHc, whit impurities of* $H_{12}Al_2Ca_3O_{12}$ *and* $CaCO_3$ *(reflection positions 1, 2, 3, respectively).*

Table 3.1.1. *Crystallographic and Rietveld refinement data for Hc-cHc system.*

Compound name	Calcium Carboaluminate Hydrate		
Molecular formula	$[Ca_4Al_2(OH)_{12}][(OH)_{2n}(CO_3)_{1-n} \cdot 4H_2O]$		
Space group, Z	R–3c, 6		
Wavelength (Å)	0.826401(3)		
Starting angle (º 2θ)	3		
Final angle (º 2θ)	61.5		
Data collection	2 º/min and 14 s/frame		
	Hc	cHc	cHc
Temperature (K)	297	297	347
Weight amount (a) (%)	62.0	34.1	97.5
n	0.5	0.2	0.2
Formula weight (g/mol)	537.50	545.29	545.29
a (Å)	5.7756(1)	5.7489(1)	5.7343(1)
c (Å)	48.812(2)	46.347(4)	46.389(9)
V (Å^3)	1409.11(9)	1326.59(9)	1329.82(6)
R−Bragg (%) (b)	2.087	1.270	3.796
R–exp (%) (b)	0.773		0.784
R–p (%) (b)	2.910		2.983
R–wp (%) (b)	4.056		4.858
No. of variables	166		104

(a) The sample contained impurities of tricalcium dialuminium oxide hexahydrate, 16592-ICSD, and calcium carbonate, 20179-ICSD, with quantities less than 4 %. (b) The figures of merit are as defined in TOPAS 4.2.

References

(1) a) R. Fischer, H. Kuzel, *Cem. Concr. Res.* 1982, **12**, 517; b) M. François, G.Renaudin, O. Evrard, *Acta Crystallogr.* 1998, **C54**, 1214; c) G. Renaudin, F. Kubel, J. P. Rivera, M. François, *Cem. Concr. Res.* 1999, **29**, 1937; d) H. Pöllmann, T. Witzke, H. Kohler, *Neues Jahrb. Mineral. Monatsh.* 1997, 423; e) A. Terzis, S. Fillipakis, H. J. Kuzel, H. Bruzlaff, *Zeitschr. Kristallogr.* 1987, **181**, 29; f) J. –P. Rapin, G. Renaudin, E. Elkaim, M. François, *Cem. Concr. Res.* 2002, **32**, 63; g) J. –P. Rapin, A. Walcarius, G. Lefevre, M. François, *Acta Crystallogr.* 1999, **C55**, 1957; h) G. Renaudin, M. François, *Acta Crystallogr.* 1999, **C55**, 835, 1999.

(2) a) A. Mesbah, M. François, C. Cau-dit-Coumes, F. Frizon, Y. Filichuk, F. Leroux, J. Ravaux, G. Renaudin, *Cem. Concr. Res.* 2011, **41**, 504; b) A. Mesbah, J. –P. Rapin, M. François, C. Cau-dit-Coumes, F. Frizon, F. Leroux, G. Renaudin, *J. Am. Ceram. Soc.* 2011, **94**, 261; c) M. Sacerdoti, E. Passaglia, *Neues. Jahrb. Mineral. Abh.* 1988, **10**, 462; c) J. –P. Rapin, M. François, *Acta Crystallogr.* 2000, **C57**, 137; d) G. Renaudin, J. –P. Rapin, E. Elkaim, M. François, *Cem. Concr. Res.* 2004, **34**, 1845.

(3) a) H. Pöllmann, *Neues. Jahrb. Mineral. Abh.* 2006, **182**, 173; b) H. Pöllman, J. F. Löns, C. Kraus, *Ber. Der. Dt. Mineral. Ges.* 1998, 219.

(4) a) W. Dosch, H. zur Strassen, *Zement-Kalk-Gips* 1965, **5**, 233; b) S. J. Ahmed, D. Glasser, L. S. W. Taylor, *Proc. Fifth Int. Symp. Chem. Cement*, vol II, Tokyo, 118, 1968; c) M. H. Roberts, *Proc. Fifth Int. Symp. Chem. Cement*, vol II, Tokyo, 118, 1968.

(5) a) H. M. Rietveld, *J. Appl. Cryst.*, 1969, **2**, 65; b) G. S. Pawley, *J. Appl. Cryst.*, 1981, **14**, 357; c) TOPAS version 4.2, 2007, Bruker-AXS, Karlsruhe, Germany; d) A. Mesbah, J. –P. Rapin, M. Francois, C. Cau-dit-Coumes, F. Frizon, F. Leroux, G. Renaudin, *J. Am. Ceram. Soc.*, 2011, **94**, 261.

The presented work is published under the reference:

Crystal Structures of Calcium Hemicarboaluminate and Carbonated Calcium Hemicarboaluminate from Synchrotron Powder Diffraction Data
Acta Crystallographica Section B: Structural Science, 2012, **68**, 493
Tomče Runčevski, Robert E. Dinnebier,* Oksana V. Magdysyuk and Herbert Pöllmann

Author contributions: T. R. did the experimental work, analysed the XRPD data and solved the crystal structures, recorded and analysed the vibrational spectra (not shown in the Thesis) and wrote the article.

H. P. provided the sample and did the SEM image, O. V. M. helped in preparing the figures with the program JANA. R. E. D. initiated and coordinated the project.

3.2. Structural Characterization and *In Situ* followed Thermal Decomposition of a novel Magnesium Oxysulphate Hydrate Phase

A new magnesium oxysulphate hydrate phase, $5Mg(OH)_2 \cdot MgSO_4 \cdot 7H_2O$*, with a positive influence on the compressive strength of magnesium-based cements was structurally characterized. It crystallizes in form of micro-sized needles. The crystal packing is made of infinite, triple* MgO_6 *chains, intercalated by sulphate groups, water molecules and hydroxide anions. Rietveld refinement of the structure indicated a model in which the interchain region is characterized by presence of statistically distributed and dynamically disordered water molecules and anions. The high temperature behaviour and the decomposition processes were studied by thermal analyses and in situ XRPD, revealing five decomposition stages with MgO as a final product.*

3.2.1 Introduction

Sorel cement phases (magnesium oxychlorides) have some superior properties over ordinary Portland cements. (1) Their sulphate analogues, magnesium oxysulphates or MOS cements, are even more interesting because they do not present a potential source of corrosion in the production of reinforced steel. (2) Due to the needle-like morphology they are good binder systems. At high temperatures they transform into MgO, which has high melting point and provides high fire resistance. Moreover, the crystallographically free water in the structure is released at high temperatures and it creates water vapor that serves as fire retardant and smoke suppressant. MOSs, in addition, have low thermal conductivity. It should be mentioned that the density of all magnesium based cement is significantly lower than the density of Portland cements. Because of these properties, MOS phases can find use as fire resistive materials, reinforcement additives for plastics, functional materials with a whisker microstructure, flake powders, variety of nano-sized materials and in commercial production of lightweight insulating boards and panels. (3)

Among the major drawbacks for large-scale applications of MOSs is their low mechanical strength. Testing the influence of the composition, fly ash and citric acid to the compressive strength, it was noticed that the maximum strength was observed when the MgO/$MgSO_4$ molar ratio during the synthesis of these phases equaled 5 (Fig. 3.2.1a). (4) Using this reactants ratio, a new MOS phase was crystallized, with chemical formula $5Mg(OH)_2 \cdot MgSO_4 \cdot 7H_2O$ (abbreviated as 5-1-7). Due to the positive influence on the mechanical characteristics and the needle-like morphology shown in Fig. 3.2.1b (which is a promising feature for growing low dimensional, micro- and nano-whiskers), special attention was paid on its structural characterization. Its crystal structure was solved and refined using laboratory XRPD. The high temperature behavior and decomposition processes were studied by thermal analyses (TGA and DSC). Surprisingly, the expected decomposition scheme was not confirmed by the thermal experiments. In order to clarify what happens with the compound upon heating, temperature-variable *in situ* XRPD study was undertaken.

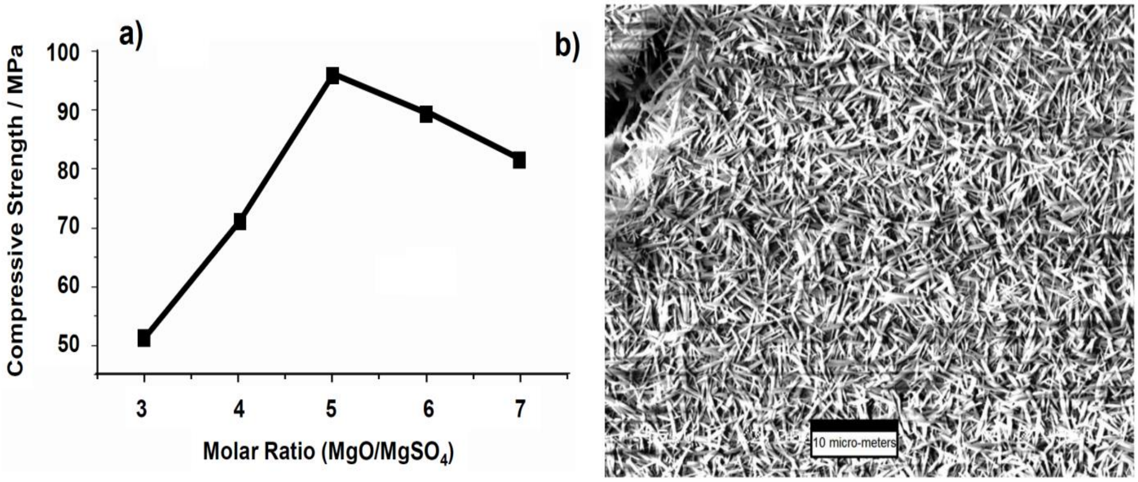

Figure 3.2.1. *a) Plot of the compressive strength value against the MgO/$MgSO_4$ molar ratio of the reacting paste. b) SEM images of the 5-1-7 phase, showing micro-sized needles morphology of the sample.*

3.2.2. Results and Discussion

The crystal structure of the 5-1-7 phase was solved *ab initio* from powder diffraction data. Figure 3.2.2a presents the crystal packing made of infinite triple chains of condense MgO_6 octahedra, intercalated by hydroxide anions, water molecules and rotationally disordered sulphate tetrahedra. The hydroxide anions and/or water molecules and the sulphate tetrahedra are statistically distributed at the same crystallographic position, with occupancies of 0.5 : 0.5.

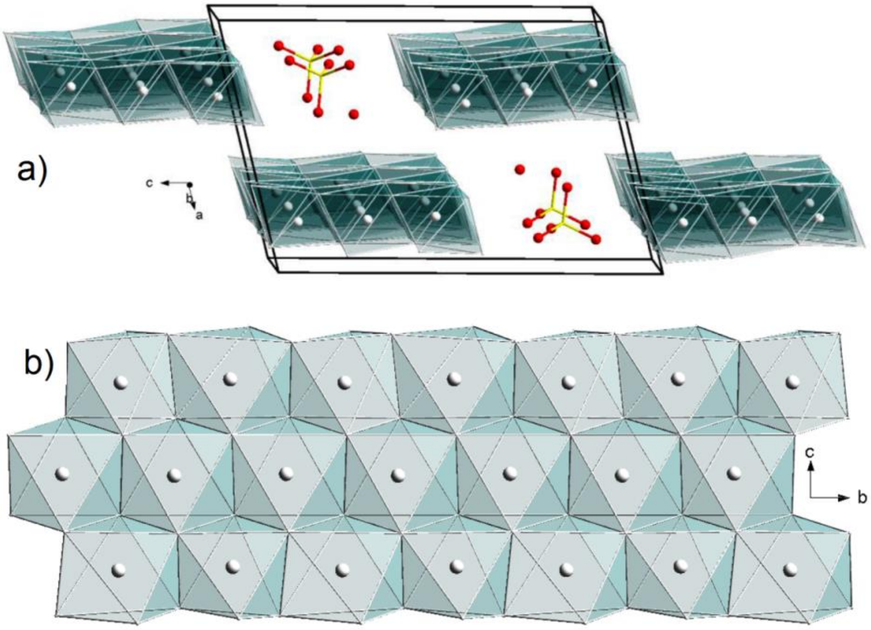

Figure 3.2.2. *a) Crystal packing of the 5-1-7 phase and b) sheet of infinite MgO_6 triple chains. Magnesium atoms are in white, oxygen atoms in red (and white when part of the octahedra) and sulphur atoms are in yellow. Hydrogen atoms are omitted for clarity.*

This crystal structure shows remarkable similarity to the structure of the $5Mg(OH)_2 \cdot MgCl_2 \cdot 8H_2O$ phase. (5) The infinite triple chains run along the crystallographic *b*-axis (Fig. 3.2.2b). The distorted octahedron around the magnesium atom centered in the middle of the triple chain shares six out of the twelve edges and all of its six corners with four neighboring octahedra. The octahedra formed by oxygen atoms coordinating the outer magnesium cations share three corners with two and two corners with one neighboring octahedron. Due to the limitations of the powder diffraction technique, the positions of the hydrogen atoms cannot be unambiguously determined.

Therefore, the distinction between the hydroxide and water species in the structure was assumed applying Pauling's rules. Namely, the protruding corners of the octahedra must be occupied by water molecules, while the corners shared by three octahedra can be occupied only by hydroxide anions. The corners shared by two octahedra can be occupied either by water molecules or hydroxide anions. When the charge balance was considered, two ordered and one statistically disordered alternative remained (Fig. 3.2.3).

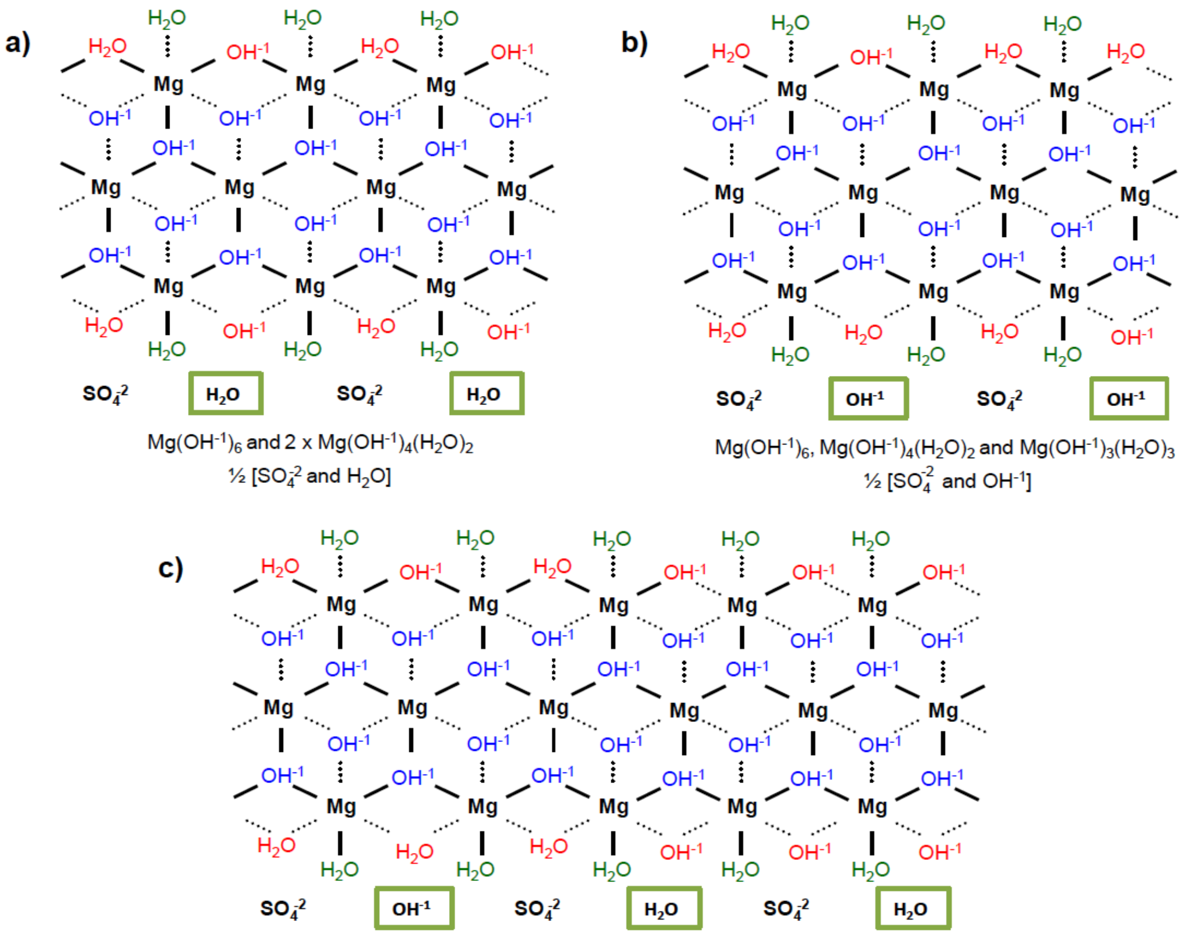

$Mg(OH^{-1})_6$ and 2 x $Mg(OH^{-1})_4(H_2O)_2$
½ [SO_4^{-2} and H_2O]

$Mg(OH^{-1})_6$, $Mg(OH^{-1})_4(H_2O)_2$ and $Mg(OH^{-1})_3(H_2O)_3$
½ [SO_4^{-2} and OH^{-1}]

Figure 3.2.3. *Representation of the composition of the magnesium octahedra in the infinite triple chains made of a) one* $Mg(OH)_6$ *and two* $Mg(OH)_4(H_2O)_2$ *octahedra, b) one* $Mg(OH)_6$*, one* $Mg(OH)_4(H_2O)_2$ *and one* $Mg(OH)_3(H_2O)_3$ *octahedron. c) Statistical distribution of water molecules and hydroxide anions in the interstitial region and the chains is assumed. The full lines present bonds to oxygen atoms above the plane of the magnesium atoms, the dotted lines present bonds to oxygen atoms below the plane.*

According to the crystal packing and the chemical formula ($5Mg(OH)_2 \cdot MgSO_4 \cdot 7H_2O$) a four-step decomposition scheme can be assumed: (I) Loss of the water molecules or hydroxide anions which are loosely bond and placed in the interstitial region, with a theoretical weight loss of 3.57 %. (II) Removal of six water molecules and/or hydroxide anions (which results in changing the structure of the chains), with a theoretical weight loss of 21.43 %. (III) Further loss of mass and producing magnesium oxide and magnesium sulphate, with a theoretical weight loss of 17.86 %. (IV) Final decay of the sulphate group by removal of SO_3, with a theoretical weight loss of 15.87 %, and the production of magnesium oxide.

In the experimentally obtained TG curve four mass loss steps were detected and four endothermic peaks were defined in the DSC curve, centered at 123 ^{0}C, 142 ^{0}C, 411.8 ^{0}C and 960 ^{0}C (Fig. 3.2.4a). The measured mass loss for the first step is ca. 8 %, indicating that minimum two water molecules are lost. In order to explain this observation the process of dehydration was monitored by *in situ* XRPD, following the structural changes on heating (Fig. 3.2.4b). In the temperature range from 303 to 396 K (corresponding to the first step in the measured TG curve), two phase transitions are visible: the 5-1-7 phase is stable up to 52 ^{0}C and decomposes into another phase which is stable up to 123 ^{0}C. Accordingly, the first step in the TG curve corresponds to two transitions and it can be assumed that two water molecules are lost at a time, thus an intermediate phase with the 5-1-6 stoichiometry is formed. The first transition is not defined in the DSC curve, while the second transition is evidenced with a sharp peak. The later observation fits nicely to the structural features. Namely, the first water molecule (or hydroxide anion) is loosely bonded and placed in the interchain region, thus the removal from the structure occurs continuously, with small changes in the overall energy. Removing the crystallographically bonded water molecule is a physical process which requires a significant amount of energy, therefore its effect is clearly visible in the DSC curve. The second weight loss step in the TGA curve represents the removal of five water molecules, the experimentally measured value of 18 % is in accordance with the theoretically calculated value of 17.86 %, and the new phase formed is stable from 123 to 150 ^{0}C. These phases, formed on heating, are most likely built by infinite sheets of magnesium octahedra without free water molecules. During the third step in the TG curve, 16 % weight loss is measured and a mixture of magnesium oxide/magnesium sulphate is confirmed by the collected PXRD pattern. Finally, during the last step, 16 % weight loss is observed, as expected after removing the sulphate group in form of SO_3 (with the theoretically calculated value being 15.87 %).

Based on the results obtained by the TG and DSC analyses, and clarified by the results from the *in situ* XRPD analyses, the decomposition process of the 5-1-7 phase is explained by the following chemical reactions:

$5Mg(OH)_2{\cdot}MgSO_4{\cdot}7H_2O$	$\rightarrow$	$5Mg(OH)_2{\cdot}MgSO_4{\cdot}6H_2O + H_2O$	[ca. 50 ^{0}C]
$5Mg(OH)_2{\cdot}MgSO_4{\cdot}6H_2O$	$\rightarrow$	$5Mg(OH)_2{\cdot}MgSO_4{\cdot}5H_2O + H_2O$	[ca. 90 ^{0}C]
$5Mg(OH)_2{\cdot}MgSO_4{\cdot}5H_2O$	$\rightarrow$	$5Mg(OH)_2{\cdot}MgSO_4 + 5H_2O$	[ca. 180 ^{0}C]
$5Mg(OH)_2{\cdot}MgSO_4$	$\rightarrow$	$5MgO + MgSO_4 + 5H_2O$	[ca. 410 ^{0}C]
$5MgO + MgSO_4$	$\rightarrow$	$6MgO + SO_3$	[ca. 950 ^{0}C]

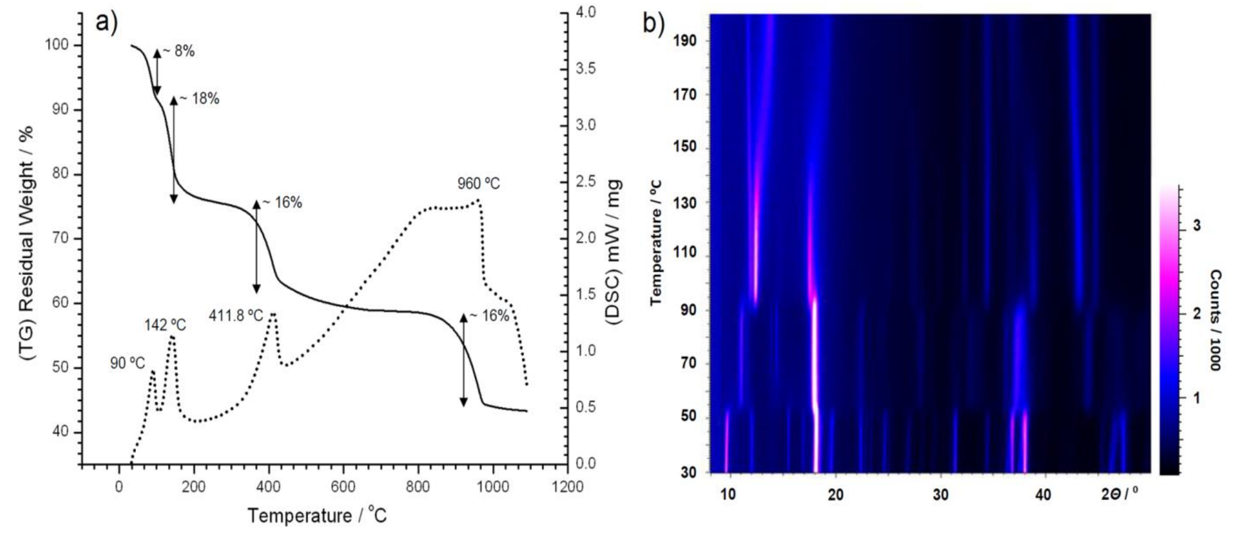

Figure 3.2.4. *a) TG curve (solid line, left vertical axis) and DSC curve (dotted line, right vertical axis) of the 5-1-7 phase. b) Two-dimensional projection of the observed scattered X-ray intensity for 5-1-7 phase as a function of diffraction angle and temperature. The intensity (counts) is colour coded.*

3.2.3 Conclusions

A new magnesium oxysulphate phase (with a 5-1-7 stoichiometry) whit a positive influence on the compressive strength of MOS cements, was structurally characterized. It crystallized in a structure built by infinite triple chains of magnesium octahedra, intercalated with sulphate tetrahedra, water molecules and hydroxide anions. The magnesium chains are ordered and running along the crystallographic *b*-axis, whereas the interchain region is characterized by statistical disorder, where the SO_4 tetrahedra are distributed with occupancy of 0.5 and the rest of the positions are occupied by water molecules and/or hydroxide anions. In addition to the statistical disorder, dynamic disorder in respect to the hydrogen bond network can be assumed. The high temperature behavior of the phase was studied by thermal analyses (TG and DSC). The first inspection of the experimental data did not corresponded to the theoretically assumed decomposition scheme. Only after performing detailed *in situ* XRPD investigations, a decomposition model was presented, where the thermally induced mass loss process was explained by five thermoinduced decomposition steps.

3.2.4 Experimental Section

Instrumentation

The diffraction pattern of the 5-1-7 phase (Fig. 3.2.5) was collected on a D8 Advance powder diffractometer [Bruker, Cu$K\alpha_1$, radiation from primary Ge(111)-Johannson-type monochromator, Våntag-1 position sensitive detector (PSD), with an opening angle of 6^o] in Debye-Scherrer geometry for a period of 24 h. Data were taken in steps of 0.009^o in 2θ at a scanning speed of 10 s/step.

Sample Purity and Preparation

The sample was found to be phase pure and it was subjected to data collection without pervious treatment, except of manual powdering in a pestle. The sample was sealed in a borosilicate glass capillary of 0.5 mm diameter (Hilgenberg glass No. 50), which was spun during the measurement for better particles' statistics.

Structure Solution and Rietveld Refinement

The TOPAS 4.2 program was used for indexing, crystal structure solution and refinement. (6a) The autoindexing was performed from first principles by the iterative use of singular value decomposition. The indexing procedure indicated an *I*-cantered monoclinic unit cell. When the observed extinction rules were examined, the most probable space groups were found to be *I*2/*m*(*C*2/*m*) (12) or *I*121(*C*121). From volume increments, *Z* was determined to be 4. Precise lattice parameters were determined by a Pawley fit. (6b)

The structure determination was performed in the *I*121 space group by the method of Charge Flipping (CF), (6c,d) and Simulating Annealing (SA). (6e) Using CF, the positions of the magnesium and oxygen atoms in the triple chains were found. By visual inspection, falsely assigned atom types were detected and corrected. The CF indicated that the region between the chains is characterized by a disorder, and its structure was determined by SA. The occupancies of the oxygen and sulphate were refined during the SA runs, whether all other peak-profile parameters were kept fix.

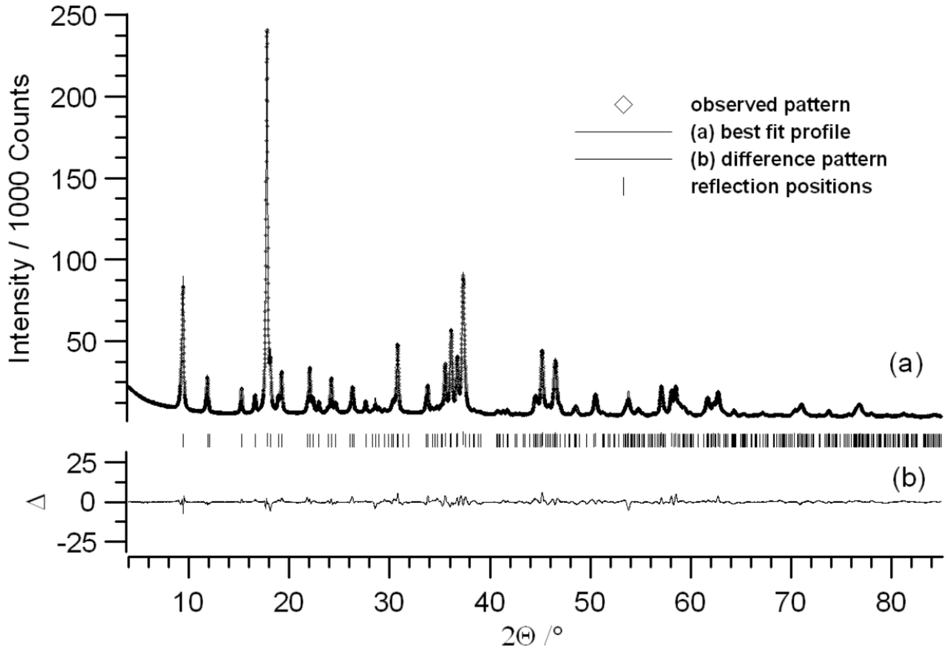

Figure 3.2.5. *Rietveld plot of the scattered X-ray intensities of the 5-1-7 phase as a function of diffraction angle at ambient conditions.*

For the final Rietveld refinement, (6f) all profile and lattice parameters were subjected to free unconstrained refinement and the final plot is shown as Fig. 3.2.5. The agreement factors (*R*-values) are listed in Table 3.2.1, together with selected crystallographic data. When the difference electron density map was examined, minor amounts of excess electron density were detected in the interstitial sites. This residual density can most likely be attributed to small amounts of absorbed and reacted CO_2 form the atmosphere, in the form of carbonate phases.

Table 3.2.1. *Crystallographic and Rietveld refinement data for the 5-1-7 phase.*

Compound name	Magnesium Oxysulphate
Molecular formula	$Mg_6(OH)_{10}SO_4 \cdot 7H_2O$
Wavelength (Å)	1.540596
Starting and final angle (° 2θ)	4.00 and 90.00
Data collection (s/step)	10
Temperature (°C)	25
Space group, Z	I121 (C121) (5), 4
a (Å), b (Å), c (Å)	10.260(3), 6.307(1), 15.138(3)
β (°), V (Å^3)	103.98(2), 950.6(4)
R−Bragg (%) [(a)]	3.897
R–exp (%)[(a)]	0.086
R–p (%) [(a)]	5.311
R–wp (%) [(a)]	6.868
No. of variables	74

(a) The figures of merit are as defined in TOPAS 4.2.

References

(1) a) S. Sorel, *Comp. Rend.* 1867, **65**, 102; b) J. Bensted, P. Barnes, *Structure and Performance of Cements.* 2nd edition. Spon Press, London, 2002; c) Z. Li, C. K. Chau, *Cem. Concr. Res.* 2007, **37**, 866; d) E. Kirk, D. F. Othmer, *Encyclopedia of Chemical Technology* vol 3, Wiley-Interscience, Weinheim, 435, 1996.

(2) a) T. Demediuk, W. F. Cole, *J. Aust. Chem.* 1957, **3**, 287, 1957; b) J. J. Beaudoin, V. S. Ramachandran, *Cem. Concr. Res.* 1978, **8**, 103, 1978; c) L. Urwongse, C. A. Sorrell, *J. Am. Ceram. Soc.* 1980, **63**, 532.

(3) a) S. Hoshino, H. Tanaka, T. Kimura, *Plastics Eng.* 1983, **39**, 35; b) X. Yan, D. Xu, D. Xue, *Acta Mater.* 2007, **55**, 5747; c) J. G. Fu, W. Liang, H. Wang, Z. H. He, *J. Cent. South Univ. Technol.* 2011, **6**, 1871; d) X. T. Sun, W. T. Shi, L. Xiang, W. C. Zhu, *Nanoscale Res. Lett.* 2008, **3**, 386.

(4) **C.** Wu, H. Yu, J. Dong, Y. Li, J. Wen, L. Zheng, Y. Tan, *Modified Magnesium Oxysulfate Cement*, 201210511700.8. China (Patent).

(5) K. Sugimoto, R. E. Dinnebier, T. Schlecht, *Acta Crystallogr.* 2007, **B63**, 805.

(6) a) TOPAS version 4.2, 2007, Bruker-AXS, Karlsruhe, Germany; b) G. S. Pawley, *J. Appl. Cryst.*, 1981, **14**, 357; c) G. Ozlányi, A. Süto, *Acta Crystallog.*, 2004, **A60**, 134; d) J. Karle, H. Hauptman, *Acta Crystallog.*, 1956, **9**, 635; e) Y. G. Andreev, G. S. MacGlashan, P. G. Bruce, *Phys. Rev.*, 1997, **B55**, 12011; f) H. M. Rietveld, *J. Appl. Cryst.*, 1969, **2**, 65.

The presented work is published under the reference:

Structural Characterization of a New Magnesium Oxysulphate Hydrate Cement Phase and its Surface Reactions with Atmospheric Carbon Dioxide

Journal of the American Ceramic Society 2013, **96**, 3609

Tomče Runčevski, Chengyou Wu*, Hongfa Yu, Bo Yang and Robert E. Dinnebier*

Author contributions: T. R. planed the project, did the experimental work, analysed the XRPD data, solved the crystal structures, analysed the vibrational spectra (not shown in the Thesis) and wrote the article.

C. W., H.Y. and B.Y. initiated the project, provided the sample, prepared the SEM image, made Fig. 3.2.1 and recorded the TG/DSC curves (Fig. 3.2.4a). R. E. D. coordinated the project.

3.3. Dehydration of the Sorel Cement Phase $3Mg(OH)_2 \cdot MgCl_2 \cdot 8H_2O$ Studied by *In Situ* Synchrotron X-Ray Powder Diffraction

Dehydration is an important process which affects the chemical, physical and mechanical properties of materials. The thermally-induced dehydration of $3Mg(OH)_2 \cdot MgCl_2 \cdot 8H_2O$ *was studied by in situ synchrotron X-ray powder diffraction, complemented by thermal analyses. Attention was paid on the determination of the chemical composition and crystal structure of the lower hydrates at high temperatures, identified as the phases* $3Mg(OH)_2 \cdot MgCl_2 \cdot 5.4H_2O$ *and* $3Mg(OH)_2 \cdot MgCl_2 \cdot 4.6H_2O$*. The crystal structure of the former was solved and refined by the Rietveld method and a structural model for the latter was proposed. A detailed scheme of the temperature induced phase transformations, in the range from 25 ºC to 500 ºC, resulted.*

3.3.1. Introduction

Two of the most important Sorel cement phases are the $3Mg(OH)_2 \cdot MgCl_2 \cdot 8H_2O$ (abbreviated as 3-1-8) and $5Mg(OH)_2 \cdot MgCl_2 \cdot 8H_2O$ (abbreviated as 5-1-8) phases. (1) They are of interest to the industry because of their high compressive and flexural strength, high fire resistance, low thermal conductivity, high resistance to abrasion, etc. Accordingly, they are used as floor materials, bonding agents in wet stones applications, for production of artificial ivory, grindstones, cast stones, tiles, among others. The 3-1-8 phase is used as a barrier construction material in salts formations, because it is stable toward Mg^{2+} containing salts and solutions. Due to this quality, it is tested for application in final disposal concepts for radioactive waste. (1, 2)

Knowing the high-temperature behaviour, especially upon dehydration, of cementitious materials is crucial for optimizing their performance. According to earlier studies, the composition of the 3-1-8 phase changes on heating to compositions with stoichiometries of 3-1-5, 3-1-4, and 3-1-0. (3) *In situ* XRPD studies on Sorel phases were performed, unfortunately without any success in detailing the corresponding crystal structures. (4) In order to fill the gap in the structural knowledge, new *in situ* crystallographic and thermal studies were undertaken and a structural picture of the thermal behaviour was successfully drawn.

3.3.2. Results and Discussion

Figure 3.3.1a presents a 2D projection of the observed scattered X-ray intensity as a function of diffraction angle and temperature. The processes at higher temperatures then 170 ºC were already reported and discussed in a previous study. (5) Three regions are observed in the projection: the first one (T < 100 ºC) corresponds to the scattered intensity from the 3-1-8 phase and the following two (100 ºC < T < 130 ºC and 130 ºC < T < 170 ºC) to the scattering intensity from the newly formed lower hydrates. The overlap of the diffraction peaks from different phases at the borders of the thermal regions indicates that the phase transitions among them are not sharp, but occur gradually in a given thermal interval with a continuous water loss.

In order to establish the temperature ranges where the lower hydrates exist as thermodynamically stable structures, and to calculate the water amount which is lost during the dehydration, combined TG/DTA analyses were performed (Fig. 3.3.1b). It was found that the dehydration process starts at about 80 °C and between 115 °C and 120 °C the first lower hydrate is the major phase of the system. The TG curve indicated that 2.6 water molecules are lost, thus the newly formed phase has a 3-1-5.4 stoichiometry. By further heating, continuous water loss is evidenced, accompanied by smaller endothermic effects. During that process a second lower hydrate is formed. The weight loss reaches a value of –14 %, which corresponds to a loss of 3.4 water molecules, thus the second phase has a 3-1-4.6 stoichiometry. Increasing the temperature to values higher than 200 ºC leads to formation of the previously reported anhydrous magnesium hydroychlorides. (5) These phases decompose at temperature higher than 400 ºC, giving MgO as the final dehydration/decomposition product of the Sorel phases. Based on the thermal and crystallographic analyses, the following scheme results:

$3Mg(OH)_2·MgCl_2·8H_2O \rightarrow 3Mg(OH)_2·MgCl_2·5.4H_2O + 2.6H_2O$

$3Mg(OH)_2·MgCl_2·5.4H_2O \rightarrow 3Mg(OH)_2·MgCl_2·4.6H_2O + 0.8H_2O$

$3Mg(OH)_2·MgCl_2·4.6H_2O \rightarrow 4[Mg(OH)_{x>1.67}Cl_{y<0.33} + Mg(OH)_{x<1.5}Cl_{y>0.5}] + 4.6\ H_2O \quad (x+y=1)$

$4[Mg(OH)_{x>1.67}Cl_{y<0.33} + Mg(OH)_{x<1.5}Cl_{y>0.5}] \rightarrow 4MgO + 2HCl + 2H_2O \quad (x+y=1)$

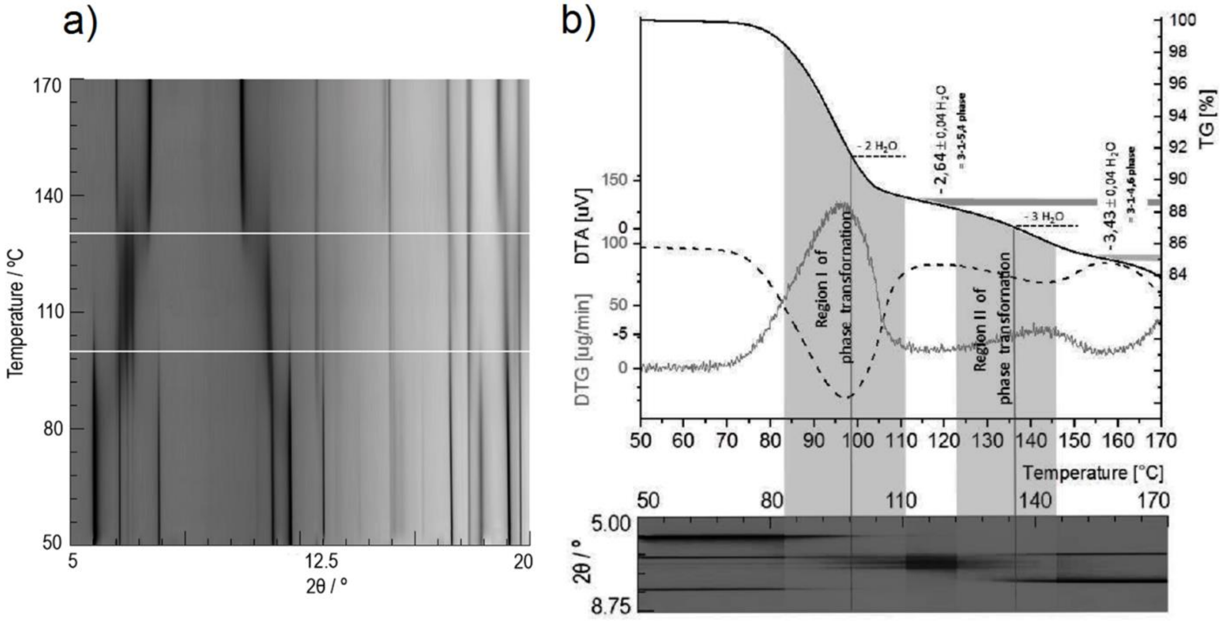

Figure 3.3.1. *a) 2D projection of the observed scattered X-ray intensity of the 3-1-8 phase as a function of diffraction angle and temperature. Three temperature ranges are identified and separated by the white lines: the first one corresponds to the 3-1-8 phase, and the following two to the lower hydrate phases formed on heating. b) Overlay of thermal analyses and the in situ 2D XRPD plot. DTA and DTG curves (left axis) and TG curve (right axis). The two temperature regions of phase transformations are highlighted.*

Although the crystal structure of the 3-1-8 phase has been known for almost 60 years, there are no reported structure determinations of the crystal structures of the lower hydrates. The main reason for that is the fact that these materials do not exist in form of crystals suitable for single crystal diffraction. Crystals of the Sorel phases exhibit severe defects and pronounced stacking faults in their crystal structures, making the process of structure solution even bigger challenge. In the scope of this work, high-resolution powder patterns were collected *in situ*, by gradually increasing the temperature. Up to ca. 80 ^{0}C, the 3-1-8 phase was shown to be stable. This phase exhibits the already reported crystal structure, (1) built of MgO_6 octahedra arranged in infinite double chains, running in the direction of the crystallographic *b*-axis, with an interchain region that accommodates chloride anions and water molecules (Fig. 3.3.2a). The first dehydration product exhibits very low crystallinity and pronounced stacking defects, which are clearly visible in the shape and intensity of the peaks in the diffraction patterns. As a result, only a tentative model of the crystal structure can be derived. This structural model is shown in Fig. 3.3.2b and presents an expected intermediate phase of 3-1-8 and the second lower hydrate. According to the thermal analyses, the stoichiometry of this phase is 3-1-5.4. The model indicates that there is a statistical distribution of chloride and oxygen species, positioned at the same crystallographic sites in the unit cell. Further heating results in additional loss of water molecules, and the stoichiometry changes to 3-1-4.6. The diffraction data quality of this phase was higher compared to the former hydrate (the peak's shape and intensities indicated the presence of stacking faults and similar defects, but far less severe as in the case of the 3-1-5.4 phase). The crystal structure of this phase was solved and successfully refined by the Rietveld method. There, all of the water molecules and hydroxide and chloride anions are statistically distributed at the edges of the Mg octahedra and there are no atoms between chains (Fig. 3.3.2c).

To visualize the changes of the phase amounts on the course of the dehydration processes, quantitative parametric Rietveld analysis was performed. (6) Figure 3.3.3 shows the phase evolution in a given temperature range (from 50 ºC to 170 ºC, 3 K/min). From room temperature to 100 ºC the 3-1-8 phase is the only phase present; from 100 ºC to 118 ºC there is a mixture of the 3-1-8 and 3-1-5.4 phases. The 3-1-5.4 phase occurs as pure phase in a short temperature interval (118 – 123 ºC) and thereafter it exists in a mixture with the 3-1-4.6 phase (up to 160 ºC). At temperatures greater than 170 ºC only the 3-1-4.6 phase is present.

3.3.3 Conclusions

Using *in situ* synchrotron X-ray powder diffraction and thermal analyses (TG/DTA) the high temperature behaviour of the Sorel cement phase 3-1-8 in the temperature range from 25 °C to 500 °C, was structurally and thermally characterized. By heating of the 3-1-8 phase, two phases are produced with stoichiometries of 3-1-5.4 and 3-1-4.6. The crystal structure of former was solved and refined by the Rietveld method and a structural model for the latter was proposed. Above ca. 200 °C the lower hydrates decompose in anhydrous magnesium hydrochlorides, which subsequently are getting dehydrated into magnesium oxide.

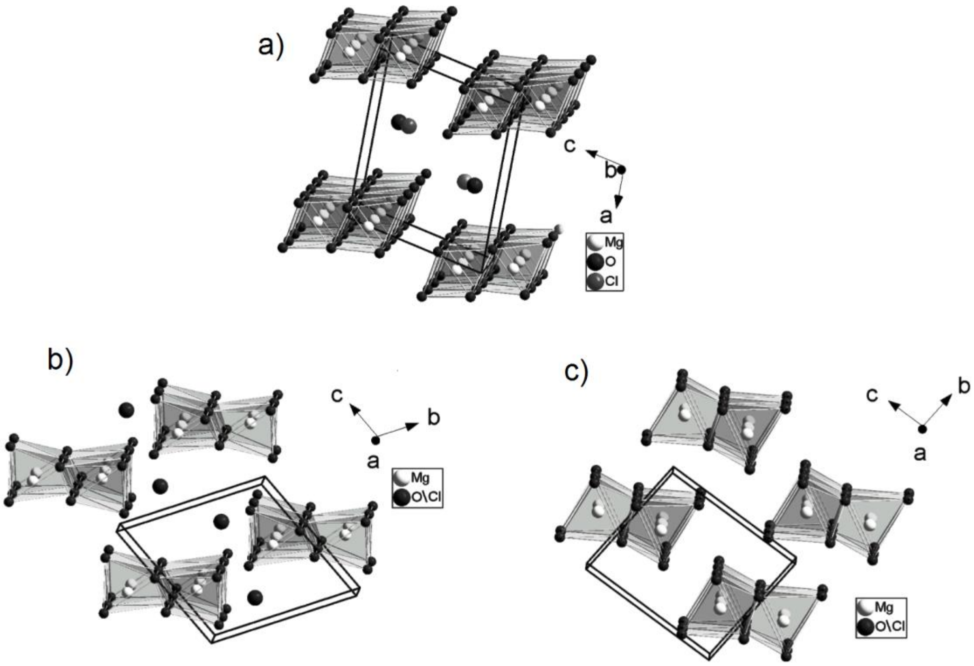

Figure 3.3.2. *Crystal packing diagrams of the a) 3-1-8, b) 3-1-5.4 and c) 3-1-4.6 phases. Semi-transparent magnesium octahedra characterized by statistical distribution of the anions are drawn. The hydrogen atoms are omitted for clarity.*

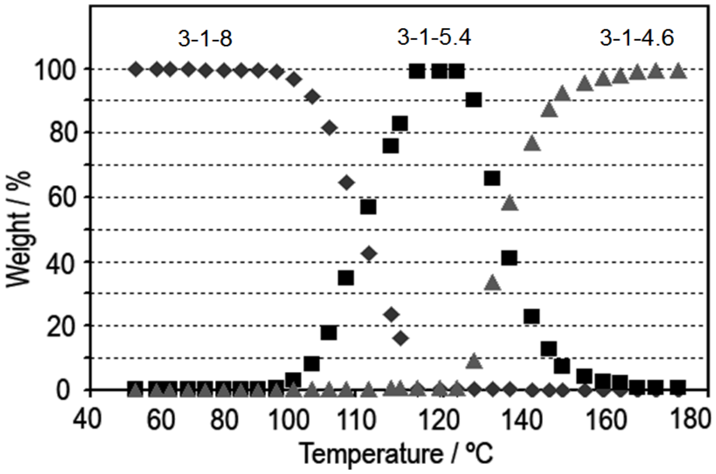

Figure 3.3.3. *Results of the quantitative parametric Rietveld analysis performed on data collected in situ on the course of the dehydration process of the 3-1-8 phase.*

3.3.4 Experimental Section

Instrumentation

The powder diffraction data were collected in the temperature range from 50 ºC to 170 ºC using the high-resolution powder diffractometer at the I11 beamline, located at the British national synchrotron facility, Diamond Light Source. The wavelength of radiation was determined from a silicon standard to be 0.826401(3) Å. The scans at each temperature were written continuously with 3 ºC/min and 14 s/frame.

Sample Purity and Preparation

The sample was placed in an open glass capillary (Hilgenberg glass No. 50), which was spun during data collection for better particle statistics.

Structure Solution and Rietveld Refinement

The powder pattern of 3-1-4.6 (Fig. 3.3.4) was indexed using the program suite TOPAS Version 4.2, (7a) and the extinctions of reflection found pointed at $P1$ or $P\bar{1}$ as possible space groups. The peak profiles and precise lattice parameters were determined by a Pawley fit, (7b) using the fundamental parameter approach. Chebyshev polynomials were used for the modelling of the background.

The crystal structure of the 3-1-4.6 phase was solved using the simulated annealing approach, (7c) and was subsequently refined by the Rietveld method. (7d) During the final Rietveld refinements the occupancies of the atoms were constrained to the stoichiometry estimated by the thermal analyses (the unconstrained refinement did not result in significantly lower figures of merit). The refinement data and the final agreement factors (*R*-values) are listed in Table 3.3.1, and the Rietveld plot is given in Fig. 3.3.4. The powder pattern is characterized by strong anisotropy of width and asymmetry of the Bragg reflection. Both phenomena were satisfactory modelled by a phenomenological approach using symmetry adapted spherical harmonics. Only the peak's widths and asymmetry were treated, and no intensity correction was applied. No attempt was made to physically model the complex peak shape suggesting severe stacking fault and other type of disorder.

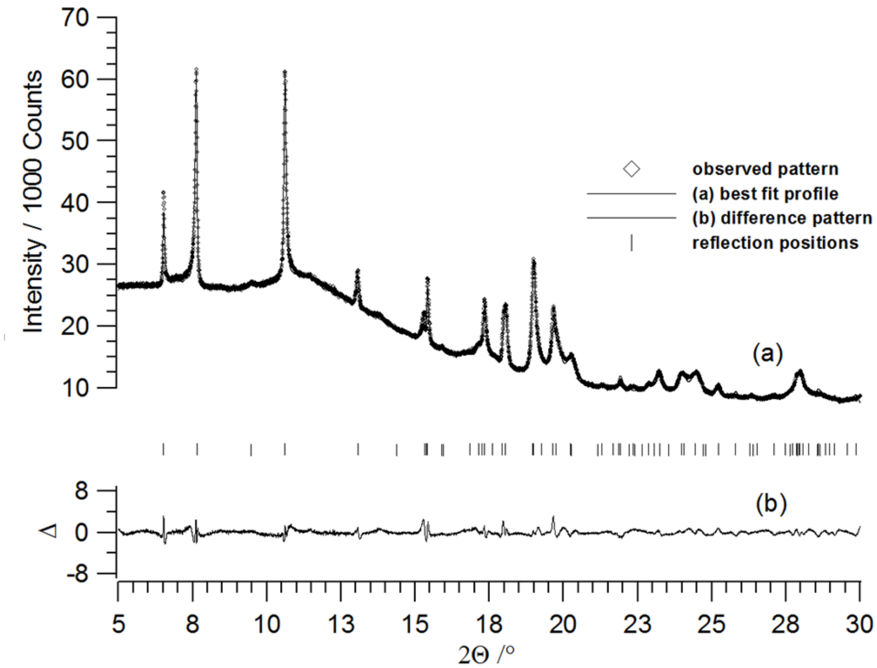

Figure 3.3.4. *Scattered X-ray intensities of 3-1-4.6 phase as a function of diffraction angle, collected at temperature of 160 °C.*

Table 3.3.1. *Crystallographic and Rietveld refinement data for 3-1-4.6 phase.*

Chemical System	3-1-4.6 phase
Molecular Formula	$3Mg(OH)_2 \cdot MgCl_2 \cdot 4.6H_2O$
Sum formula	$Mg_4Cl_2O_{10.6}H_{14.6}$
Space Group	*P*-1 (No. 2)
Z	2
a (Å), *b* (Å), *c* (Å)	3.158(4), 6.246(9), 7.48(1)
α (°), *β* (°), *γ* (°)	95.03(4), 102.34(6), 91.86(9)
Temperature (°C)	160
Density ($g \cdot cm^{-1}$)	2.116(5)

Data collection	2 ºC/min and 4 s/frame
Wavelength (Å)	0.826401(3)
Start and finish angle (º 2θ)	5 and 30
R−Bragg (%) (a)	0.89
R–p (%) (a)	1.86
R–p’ (%) (a)	15.7
R–exp (%) (a)	0.06
R–wp (%) (a)	2.48

(a) The figures of merit are as defined in TOPAS 4.2. (1)

References

(1) a) S. Sorel, M. Dumas, *C. R. Acad. Paris* 1976, **65**, 102; b) W. Feitknecht, *Helv. Chim. Acta* 1926, **9**, 1018; c) W. Feitknecht, F. Held, *Helv. Chim. Acta* 1927, **10**, 140; d) W. Feitknecht, F. Held, *Helv. Chim. Acta* 1930, **13**, 1380; e) W. Feitknecht, F. Held, *Helv. Chim. Acta* 1944, **27**, 1495; f) C. R. Bury, E. R. H. Davies, *J. Chem. Soc.* 1932, 2008; g) P. M. de Wolff, L. Walter-Levy, *Acta Crystallogr.* 1953, **6**, 40; h) K. Sugimoto, R. E. Dinnebier, T. Schlecht, *Acta Crystallogr*. 2007, **B63**, 805.

(2) Vorläufige Sicherheitsanalyse für den Standort Gorleben, AP 9.2, Integrität geotechnischer Barrieren, GRS Braunschweig, GRS 287 and GRS 288 (2013).

(3) a) W. F. Cole, T. Demediuk, *Aust. J. Chem.* 1955, **8**, 243; b) S. Xia, P. Xing, S. Gao, *Thermochim. Acta* 1991, **183**, 349.

(4) a) A. N. Christensen, P. Norby, J. C. Hanson, *J. Solid St. Chem.* 1995, **114**, 556; b) A. N. Christensen, P. Norby, J. C. Hanson, *Acta Chem. Scand.* 1995, **49**, 331.

(5) R. E. Dinnebier, I. Halasz, D. Freyer, J. C. Hanson, *Z. Anorg. Allg. Chem.* **2011**, 637, 1458.

(6) G. W. Stinton, J. O. S. Evans, *J. Appl. Crystallogr.* 2007, **40**, 87.

(7) a) TOPAS version 4.2, 2007, Bruker-AXS, Karlsruhe, Germany; b) G. S. Pawley, *J. Appl. Cryst.*, 1981, **14**, 357; c) Y. G. Andreev, G. S. MacGlashan, P. G. Bruce, *Phys. Rev.*, 1997, **B55**, 12011; d) H. M. Rietveld, *J. Appl. Cryst.*, 1969, **2**, 65.

The presented work is published under the reference:

Dehydration of the Sorel cement phase $3Mg(OH)_2 \cdot MgCl_2 \cdot 8H_2O$ studied by *In Situ* Synchrotron X-ray Powder Diffraction and Thermal Analyses
Zeitschrift für Anorganische und Allgemeine Chemie 2014, **640**, 100
Tomče Runčevski, Robert E. Dinnebier* and Daniela Freyer*

Author contributions: T. R. did the experimental work, analysed the XRPD data, solved the crystal structure, and wrote the article together with D. F.

D. F. provided the sample and performed the thermal analyses (Fig. 3.3.1b). R. E. D. initiated and coordinated the project.

3.4. *In Situ* Monitoring of the Thermosalient (Jumping Crystal) Effect of a Polymorphic Organometallic System, accompanied by Colossal Thermal Expansion

The thermosalient (TS) effect is an extremely rare propensity of some solids to be self-actuated by an active ballistic event when taken over a phase transition, whereby crystals travel over distances that can reach up to thousands times their size within seconds. Despite that this interesting phenomenon provides a conceptually new platform for direct conversion of heat into mechanical work, which is posed to push up the performance of organic actuators, it rather remains mechanistically poorly understood, in part due to lack of in situ structural studies. Herein, firm evidence that organometallic solids are capable of the TS effect is presented. Across the given temperature range, crystals switch among five molecular packings that are related by four phase transitions, one of which mechanically responsive. Moreover, some of the polymorphs exhibit anomalous and remarkably large thermal expansion where the volumetric expansion coefficients are among the record values reported for molecular solids thus far. The structural transition responsible for the TS effect was detailed for the first time from in situ collected XRPD data to reveal a mechanism where the thermally induced strain in the head-to-head stacked molecular layers is released by sliding of the layers atop each other.

3.4.1 Introduction

It was recently shown that mechanically active components and the related processes in living organisms can serve as important mechanistic and kinematic models for the design of artificial, biomimetic actuators. (1) Having the problems with the mechanical robustness in part resolved with the advent of crystal engineering, and being capable of fast energy transfer by virtue of very dense and highly ordered packing, mechanically responsive single crystals are now evolving as a new platform for rapid actuation at macroscopic level. Crystals capable of mechanical effects such as reshaping (twisting, rolling or bending) or displacement by effective locomotion (crawling, creeping, hopping and slithering) are prospective for the design of biomimetic and technomimetic mechanically responsive elements, including artificial tissues and dynamic components in microfluidic mechanics. (2) The ultrafast energy transfer and efficient coupling between the thermal/light energy and mechanical energy typical for the dense packing of small-molecule crystals stand as main assets of single crystals towards the design of fast and ultrafast actuators. The assessment and optimization of the performance of such technomimetic and biomimetic single crystalline actuators necessitates an in-depth understanding of the underlying dynamic atomic-scale processes. Whether the self-acutation of crystals is generally caused by a sharp, first-order phase transition, the continuous change of the habit upon thermal treatment is inevitably related to the thermal expansion, a well-understood physical phenomenon characterized by the relative rate at which a material expands (α), which usually falls within the interval 0×10^{-6} $K^{-1} < \alpha < 20 \times 10^{-6}$ K^{-1}. Examples of unconventional thermal expansion, such as negative thermal expansion or exceptionally large values of α, are of special interest as they often highlight important physical processes in the respective materials. (3)

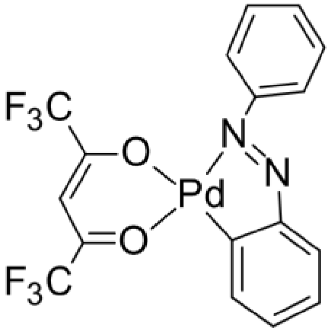

Figure 3.4.1. *Molecular formula of (phenylazophenyl)palladium(II) hexafluoroacetylacetonate (PHA).*

It was previously reported that crystals of (phenylazophenyl)palladium(II) hexafluoroacetylacetonate (PHA, Fig. 3.4.1) when heated on one side “literally fly off the hot stage”. (4) This note of crystal motility was to become the first documented report of the thermosalient effect (TS), the propensity of certain crystals to hop and leap when taken over a phase transition. The processes behind the leaping effect have remained a mystery for three decades. One of the reasons for the lack of knowledge on this remarkable system was the need for high-resolution, time- and temperature-resolved *in situ* studies. To decipher the mechanism, the trigger and the driving force behind the TS effect and to elucidate the interplay between the thermodynamic and kinetic factors for its occurrence, the crystal structures before and after the phase transition needed to be detailed. As shown in Fig. 3.4.2, very often the single crystals cannot withstand the stress generated upon the phase transition, and therefore disintegrate. This disintegration hampers the applicability of single crystal diffraction, leaving XRPD as the remaining method of choice. In addition, XRPD is a perfect method for following unit cell changes on heating/cooling, thus studying the thermal expansion phenomena.

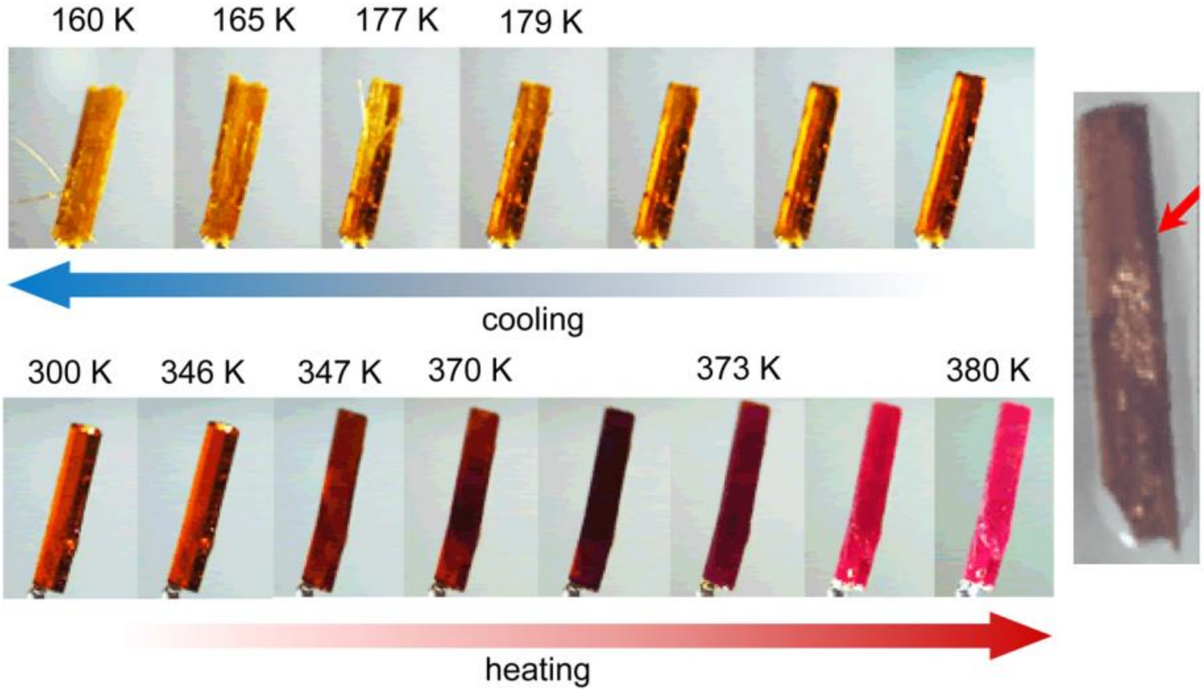

Figure 3.4.2. *Disintegration of a single crystal of PHA upon cooling and heating. The inset picture on the left shows progression of the phase transition in a single crystal of PHA, effectively powdering the crystal.*

The results presented herein unravelled extraordinary crystal chemistry: PHA exists as five polymorphs that are related by four phase transitions. At least two phases exhibit large positive thermal expansion (PTE) of the crystallographic axes, while one of them undergoes uniaxial negative thermal expansion (NTE), an extremely rare property. In addition, some of the highest thermal expansion coefficients among the known molecular solids were recorded. This fortuitous combination of exceptional properties provided unique opportunity to directly relate the NTE and PTE with the TS effect in different structural polymorphs of the same compound. Moreover, for the first time, a clear link between the anomalous thermal expansion and the mechanical response was established, with both being rooted in the susceptibility of this material to internal strain.

3.4.2 Results and Discussion

PHA was prepared according to a previously published procedure, which yielded two forms stable at room temperature (RT), identified by XRPD as the yellow (α) and the red (β) polymorph with reported crystal structures. (4)

In order to follow the phase transitions and to investigate for new polymorphs, the thermal behaviour of both phases was monitored by *in situ* XRPD on cooling and subsequent heating. As shown in Fig. 3.4.3, on cooling form α gradually transforms into a new polymorph named form δ *via* a second order phase transition. On cooling to even lower temperatures form δ transforms into another, new polymorph named form ε *via* a sharp first order phase transition. Figure 3.4.4 presents a more detailed view on the changes of the scattered X-ray intensity as a function of temperature, further indicating that the first transition is of second order, whereas the second transition is of first order. As it can be seen in both figures, the transitions are completely reversible and mirrored on heating. Due to the disintegration of the single crystal of form α on cooling (Fig. 3.4.2), the crystal structure of form ε was solved *ab inito* by XRPD using synchrotron X-ray radiation. The crystal structure of form δ remained unsolved, owning to the fact that it is metastable and coexists with form α in a mixture which relative amount is not constant but rapidly changing with temperature. Nevertheless, taken that this structure is connected to the crystal structure of form α *via* second order phase transition, great similarity between them is expected.

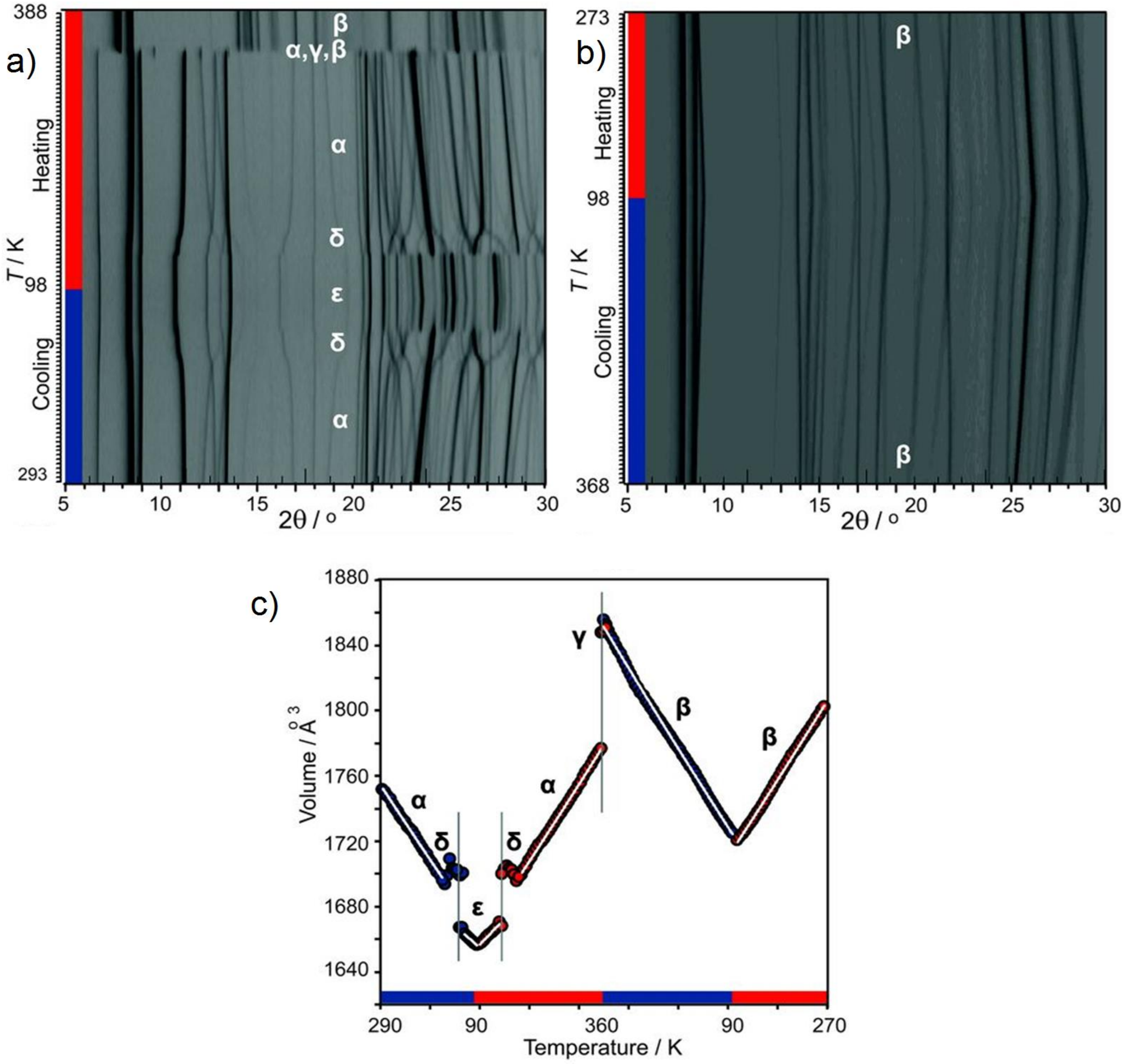

Figure 3.4.3. *Thermally-induced changes of PHA: a) and b) present the phase transitions monitored by temperature-resolved X-ray powder diffraction; in c) the change of the unit cell volume with temperature data is given (the volumes of forms γ and β were multiplied by 2 to bring them on the same number of molecules per unit cell as in α).*

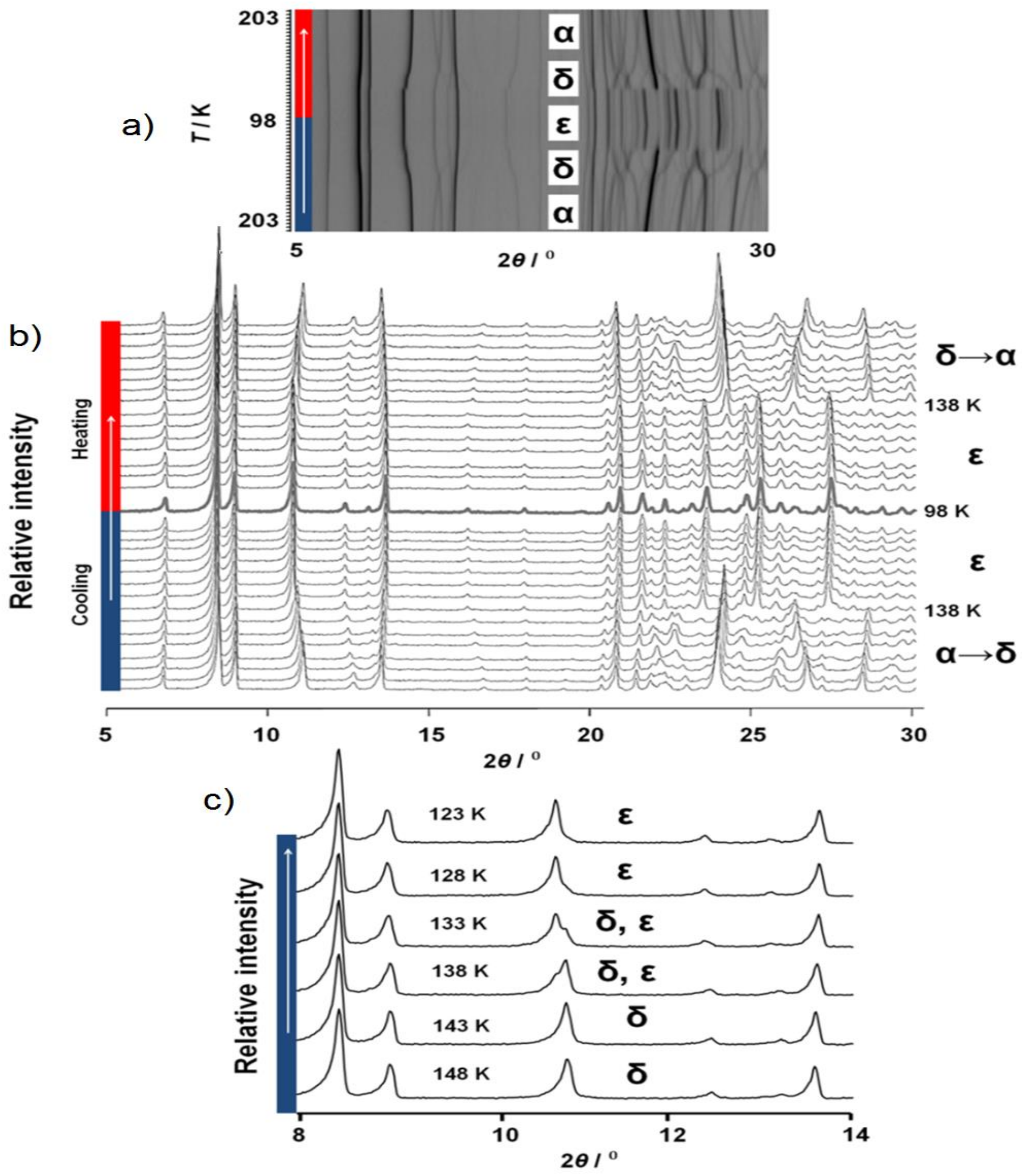

Figure 3.4.4. *a) 2D projection of the observed X-ray scattered intensity of PHA plotted as a function of diffraction angle and temperature, which shows four phase transitions on cooling to 98 K and subsequent heating. b) The scattered intensity in the diffraction patterns changes continuously during the first transition of cooling (α ↔ δ) followed by a sharp change (δ ↔ ε). Accordingly, it can be concluded that the first phase transition (α ↔ δ) is of second order and that the second one (δ ↔ ε) is of first order. c) Close inspection of the diffraction patterns during the δ ↔ ε transition reveals co-existence of phases, in support of a first-order phase transition.*

On heating of form α, pristine and uncrushed crystals do not transform to the dark red form β directly, but *via* the intermediate metastable form γ (Fig. 3.4.5). Due to the very narrow temperature window of stability and the dependence of the transition temperature on the crystallite size and shear history, bulk amounts of this polymorph in pure state were not obtained; instead, phase γ was produced in a mixture with forms α and β. Because of the increased mosaic spread during the transition thwarted *in situ* single crystal diffraction analysis, the structure of this new phase (responsible for the jumping effect) was solved form powder diffraction data. Taken that form γ is metastable, temperature- and time-resolved XRPD was employed to monitor its behaviour (Fig. 3.4.5).

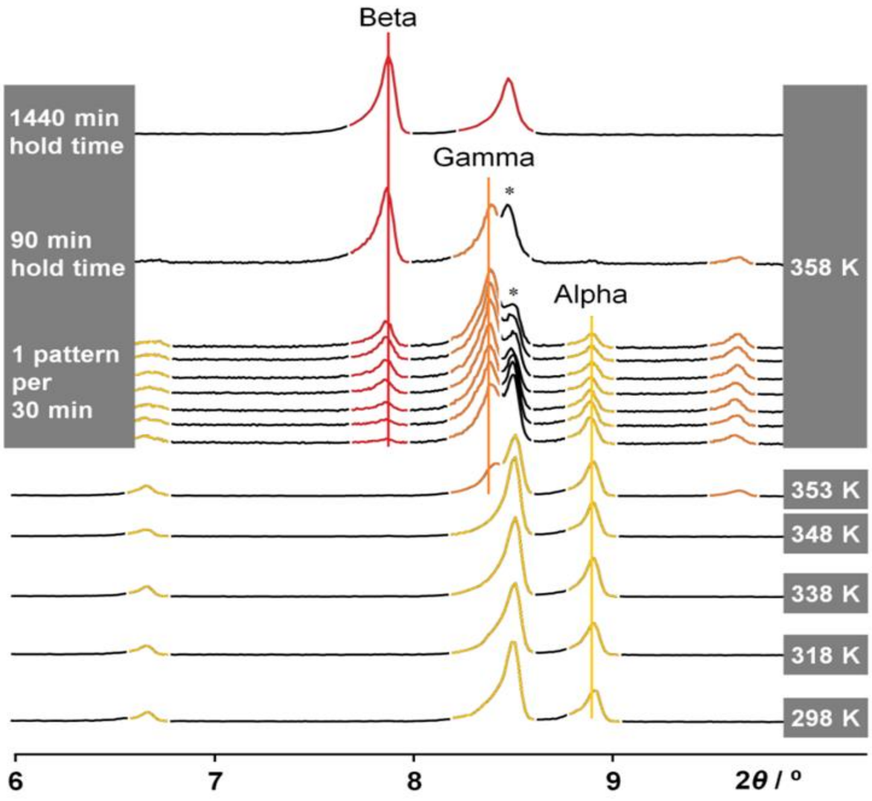

Figure 3.4.5. *Time- and temperature-resolved PXRD data of PHA.*

From 298 K to 348 K only diffraction maxima of form α are present. At 353 K the phase transition α ↔ γ takes place and the sample exists as a mixture of α and γ. At 358 K phase β starts to emerge gaining in quantity by time.

Form γ was obtained by heating form α, followed by formation of form β and producing a three-phase mixture. At higher temperatures only the β phase was detected. Interestingly, if the mixture is kept at a fix temperature of 358 K it gradually changes its phase composition: at the beginning, the amount β is increasing on the cost of the amount of α, whereas the relative amount of form γ remains constant. Later, γ also transforms into β. The very high crystallinity of the phases is a fortunate fact, which enabled collection of diffraction data for relatively short time. Thus, several subsequent diffraction patterns where the amount of γ was constant were collected. Those data were used to solve the crystal structure of this polymorph.

In order to test the influence of mechanical grinding, which creates immense local pressure, the room temperature phases were mechanically ground. Phase α immediately transformed in form β, which on grinding did not changed its structure (Fig. 3.4.6).

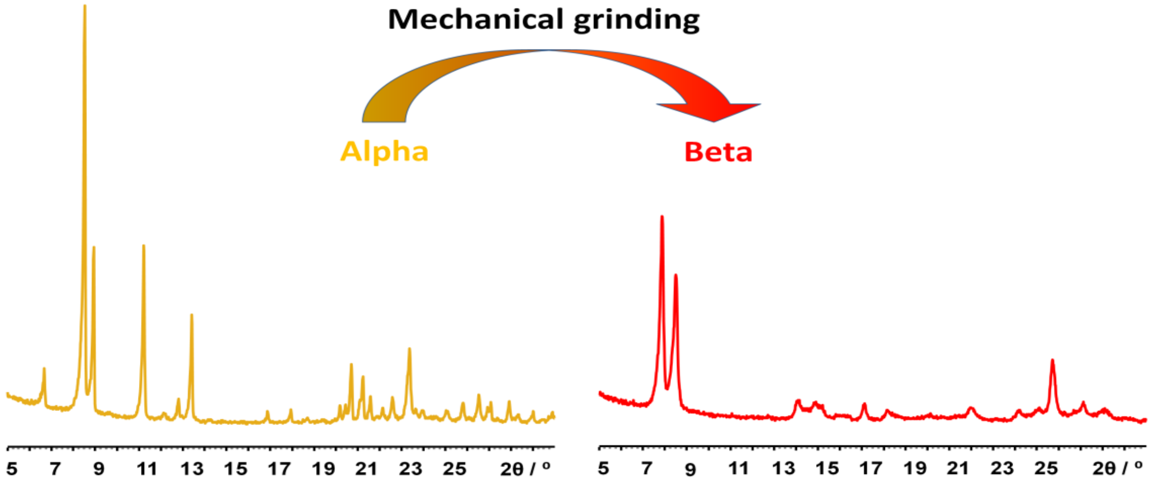

Figure 3.4.6. *Mechanochemically induced α to β phase transition.*

The α to γ phase transition was shown to be accompanied by furious jumps of crystals, whereas the rest of the phase transitions were not thermosalient, but resulted only in degradation of the single crystal integrity. The gratifying occurrence of both TS and non-TS phase transitions of PHA and the determined crystal structures of the polymorphs of PHA provides basis to firmly establish, for the first time, the mechanism of the TS effect. It is not surprising that the low temperature phase transitions are not thermosalient, taken the similarity of the crystal structures before and after the phase transitions (Fig. 3.4.7). Even after the first order phase transition, the layers of face-to-face oriented and head-to-head stacked PHA molecules in α remain the same in form ε (and probably in form δ). The extensive similarity of the room and low temperature polymorphs warrants reversibility of the process.

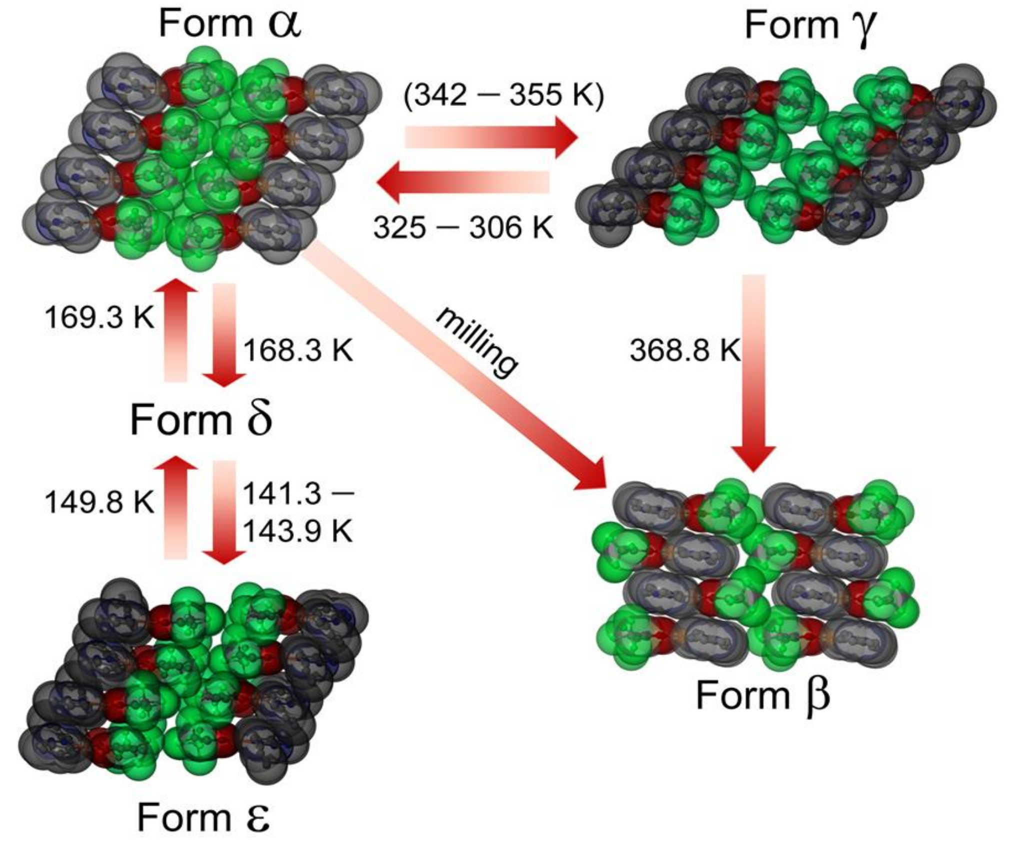

Figure 3.4.7. *Phase transitions and crystal structures of four of the five polymorphs of PHA.*

By heating of form α, its unit cell expands mainly along the *a*-axis and the molecules are getting separated one in respect to the other. Simultaneously, a rotation of the phenyl ring causes continuous changes of the packing and contraction of the *c* axis. The shear strain caused by the distortion of the unit cell is accrued to the point where it overweighs the cohesive interactions, and the structure switches to form γ. The strong coupling between the molecules results in cooperative progression of the transition even when the sample is maintained at constant temperature, as evidenced by isothermal XRPD (Fig. 3.4.5). The sharp, first-order thermosalient phase transition is characterized by high increase of the unit cell volume per molecule. The molecules have retained their head-to-head disposition within the layers, but given the increase of free space in the unit cell, the columns are separated with respect to each other to a great extent.

The crystal structure of form β is significantly different compared to that of form α. The head-to-head aligned molecules in α rearrange to head-to-tail disposition in β (Fig. 3.4.7 and Fig. 3.4.8). Based on the crystal structures, we conclude that the fragmentation during this transition is rooted in strong structural perturbation that is unsustainable to the crystal. Such molecular inter-digitation is not anticipated *a priori*, because 180^{o} in-plane rotation of individual PHA molecules is clearly not viable in the solid state. Instead, by invoking the least motion pathway within the topochemical postulate, a mechanism where the inter-digitation occurs by sliding in opposite directions of alternating layers of PHA molecules is envisaged. It can be assumed that this characteristic of the structure makes form β the thermodynamically most stable form. A comparison of the α, β and γ crystal structures is given in Fig. 3.4.8.

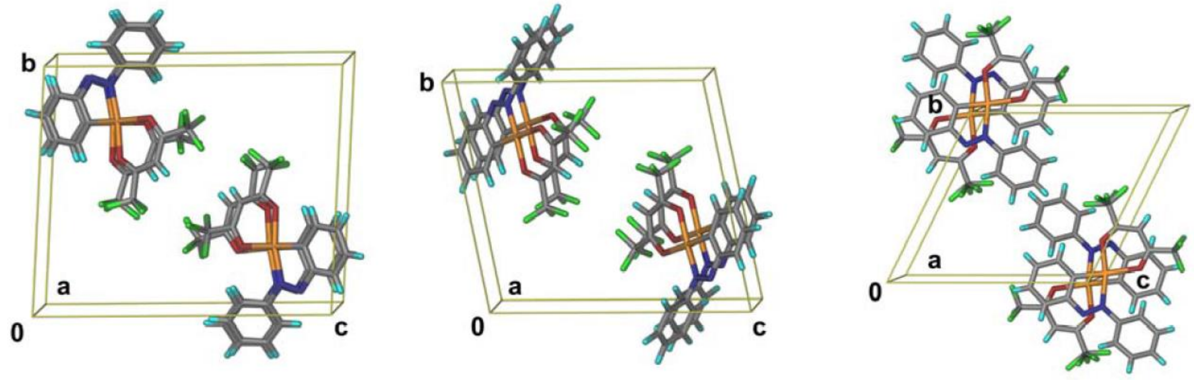

Figure 3.4.8. *Crystal packings of α, γ and β polymorphs of PHA.*

The thermal expansion of the solid forms of PHA was monitored by variable-temperature XRPD (Fig. 3.4.9). The lattice parameters were obtained by Pawley fitting of the diffraction patterns. The coefficients of the lattice thermal expansion were calculated using the following expression having linear and quadratic terms (the large uncertainty of the quadratic term, as well as visual inspection, indicates that the expansion is predominantly linear):

$$p(\mathrm{T}) = p_0(1 + \alpha_p(\mathrm{T} - \mathrm{T}_0)(1 + \alpha'_p(\mathrm{T} - \mathrm{T}_0))$$

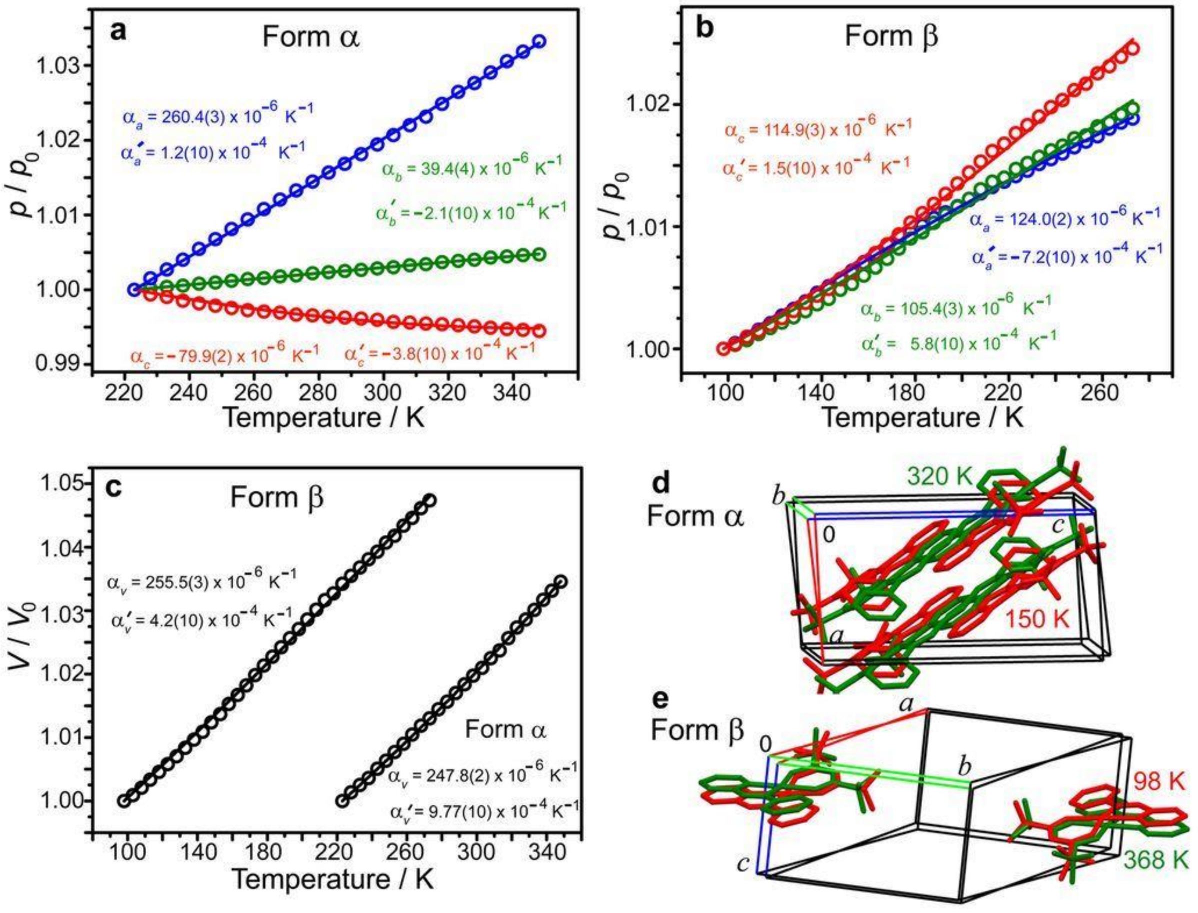

Figure 3.4.9. *a) Biaxial PTE and uniaxial NTE of α on heating from 223 K to 348 K. b) Axial PTE of β on heating from 98 K to 273 K. c) Volumetric PTE of form α and form β. d) Crystal structures of form α at 150 K (red) and 320 K (green), and e) of form β at 98 K (red) and 368 K (green) (Note that unit cell of β is scaled to be comparable to the one of α).*

The expansion of form α was studied in the thermal window between the transition α → δ (193 K on cooling and 223 K on heating) and α → γ at 348 K. Polymorph β, generated *in situ* by heating of α, was studied above the temperature of the irreversible γ → β transition (368 K) to 98 K. As shown in Fig. 3.4.9, form α undergoes exceedingly large thermal expansion; between 223 K and 348 K the *a*-axis expands as much as 4.81%, giving positive thermal expansion (PTE) coefficient α_a = 260.4(3) × 10^{-6} K^{-1}. The expansion along *b*-axis, α_b = 39.4(4) × 10^{-6} K^{-1}, is higher but comparable to the values that are typically observed with molecular solids

(0×10^{-6} $\text{K}^{-1} < \alpha < 20 \times 10^{-6}$ K^{-1}). The PTE along the *a*-axis is compensated by a considerably large negative thermal expansion along the *c*-axis, with $\alpha_c = –79.9(2) \times 10^{-6}$ K^{-1}. Although the biaxial PTE is partially compensated by uniaxial NTE, the bulk volume thermal expansion is still exceptionally large, $\alpha_V = 247.8(2) \times 10^{-6}$ K^{-1}. On the contrary, all axes of form β having outstandingly large PTE coefficients, $\alpha_a = 124.0(2) \times 10^{-6}$ K^{-1}, $\alpha_b = 105.4(3) \times 10^{-6}$ K^{-1} and $\alpha_c = 114.9(3) \times 10^{-6}$ K^{-1}. Similar to form α, the rather isotropic expansion of form β results in volume expansion of $\alpha_V = 255.5(3) \times 10^{-6}$ K^{-1}, one of the largest volume expansions reported thus far. The volumetric and some axial thermal expansion coefficients of the PHA polymorphs are higher than the coefficients that are deemed colossal and observed with $\text{Ag}_3[\text{Co(CN)}_6]$ ($\alpha_V = 160 \times 10^{-6}$ K^{-1}, $\alpha_a = 150 \times 10^{-6}$ K^{-1} and $\alpha_c = –130 \times 10^{-6}$ K^{-1}), and comparable to those of a MOF material under vacuum ($\alpha_V = 300 \times 10^{-6}$ K^{-1}, $\alpha_a = 230 \times 10^{-6}$ K^{-1} and $\alpha_c = –170 \times 10^{-6}$ K^{-1}), and of (S,S)-octa-3,5-diyn-2,7-diol ($\alpha_V = 47 – 241 \times 10^{-6}$ K^{-1}, $\alpha_a = 515 – 156 \times 10^{-6}$ K^{-1}, $\alpha_b = –85 – –63 \times 10^{-6}$ K^{-1} and $\alpha_c = –204 – –45 \times 10^{-6}$ K^{-1}). (3)

3.4.3 Conclusions

In summary, crystals of PHA exhibit a multitude of extraordinary phenomena which were revealed by using time- and temperature-resolved, *in situ* X-ray powder diffraction. The impressive crystal motility is instigated by a first-order TS phase transition in the phase α and is preceded by a colossal expansion along the *a*-axis, strong expansion along the *b*-axis and negative expansion along the *c* axis. On a molecular scale, the TS transition is due to small, displacive, diffusionless, distortive structural perturbation, where the PHA molecules slide atop each other. The internal strain that develops in response to the strong thermal anisotropy drives two phase transitions above and two phase transitions below ambient temperature. The TS-active structure is soft and remarkably susceptible to internal strain. In a heated, non-pressed crystal, accumulation of strain above a threshold triggers a rapid, self-perpetuated transformation, which causes sudden expansion along the longest axis of the crystal, whereby the crystal is fiercely propelled.

3.4.4 Experimental Section

Instrumentation

High-resolution XRPD were collected on a laboratory powder diffractometer Stoe Stadi-P with Cu$K\alpha_1$ radiation from primary Ge(111)-Johannson-type monochromator and Dectris-MYTHEN 1K strip PSD with an opening angle of 12° in 2θ, in Debye-Scherrer geometry. For the temperature-resolved measurements, hot/cold air blower (Oxford Cryosystems) was used for temperature control and data were collected at every 5 degrees, with exposition time of 5 min.

For more detailed refinement of the crystal structures solved from powder diffraction data, forms gamma and epsilon, high-resolution powder patterns were collected at the European Synchrotron Radiation Facility (ESRF) at the ID31 High-Resolution Powder Diffraction Beamline with wavelength of 0.40000 Å using crystal analyzer detector, at 358K and 90K, respectively. The respective patterns are given in Fig. 3.4.11 and Fig. 3.4.12 and the details are given in Table 3.4.1.

Sample Purity and Preparation

The low temperature polymorph, ε, and the high temperature polymorph, γ, were obtained by *in situ* cooling and heating of form α, respectively. Prior to measurement the samples were manually powdered in a mortar and pestle and sealed in borosilicate glass capillaries of 0.5 mm diameter (Hilgenberg glass No. 50). The samples were spun during data collection for better particle statistics. Epsilon was obtained in a phase pure sample. In all of the heating trials, gamma was produced in a triple mixture, together with the polymorphs alpha and beta which crystal structures were previously solved by single crystal X-ray diffraction and reported in the literature.

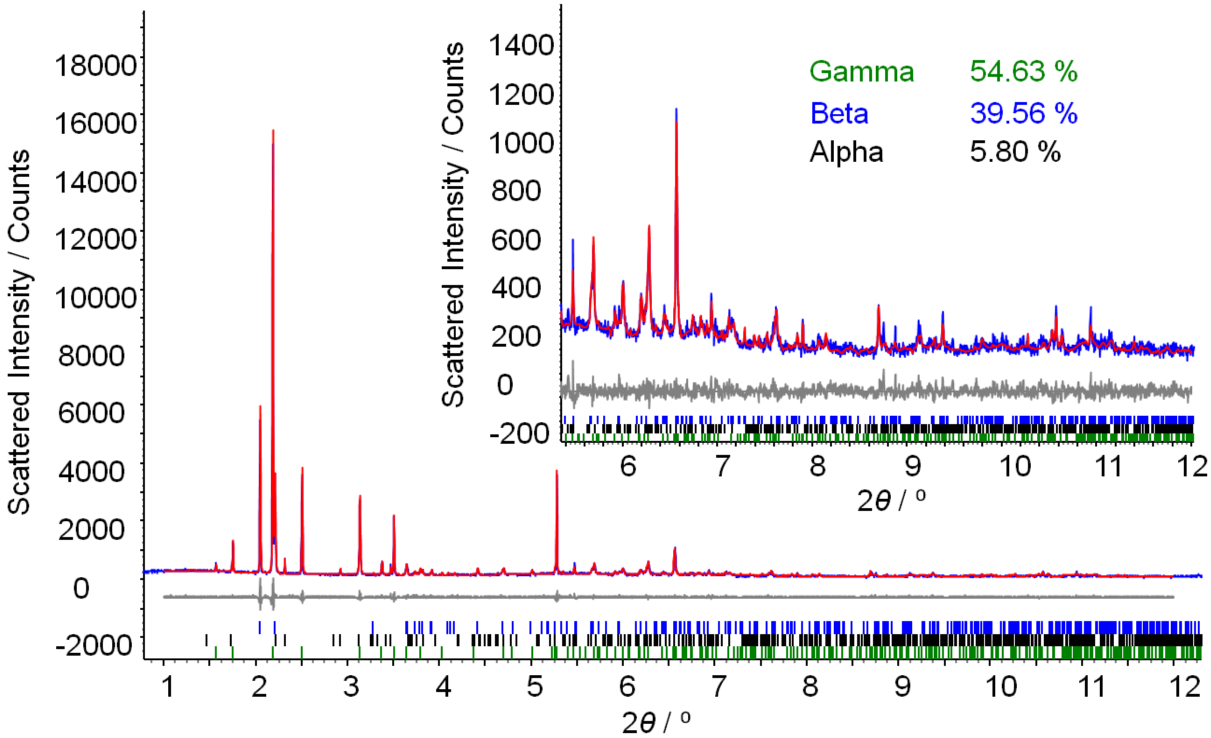

Figure 3.4.10. *Rietveld plot of PHA at 358 K. The observed pattern (blue) measured in Debye-Scherrer geometry, the best Rietveld fit profile (red) and the difference curve between the observed and the calculated profiles (gray) are shown. The Bragg reflections positions of the three present phases are given together with the ratio of the phases in the mixture.*

Structure Solution and Rietveld Refinement

The powder data analyses (pattern indexing, profile fitting, crystal structure solution and refinement) were performed with the program TOPAS 4.2. (5a) Patterns of the polymorphs with unknown crystal structures (γ and ε) were indexed with the singular value decomposition method, resulting in triclinic unit cells (*P*1 or *P*–1). Precise lattice parameters of all polymorphs were determined by Pawley fits, (5b) using the fundamental parameter approach for peak fitting, applied on each diffraction pattern collected in the studied temperature range. During the full profile decomposition the lattice parameters, stain and crystal size contributions were refined. In addition, Chebyshev polynomials were used to model the background.

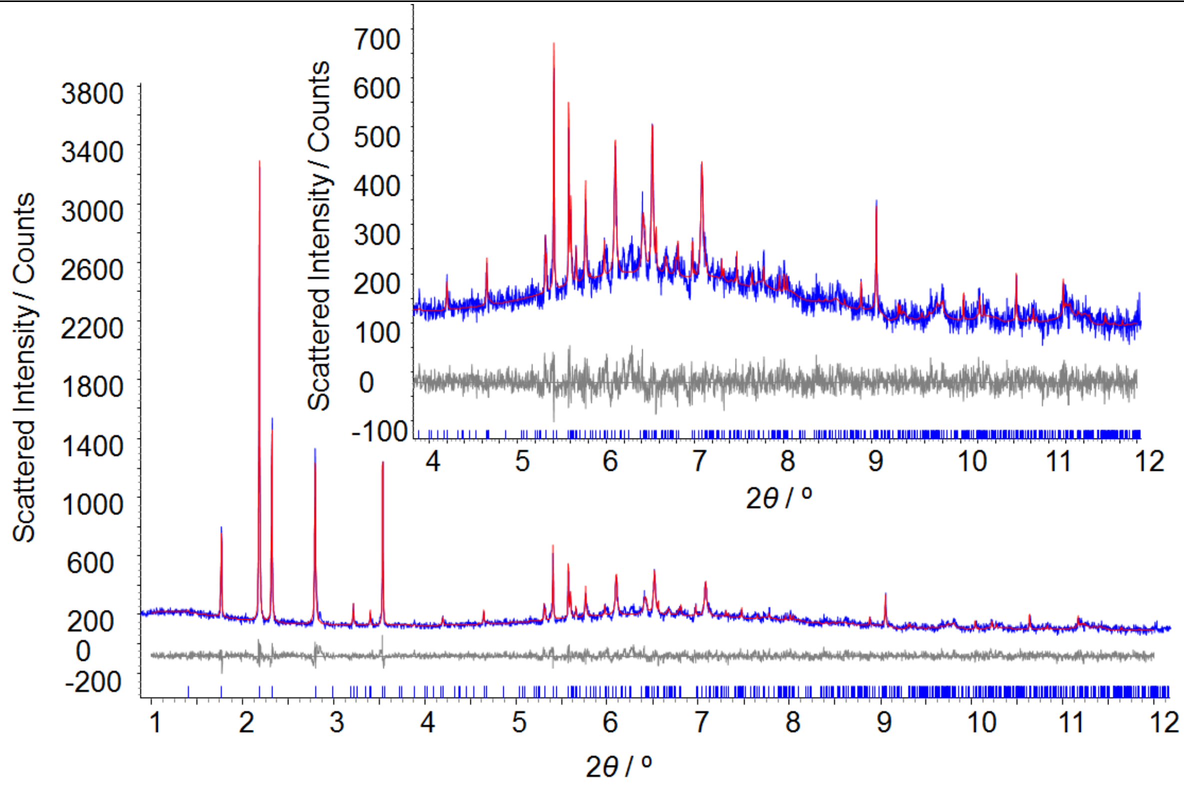

Figure 3.4.11. *Rietveld plot of PHA at 90 K. The observed pattern (blue) measured in Debye-Scherrer geometry, the best Rietveld fit profile (red) and the difference curve between the observed and the calculated profiles (gray) are shown. The Bragg reflections positions of the three present phases are given together with the ratio of the phases in the mixture.*

The crystal structures of forms γ and ε were solved by the global optimization method of simulated annealing (SA) in real space. (5c) The structure solution was performed in the *P*–1 space group using two rigid bodies for ε and one for γ in the respective asymmetric units. For the definition of the connectivity between the atoms within the rigid body of the complex the *z*-matrix notation was used. During the SA runs three rotations, three translations for each rigid body together with all possible torsion angles were set flexible. An overall temperature factor for each atom type was included in the SA process. Taken that γ was found in a mixture together with α and β, their crystal structures were included in the course of structure solution in real space with all their parameters kept fixed.

Table 3.4.1. *Crystallographic and Rietveld refinement data for PHA.*

Chemical System	Gamma	Epsilon
Sum Formula	$C_{17}H_{10}N_2O_2F_6Pd$	$C_{17}H_{10}N_2O_2F_6Pd$
Space Group, Z	P-1 (No. 2), 2	P-1 (No. 2), 2
a (Å), b (Å), c (Å)	4.2736(5), 13.5601(2), 14.8046(3)	7.7972(2), 13.2030(2), 6.4284(3)
α (°), β (°), γ (°)	83.307(8), 93.959(9), 76.843(7)	94.002(2), 87.307(3), 100.656(3)
Temperature (K)	358	90
Data collection time (h)	2	2
Wavelength (Å)	0.40000	0.40000
Start and finish angle (° 2θ)	1 and 12	1 and 12
R−Bragg (%) (a)	1.565	1.221
R–p (%) (a)	8.580	8.002
R–exp (%) (a)	1.418	2.008
R–wp (%) (a)	9.895	9.870

(a) The figures of merit are as defined in TOPAS 4.2.

Once a global minimum was found, the crystal structures were subjected to Rietveld refinement, (5d) in which bond lengths and angles of similar chemical character (e.g. aromatic, C−F bonds, C−N bonds etc.) were refined to a single joint value, together with free refinement of all profile and lattice parameters. The anisotropy of width and asymmetry of the Bragg reflections was successfully modelled by applying symmetry adapted spherical harmonics of eight's order to Gaussian, Lorentzian and exponential distributions which are then convoluted with geometrical and instrumental contributions to the final peak profile. Despite the use of capillaries in Debye-Scherrer geometry, a small amount of preferred orientation was detected and was adequately described by the use of symmetry adapted spherical harmonics. The final Rietveld plots for γ and ε, using the powder patterns collected using high-resolution synchrotron radiation, are given in Fig. 3.4.10 and Fig. 3.4.11, the refined structures of the PHA molecules in two polymorphs are presented in Figs. 3.4.12. Crystallographic details are given in Table 3.4.1.

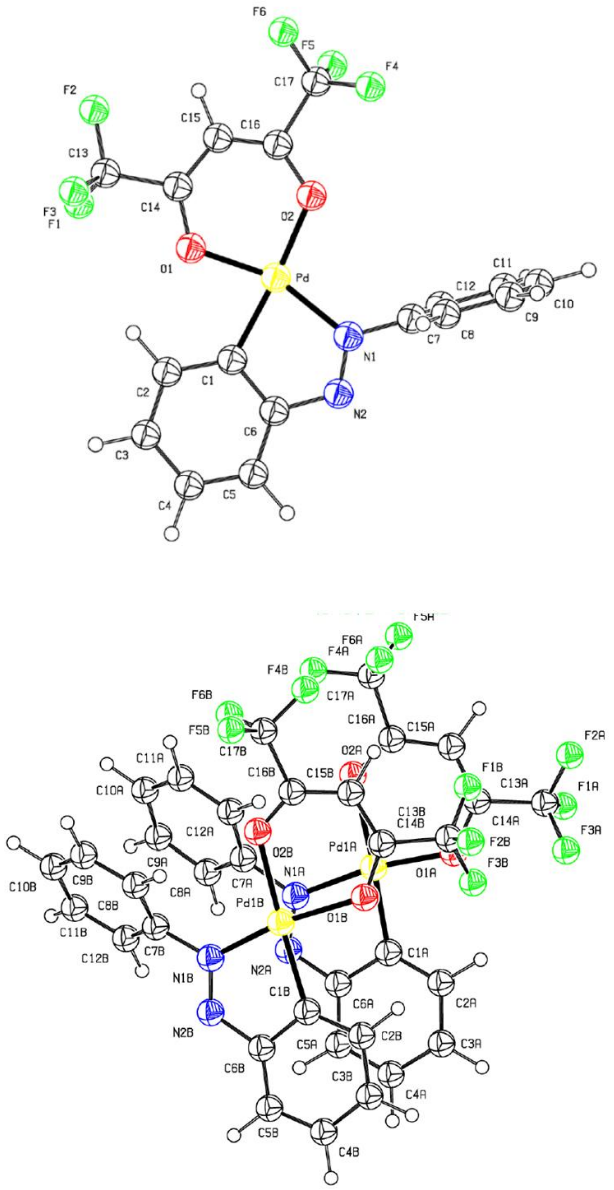

Figure 3.4.12. *Refined structures of the PHA molecules crystallized as the polymorphs gamma (up) and epsilon (down).*

References

(1) I. Burgert, P. Fratzl, *Phil. Trans. R. Soc.* 2009, **A367**, 1541; b) F. Ilievski, A. D. Mazzeo, R. F. Shepherd, X. Chen, G. M. Whitesides, *Angew. Chem. Int. Ed.* 2011, **50**, 1890; c) X. He, M. Aizenberg, O. Kuksenok, L. D. Zarzar, A. Shastri, A. C. Balazs, J. Aizenberg, *Nature* 2012, **487**, 214.

(2) a) F. Terao, M. Morimoto, M. Irie, *Angew. Chem. Int. Ed.* 2012, **51**, 901; b) D. Kitagawa, H. Nishi, S. Kobatake, *Angew. Chem. Int. Ed.* 2013, **52**, 9320; c) J. M. Blatchly, N. H. Harsthorne, *Trans. Faraday Soc.* 1966, **62**, 512; d) T. Kim, M. K. Al-Muhanna, S. D. Al-Suwaidan, R. O. Al-Kaysi, C. J. Bardeen, *Angew. Chem. Int. Ed.* 2013, **52**, 6889; e) S. Ghosh, M. C. Reddy, *Angew. Chem. Int. Ed.* 2012, **51**, 10319; f) Ž. Skoko, S. Zamir, P. Naumov, J. Bernstein, *J. Am. Chem. Soc.* 2010, **132**, 14191; g) S. C. Sahoo, M. Panda, N. K. Nath, P. Naumov, *J. Am. Chem. Soc.* 2013, **135**, 12241.

(3) a) R. S. Krishnan, R. Srinivasan, S. Devanarayanan, *Thermal expansion of crystals*, Pergamon, 1979. b) H. Birkedal, D. Schwarzenbach, P. Pattison, *Angew. Chem. Int. Ed*. 2002, **41**, 754; c) A. L. Goodwin, C. Kepert, *J. Phys. Rev*. 2005, **B71**, 140301-1; d) A. L. Goodwin, M. Calleja, M. J. Conterio, M. T. Dove, J. S. O. Evans, D. A. Keen, L. Peters, M. G. Tucker, *Science* 2008, **319**, 794; e) C. Yang, X. Wang, M. A. Omary, *Angew. Chem. Int. Ed.* 2009, **48**, 2500; f) D. Das, T. Jacobs, L. J. Barbour, *Nature Mater*. 2010, **9**, 36.

(4) Etter, M. C.; Siedle, A. R. Solid-state rearrangement of (phenylazopheny1)palladium hexafluoroacetylacetonate. J. Am. Chem. Soc. 105, 641–643 (1983).

(5) a) TOPAS version 4.2, 2007, Bruker-AXS, Karlsruhe, Germany; b) G. S. Pawley, *J. Appl. Cryst.*, 1981, **14**, 357; c) Y. G. Andreev, G. S. MacGlashan, P. G. Bruce, *Phys. Rev.*, 1997, **B55**, 12011; d) H. M. Rietveld, *J. Appl. Cryst.*, 1969, **2**, 65.

The presented work is published under the reference:

Colossal Positive and Negative Thermal Expansion and Thermosalient Effect in a Pentamorphic Organometallic Martensite

Submitted to *Nature Communications*

Manas K. Panda, Tomče Runčevski,* Subash Chandra Sahoo, Alexei A. Belik, Naba K. Nath, Robert E. Dinnebier and Panče Naumov*.

Author contributions: T. R. collected and analysed the XRPD data and solved the crystal structures, recorded and analysed the vibrational spectra (not shown in the Thesis), calculated and explained the thermal expansion coefficients. T. R. together P. N. coordinated project and wrote the article.

M. K. N., S. C. S., N. K. N. and P. N. provided the sample and performed the single crystal diffraction experiments, the kinematic analysis (not shown in the Thesis), part of the thermal analyses (not shown in the Thesis) and theoretical calculations (not shown in the Thesis), they also prepared Figs. 3.4.2, 3.4.7 and 3.4.8. A. A. B. did the low-temperature DSC measurements (not shown in the Thesis). R. E. D. monitored the work. P. N. initiated the project.

3.5. Following a Photoinduced Reconstructive Phase Transformation and its Influence on the Crystal Integrity: *In Situ* Powder Diffraction Study

In the course of organic solid state photoreactions a single crystal of a reactant can be transformed into a single crystal of a product or it can lose its crystallinity and become amorphous. In-between these two scenarios are the reconstructive phase transformations, where upon irradiation the reactant single crystal becomes powder or single crystal with strongly increased mosaicity. Herein, a detailed description of photodimerization followed by in situ XRPD is presented and the structural changes are directly correlated with the disintegration process. The kinetics of the reaction, elucidated by analysis of in situ collected diffraction data, is explained by two kinetic regimes, forming an autocatalytic-autoinhibition photoreaction set with (theoretically) 100 % quantum yield.

3.5.1 Introduction

The first report on photoinduced reactions of organic crystals dates back to the 19th century; based on the intensive research on solid state photoreactions which followed, the topochemical principle was postulated. (1) This very intuitive and exceedingly useful concept employs the necessity of minimum atomic movements and geometrical changes in constrained environments such as the crystal packing. Topotactic reactions are those in which the product forms in an oriented fashion, requiring at least some lattice points to coincide with the lattice points of the reactant. Most of these reactions are reversible and proceed in a single-crystal-to-single-crystal (SCSC) manner, which represents a promising platform for the design of photoswitches and molecular motors. (2) There are many examples, however, of irreversible photoreactions, even photoamorphisation and/or melting reaction. (3) In-between these two reaction types are the so-called reconstructive phase transformations (RPTs). When the geometrical movements during the reaction are significant (in the sense of different crystal packings, accommodated in different unit cells), the crystal cannot withstand the stress and therefore it disintegrates. The crystal disintegration and irreversibility of the reaction hamper the perspective applications of RPT systems in molecular machineries. Contrary, in terms of synthetic photochemistry, irreversible RPT reactions (often with 100 % yield) are very favorable. Thus, tuning the reaction fashion stands at the frontiers of crystal engineering. The borders between the realms of SCSC and RPT reactions are not impassable, for instance dilution of the crystal packing with a single water molecule can change the manner from RPT to SCSC. (4) In order to better understand these processes and ultimately to control them, detailed structural information, at the molecular level, before and after the photoreaction is crucial. Even if the reactant forms crystals suitable for single crystal diffraction, the disintegration with the reaction thwarts *in situ* following of the reaction and structure solution of the direct products by single crystal diffraction. Accordingly, the suitable method of choice is XRPD.

In the quest for new molecular switches, motors and actuators, nature provides useful insights, for example with the chromophores of rhodopsin, photoactive yellow protein, and green fluorescent protein (GFP). (5) The latter is well-known after its remarkable fluorescence properties and (since recently) its rich solid state chemistry. The intermediates in the synthesis of GFP derivatives, the oxazolone analogs, have been only slightly explored in terms of photoreactivity. (6) In the present work, the GFP oxazolone derivative, (*Z*)-4-(4-bromobenzylidene)-2-methyloxazol-5(4*H*)-one (*Z*-1), was synthetized according to the reaction outlined in Fig. 3.5.1a, and close attention was paid to its photoreactivity.

3.5.2. Results and Discussion

A wide range of wavelengths can be used to promote *Z*-1 photoreactivity. When it is irradiated in solution under a variety of conditions, including different solvents and light sources, *Z*-*E* photoisomerization is always found to be the main reaction mechanism (Fig. 3.5.1b). (6) However, when *Z*-1 was placed on a glass plate and irradiated at 350 nm using a photoreactor no photoisomerization was detected by NMR. Instead, a dimer (denoted as 2) as a product of [2 + 2] photocycloaddition was observed after several hours of irradiation (Fig. 3.5.1c). No photoisomer *E*-1 was detected by NMR during the whole irradiation process. Continuous irradiation for another week did not lead to any further changes in the reaction crude as observed by NMR. The resulting crude was purified by chromatography on silica gel and the product was confirmed as 2 by ^{1}H and ^{13}C-NMR and HRMS. In order to check the stability of 2, several trials were conducted with samples directly obtained from the reaction crude after irradiation. The integrity of the samples was checked after two weeks i) in dark at –30 ºC ii) in dark at room temperature (RT) iii) under ambient light at RT and iv) irradiated with a medium-pressure Hg lamp for 30 h. In all four cases the samples were exactly as the reaction crude.

All attempts to grow crystals of *Z*-1 and 2 suitable for single crystal X-ray diffraction resulted in microcrystalline powders. Therefore, the crystal structures were determined using powder diffraction data collected on high-resolution laboratory diffractometers.

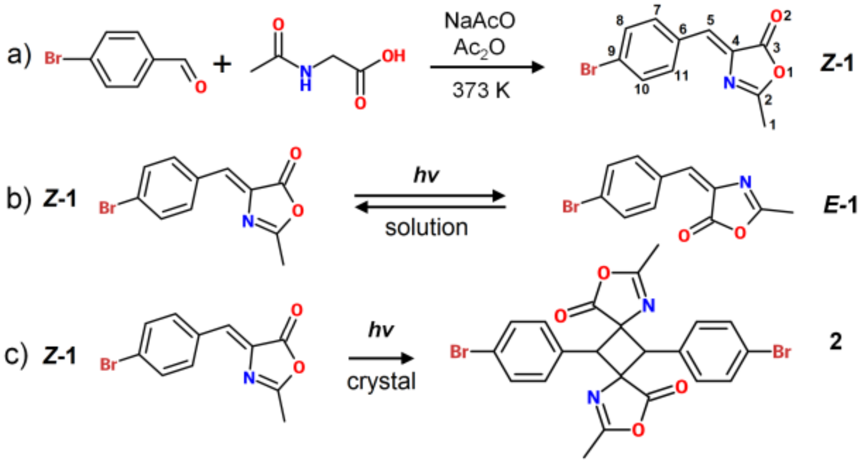

Figure 3.5.1. *a) Synthesis of Z-1. b) Photoisomerization in solution, and c) photodimerization in the solid state.*

Crystals of *Z*-1 were monitored in the course of the irreversible photoreaction with scanning electron microscopy (SEM) and XRPD. Figure 3.5.2 shows the irreversible crystal disintegration as the reaction proceeds, followed by changes of the diffraction patterns. Accordingly, the photoreaction outlined in Fig. 3.5.1c turns to be a perfect model for studying of RPT reaction in a sense of correlating the macroscopic effects on the crystals with molecular movements in the crystal structure during the reaction.

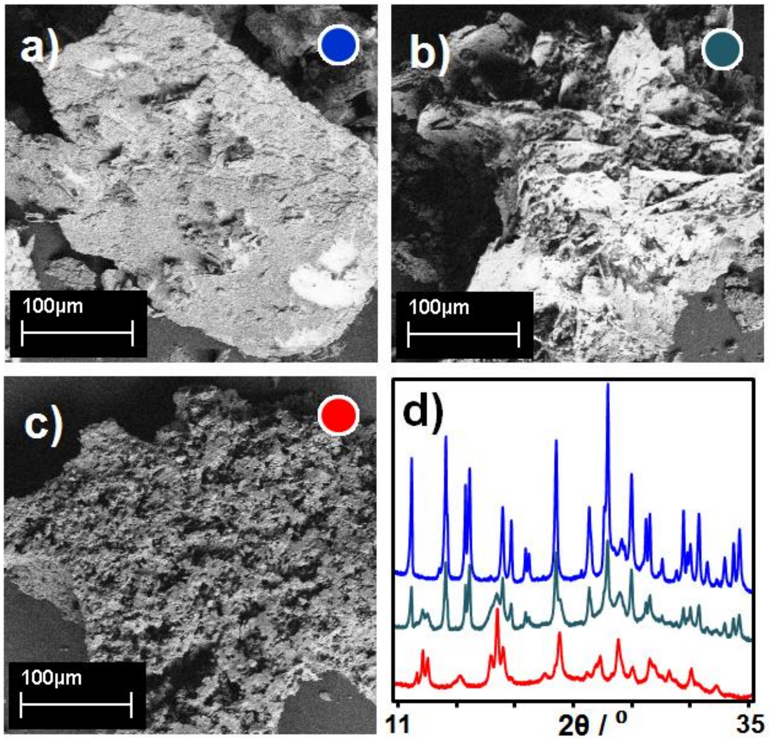

Figure 3.5.2. *SEM images of a) crystals of Z-1 before irradiation, after b) 3 days and c) 5 days irradiation. d) Respective XRPD patterns.*

Z-1 was shown to crystallize in an orthorhombic unit cell (space group $Pbc2_1$) with two molecules in the asymmetric unit (denoted A and B). The main difference between the symmetrically independent molecules was observed in the torsion angle between the two rings (N-C4-C5-C6 in A = 3.47^0 and in B = -16.66^0). The two molecules are closely head-to-tail packed, where the distances between the double bonded carbon atoms are C4A-C5B = 3.376 Å and C5A-C4B = 3.629 Å, forming pairs aligned parallel to the *a*-axis (Fig. 3.5.3a). The Hirshfeld surfaces around the C4 and C5 atoms of both molecules show intensive contacts, which together with the C-C distances smaller than 4.2 Å (the Schmidt criterion for photocycloaddition), explain the photoreactivity of *Z*-1 and formation of the dimer 2. The dimer crystallizes in the low symmetry, triclinic *P*-1 space group with half a molecule (one respective monomer) in the asymmetric unit. Figure 3.5.3b shows the necessary molecular movements of the A and B monomers in order to form the dimer molecule. The five-membered rings perform remarkable bending, whether the heavier six-membered ring is slightly rotated.

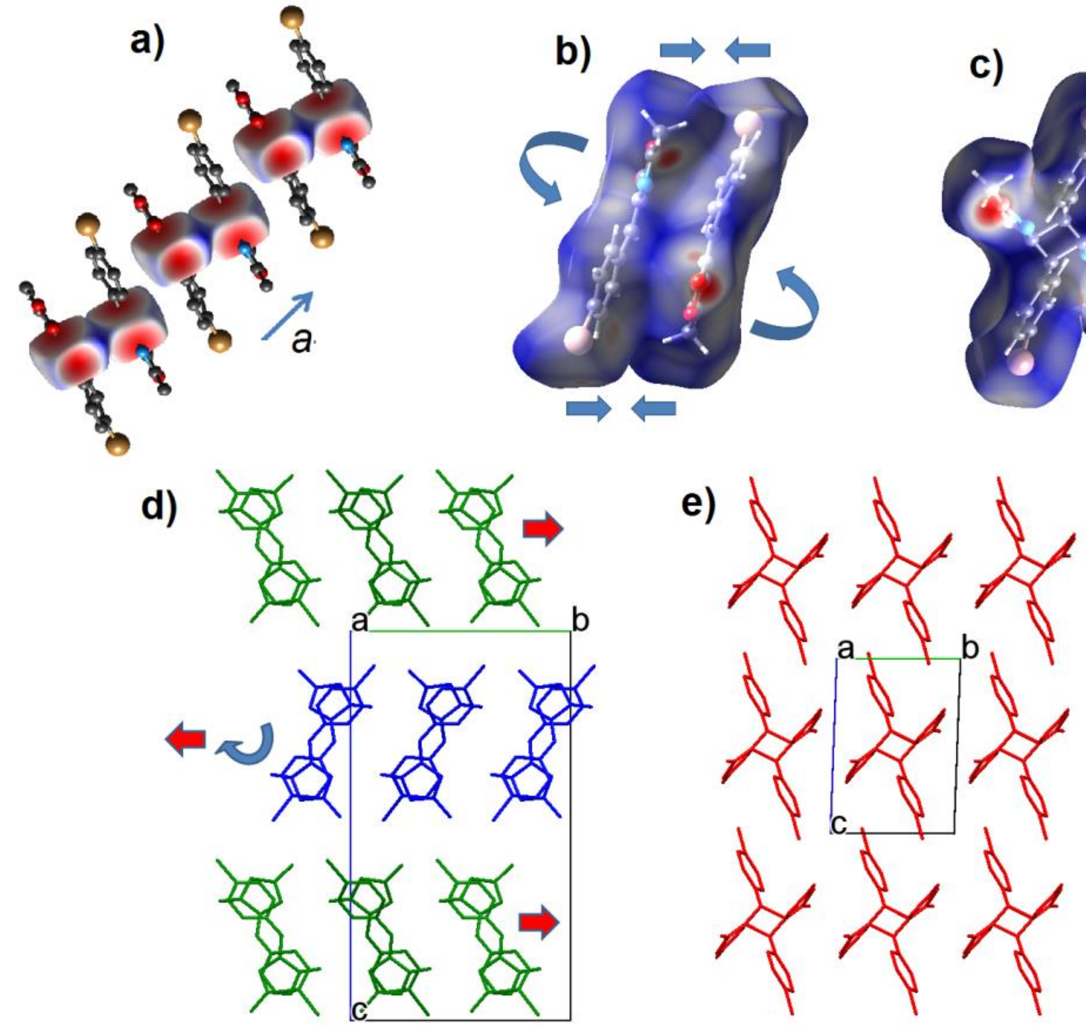

Figure 3.5.3. *a) Head-to-tail packed monomers, featuring the Hirshfeld surface around the reactive double bonds. Hirshfeld surfaces of b) the two symmetrically independent molecules in Z-1, and c) the dimer molecule in 2. Crystal packing diagrams of d) Z-1 and e) 2.*

In order to accommodate the new geometry of the dimer product, the crystal packing significantly changes. In the crystal structure of the reactant, the monomers pack forming two layers (depicted in green and blue, Fig. 3.5.3d), whether the dimers in the product's structure become ordered and only one layer is infinitely translated in space (Fig. 3.5.3e). In order this reactant-product transformation to happen in the solid state, significant molecular movements employing in-layer rotations and shifting must occur (as indicated with arrows in Fig. 3.5.3d).

Those movements in the crystal generate immense internal stress which, when released, triggers disintegration observable as cracking, increasing of mosaicity or ultimately powdering of single crystals. The results of this disintegration are visible in Figure 3.5.2. The domain size were calculated after the reaction had begun, showing that the size of the product particles indeed significantly reduces (Fig. 3.5.4).

In order to explain the nature of the solid state reaction and crystal disintegration, information on the nucleation and the subsequent growth of the product phase is needed. There are a number of cases where the kinetics of photodimerization are successfully explained using the JMAK model. (7)

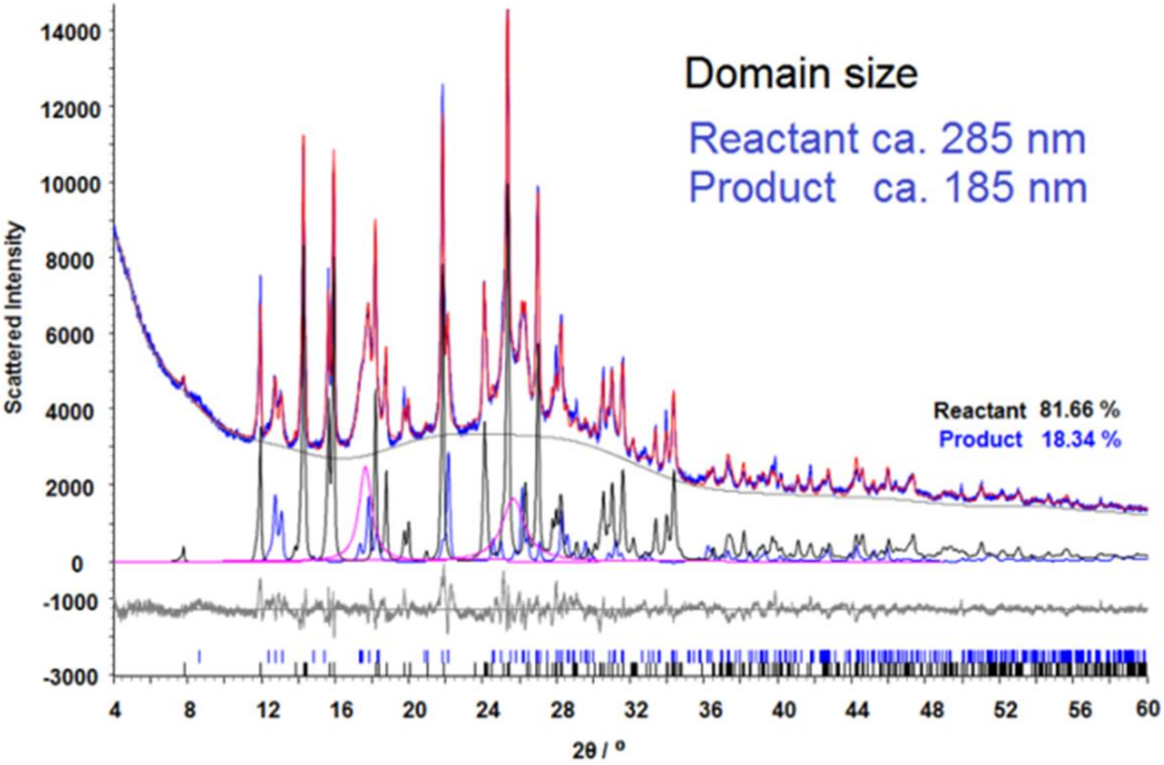

Figure 3.5.4. *Rietveld plot of partially reacted sample, where the reactant (Z-1) and the product (2) are simultaneously present. Amorphous content (magenta coloured peaks) is detected.*

The JMAK model is centered on the equation:

$$\ln(-\ln(1-x)) = n \cdot \ln(t) + n \cdot \ln(k)$$

The Sharp–Hancock is a representable plot for such a model and gives a straight line with a slope n and intercept $n \cdot \ln(k)$, where t is the collapsed time, $x(t)$ is the evolved fraction of the product phase, k (s^{-1}) is the reaction rate constant and n is the Avrami exponent. The rate constant k depends on the nucleation and growth rates and is also sensitive to temperature. The Avrami exponent represents the order of the reaction and describes the dimensionality of the growth of the product phase. It relates to the dimensionality (*dim*) of the growth of the dimer with the equation $dim = n - 1$. Interestingly, the Sharp–Hancock plot of the collected data of the *Z*-1 dimerization exhibits two different growth regimes (Fig. 3.5.5) although a single-line plot was expected. (8)

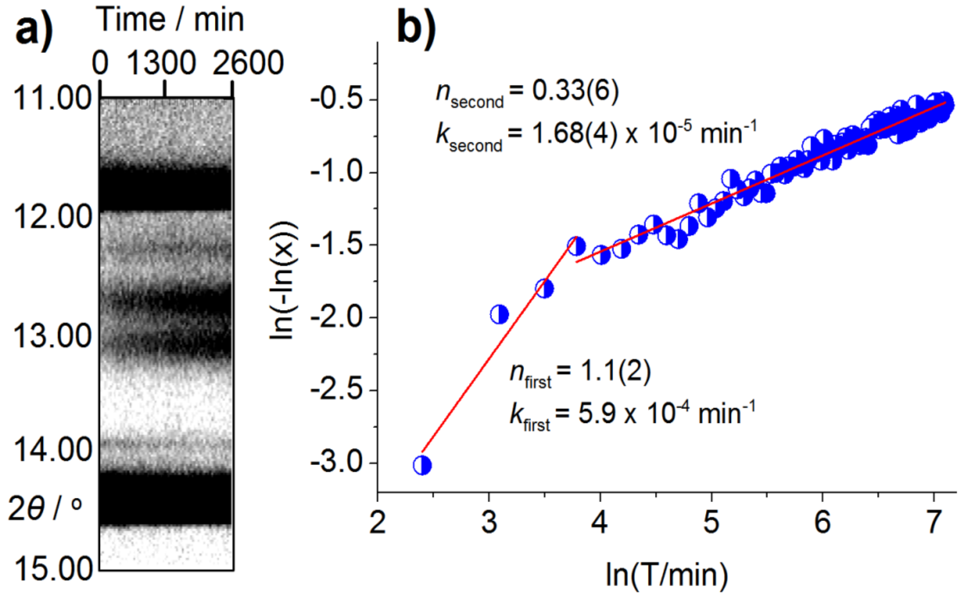

Figure 3.5.5. *a) 2D projection of the observed X-ray intensity as function of diffraction angle and time. b) Sharp-Hancock plot.*

The first regime explains the kinetic behavior at the beginning of the reaction. Owning to the fact that the time to collect the data on the experimental setup was restrained to minutes, only few points are available. Qualitative discussion on the experimental data, however, can be made. Inspecting the slope and intercept of the Sharp–Hancock plot of the first regime gives $k_{first} = 5.9(5) \cdot 10^{-4}$ min^{-1} and $n_{first} = 1.1(2)$. These values strongly indicate a fast reaction in connection with homogeneous nucleation and nearly zero dimensionality. (8) The values for the second regime are $k_{second} = 1.68(4) \cdot 10^{-5}$ min^{-1} and $n_{second} = 0.33(6)$. The dimensionality of this process has a negative value, which can be described by including a negative autocatalytic step, termed autoinhibition, as recently shown for a similar reaction. (8) It is assumed that during the first regime, dimerization of the molecules happens (indicated by the zero dimensionality and relatively fast kinetic rate) and during the second regime, significant changes of the crystal packing occur, building up strain. The strain-caused disintegration of the crystal acts as an inhibition step to the photoreaction by cracking and reducing the domain size. Therefore it influences the nucleation rate and growth of the dimer phase in the reacting matrix of the monomer phase. The fragmentation of the particles, however, enables easier penetration of photons inside the reacting crystal, making the bulk material accessible to irradiation and subsequent transformation. It can be suggested that the fragmentation leads to a fine balance between kinetics-inhibition and cracking-assisted bulk phototransformation. The interplay between the homogenous reacting first-regime (dimerization of the monomers by minimum atomic movement and geometrical changes in the crystal packing) and fragmentation-effect dominated second-regime (significant changes of the crystal packing of the dimer molecules formed during the first regime) leads to a unique photoreaction set.

3.5.3 Conclusions

To summarize, the photoirradiation of *Z*-1 proceeds *via* RPT, causing an irreversible disintegration of crystals, which was followed by *in situ* XRPD. This macroscopic event was correlated with the significant changes on the molecular level in the crystal structures before and after the reaction. Those changes create internal stress, which when released causes disintegration of crystals. The kinetics of this photodimerization reaction were explained by two kinetic regimes, corresponding to two different structural events: i) dimerization of the monomers *via* minimum atomic movement ii) changes of the crystal packing *via* in-layer rotations and shifting generating immense internal stress. These subsequent processes are forming an interesting homogeneous-nucleation – autocatalytic-autoinhibition photoreaction set characteristic for RPT resulting in crystal photo-disintegration and (theoretical) 100 % reaction quantum yield.

3.5.4 Experimental Section

Instrumentation

High-resolution XRPD patterns (Fig. 3.5.6 and 3.5.7) were collected on laboratory powder diffractometers: D8 Advance powder diffractometer [Bruker, Cu$K\alpha_1$, radiation from primary Ge(111)-Johannson-type monochromator, Våntag-1 position sensitive detector (PSD), with an opening angle of 6º] in Debye-Scherrer geometry; and Stoe Stadi-P with Cu$K\alpha_1$ radiation from primary Ge(111)-Johannson-type monochromator and Dectris-MYTHEN 1K strip PSD with an opening angle of 12º in 2θ, also in Debye-Scherrer geometry. For the kinetics experiment, XRPD patterns were collected *in situ* at each 5 minutes at room temperature, in 2θ range of 11–15°, for over than one week.

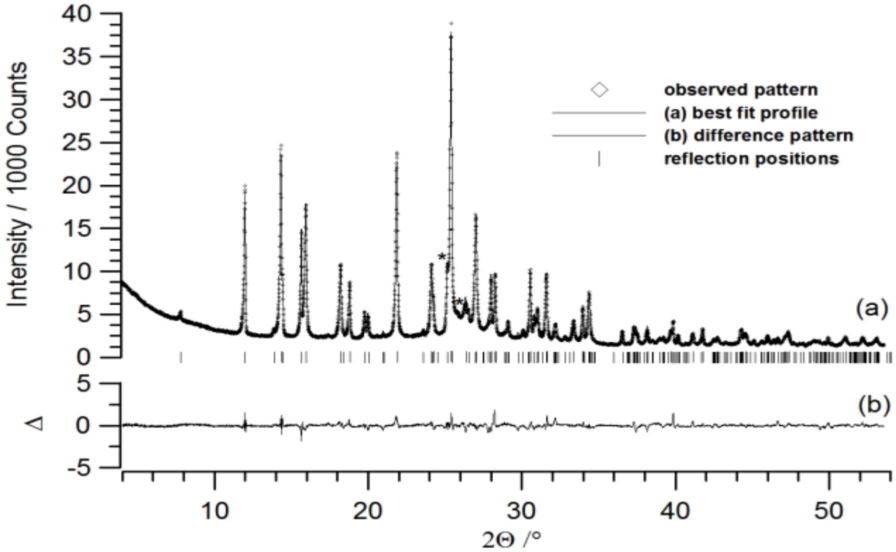

Figure 3.5.6. *Rietveld plot of the scattered X-ray intensities of the reactant Z-1 as a function of diffraction angle at ambient conditions.*

Sample Purity and Preparation

The sample of *Z*-1 was synthetized (Fig. 3.5.1a) in form of yellow powder and it was subjected to data collection without pervious treatment, except of gentle manual powdering in a pestle. The sample of the dimer was synthetized from *Z*-1 (as described in the Results and

Discussion), manually ground and measured. Both samples was sealed in a borosilicate glass capillaries of 0.5 mm diameter (Hilgenberg glass No. 50), which were spun during the measurement for better particle statistics.

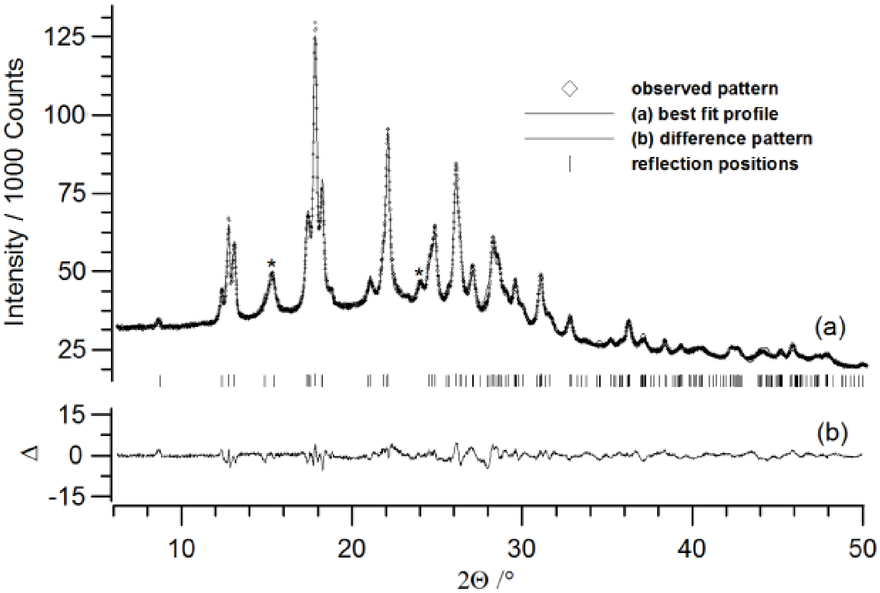

Figure 3.5.7. *Rietveld plot of the scattered X-ray intensities of the product 2 as a function of diffraction angle at ambient conditions.*

Structure Solution and Rietveld Refinement

The TOPAS 4.2 program was used for indexing, structure solution and refinement of the XRPD patterns. (9a) The indexing was performed from first principles by the iterative use of singular value decomposition, and it indicated the reactant crystallizes with orthorhombic unit cell and the product with a triclinic. The most probable space group for the reactant was found to be $Pbc2_1$. The space group of the product was found to be P–1. Precise lattice parameters were determined by a Pawley fit. (9b) The structure determination was performed by the method of Simulating Annealing. (9c) For the final Rietveld refinement, (9d) all profile and lattice parameters were subjected to free unconstrained refinement and the final plots are shown in Figa. 3.5.6 and 3.5.7. The anisotropy of width and asymmetry of the Bragg reflections was successfully modeled by applying symmetry adapted spherical harmonics of low order which are then convoluted with geometrical and instrumental contributions to the final peak profile.

Table 3.5.1. *Crystallographic and Rietveld refinement data for Z-1 and 2.*

	Reactant	Product
Molecular formula	$C_{11}H_9O_2NBr$	$C_{22}H_{16}O_4N_2Br_2$
Wavelength (Å)	1.540596	1.540596
Starting angle (º 2θ)	4.00	6.00
Final angle (º 2θ)	55.00	50.00
Data collection time (h)	24	24
Temperature (ºC)	25	25
Space group, *Z*	$Pbc2_1$, 4	*P*–1, 2
a (Å)	7.36774(21)	7.2640(16)
b (Å)	12.72997(29)	7.15366(87)
c (Å)	22.59114(63)	10.6414(17)
α (º)	90	91.3209(65)
β (º)	90	72.5124(93)
γ (º)	90	87.7580(65)
V (Å^3)	2118.850(90)	526.659(90)
R−Bragg (%) (a)	2.64	1.44
R–exp (%) (a)	1.71	0.04
R–p (%) (a)	3.67	2.17
R–wp (%) (a)	5.30	2.85

(a) The figures of merit are as defined in TOPAS 4.2.

Despite the use of capillaries in Debye-Scherrer geometry, a small amount of preferred orientation was detected and adequately described by the use of symmetry adapted spherical harmonics. The resulting improvement in the weighted profile agreement factor was on the order of 1%. The agreement factors and selected crystallographic data are listed in Table 3.5.1, the Rietveld plots are given in Figs. 3.5.6 and 3.5.7 and the refined molecular structures in the solid state in Figs. 3.5.8 and 3.5.9.

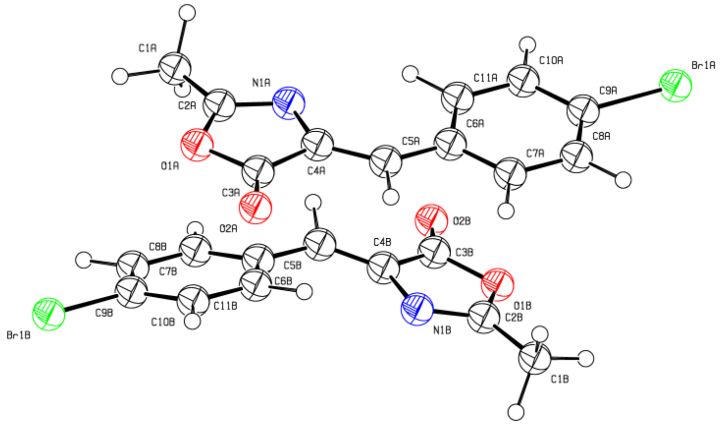

Figure 3.5.7. *Refined structure of the monomer molecules in the solid state.*

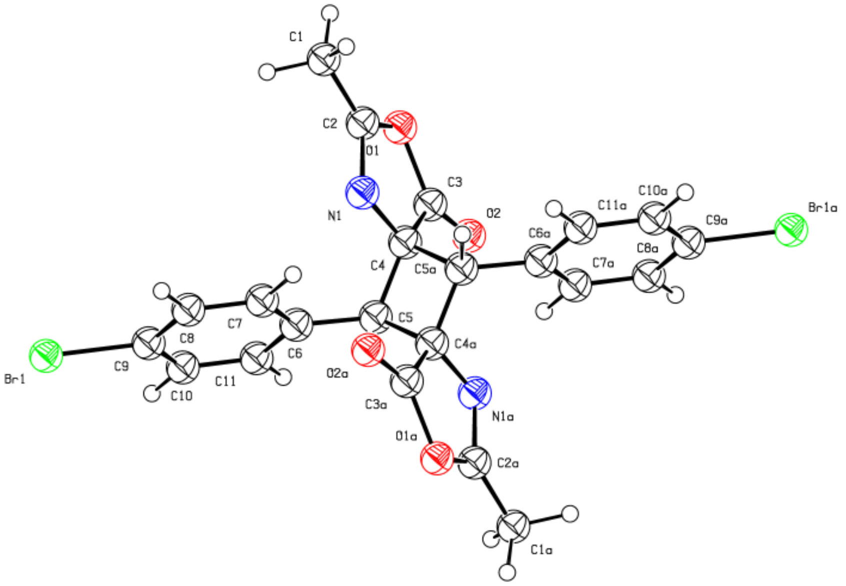

Figure 3.5.8. *Refined structures of the dimer molecule in the solid state.*

References

(1) a) S. Trommsdorff, Ann. Chem. Pharm. 1834, 11; b) M. D. Cohen, G. M. J. Schmidt, *J. Chem. Soc.* 1964, 1996; c) H. Morawetz, S. Z. Jakabhazy, J. B. Lando, J. Shafer, *Proc. Natl. Acad. Sci.* 1963, **49**, 789–793.

(2) a) S. –Y. Yang, P. Naumov, S. Fukuzumi, *J. Am. Chem. Soc.* 2009, **131**, 7247; b) S. D. Karlen, H. Reyes, R. E. Taylor, S. I. Khan, M. F. Hawthorne, M. A. Garcia-Garibay, *Proc. Natl. Acad. Sci.* 2010, **107**, 14973.

(3) a) P. Naumov, P. Makreski, G. Petruševski, T. Runčevski, G. Jovanovski, *J. Am. Chem. Soc.* 2010, **123**, 11398; b) D. de Loera, A. Stopin, M. A. Garcia-Garibay, *J. Am. Chem. Soc.* 2013, **135**, 6626.

(4) N. K. Nath, K. Manoj, A. Serban Gac, P. Naumov, *Chem. Eur. J.* 2013, **19**, 8094.

(5) a) D. Baylor, *Proc. Natl. Acad. Sci. USA* 1996, **93**, 560; b) T. E. Meyer. *Biochim. Biophys. Acta* 1985, **806**, 175; c) R. Heim, D. C. Prasher, R. Y. Tsien, *Proc. Natl. Acad. Sci. USA* 1994, **91**, 12501; d) P. Naumov, J. Kowalik, K. M. Solntsev, A. Baldridge, J. –S. Moon, C. Kranz, L. M. Tolbert, *J. Am. Chem. Soc.* 2010, **132**, 5845.

(6) a) M. Blanco-Lomas, P. J. Campos, D. Sampedro, *Org. Lett.* 2012, **14**, 4334; b) I. Funes-Ardoiz, M. Blanco-Lomas, P. J. Campos, D. Sampedro, *Tetrahedron*, 2013, **69**, 9766.

(7) a) M. Avrami, *J. Chem. Phys.* 1939, **7**, 1103; b) W. A. Johnson, P. A. Mehl, *Trans. AIME* 1939, **135**, 416; c) A. N. Kolmogorov, *Bull. Acad. Sci. USSR Phys. Ser.* 1937, **1**, 355.

(8) a) A. F. Mabied, M. Mueller, R. E. Dinnebier, S. Nozawa, M. Hoshino, A. Tomita, T. Sato, S. Adachi, *Acta Crystallog.* 2012, **B68**, 424.

(9) a) TOPAS version 4.2, 2007, Bruker-AXS, Karlsruhe, Germany; b) G. S. Pawley, *J. Appl. Cryst.*, 1981, **14**, 357; c) Y. G. Andreev, G. S. MacGlashan, P. G. Bruce, *Phys. Rev.*, 1997, **B55**, 12011; d) H. M. Rietveld, *J. Appl. Cryst.*, 1969, **2**, 65.

The presented work is published under the reference:

Following a Photoinduced Reconstructive Phase Transformation and its Influence on the Crystal Integrity: Powder Diffraction and Theoretical Study

Angewandte Chemie International Edition, accepted

Tomče Runčevski,* Marina Blanco-Lomas, Marco Marazzi, Marcos Cejuela, Diego Sampedro* and Robert E. Dinnebier.

Author contributions: T. R. initiated and coordinated the project, collected and analysed the XRPD data and solved the crystal structures, did the kinetic analysis and wrote the article together with D. S.

M. B. L., M. M., M. C. and D. S. provided the sample and performed the chemical characterizations (not shown in the Thesis) and the theoretical analyses (not shown in the Thesis). R. E. D monitored the work.

3.6. On the Remarkable Influence of Hydrogen Bonding on the Crystal Size of Codeine Phosphate Hydrates and *In Situ* Visualization of the Thermally Induced Dehydration/Polymorphism/Degradation Sequence

Codeine phosphate, a well-known active pharmaceutical ingredient, forms three hydrates and two anhydrites under experimentally different conditions. Among them, the sesquihydrate and the monohydrate are stable at room temperature (and differ in one water molecule per codeine cation). The influence of that water molecule on the internal crystal structure of their polymorphs and how that translates onto their external crystal shape is reported. An in situ diffraction study was employed to monitor the thermally induced sequence of dehydration/polymorphism/degradation.

3.6.1 Introduction

Codeine, which is a natural alkaloid extracted from the opium poppy plant, is a narcotic analgesic, antitussive and antidiarrheal active pharmaceutical ingredient with a long tradition in the treatment of many indications, such as cough, diarrhoea, mild to moderate pain and irritable bowel syndrome, among others. (1) It is listed in the WHO model list of essential medicine, and it is among the most widely used narcotic drugs. The base is frequently marketed in form of the codeine phosphate salt (COP, Fig. 3.6.1), and only two hydrates are commercially used in preparation of pharmaceutical formulations, the sesquihydrate (COP-S, 1.5 water equivalents per codeine cation) and the hemihydrate (COP-H, 0.5 water equivalents). Even though COP is an important chemical, there are many unanswered question concerning its solid state properties. Only recently, detailed IR and Raman spectroscopic and thermoanalytical studies were reported. (2) The existence of an unstable monohydrate (COP-M) on heating of COP-S was only speculated, and anhydrous forms (COP-AI and COP-AII) were suspected at high temperature.

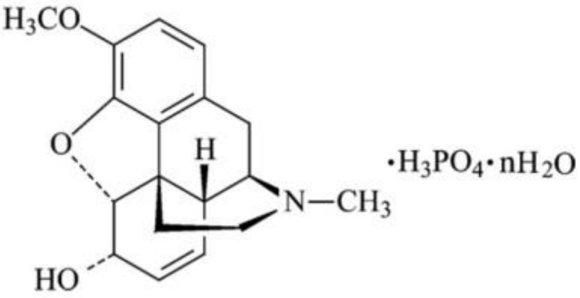

Figure 3.6.1. *Structural formula of codeine phosphate n-hydrate.*

Surprisingly, the reported crystallographic research of COPs is very scarce, with only the crystal structure of COP-H being detailed in the literature. (3) Among the reasons for the latter is the crystallization outcomes of COP, yielding single crystals of COP-H, but polycrystalline bulk of COP-S (Fig. 3.6.2). It is known that changes in the crystal structure alter the physical properties of a solid, including the crystallization behavior. (4) The crystal structures of COP-S and COP-H, however, differ only in one water molecule, and its effect on the crystallization is rather impressive. The ability of water to change the crystal structure (e.g. *via* hydrogen bonding networks) is known, (4) but the COP hydrates are an extreme example of how that translates onto the physical size, shape and stability of crystals. Moreover, when pharmaceutics are in question, the physics of a solid possibly affects a number of properties, including (but not limiting to) toxicity, bioavailability, chemical stability or shelf life. (5) Therefore, an understanding of the role of one additional water molecule in how the COP crystal grows is a desired.

3.6.2. Results and Discussion

In the course of previous studies on solid-state transformations and solvatomorphism, (2) recrystallizations of COP in different solvents lead to single crystals of COP-H and powder of COP-S. Taken the polycrystalline nature of COP-S, its crystal structure was solved using XRPD. The consecutive Rietveld refinement the solution and gave valuable information on the microstructure.

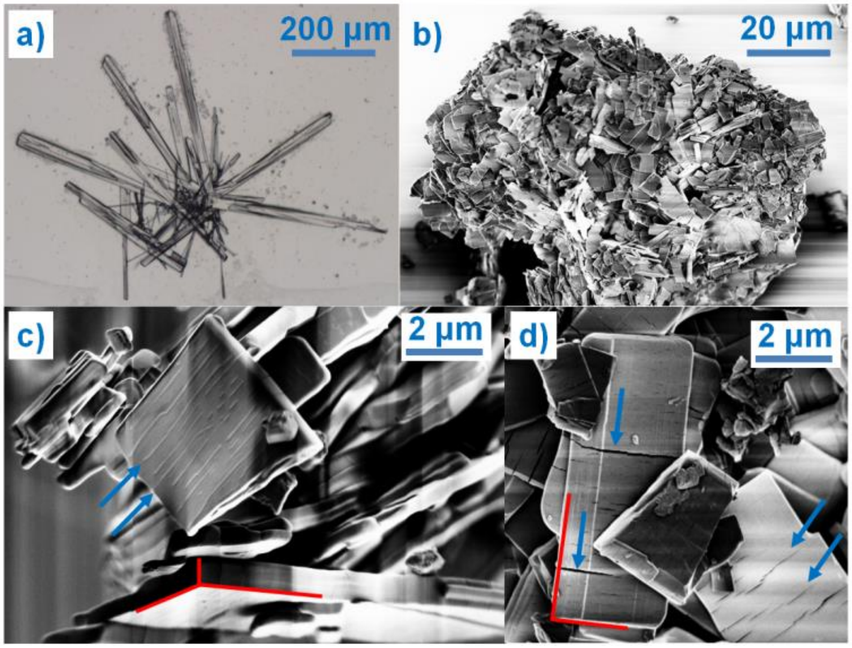

Figure 3.6.2. *a) Optical microscopy image of COP-H single crystals and b)-d) SEM images of COP-S polycrystalline particles (the red lines are guide to the eye for the microcrystals habit and the blue arrows indicate the cracks perpendicular to the largest crystal axis).*

The asymmetric unit of COP-S is composed of two codeine cations adopting the characteristic T conformation, known from related compounds of the opiate family. (3) The crystal packing of the cations is similar to the one in COP-H, as shown in Fig. 3.6.3a-d. Although both hydrates have two cations in the asymmetric unit, COP-H crystallizes in the $P2_1$ space group and COP-S in $P2_12_12_1$, thus Fig. 3.6.3b presents doubled unit cell content of the former for better comparison. The similar packing of the codeines cannot solely account for the different crystallization behavior. Irrespective of being similarly packed, however, independent codeine units are differently linked to other constituents of the asymmetric unit. In COP-H, two cations are linked together through a (codeine)-O–H···O-(codeine) hydrogen bond, employing their hydroxy and methoxy groups. The hydroxy group is additionally bonded to the water molecule and both codeine cations are bonded to the phosphate anions *via* (codeine)-N–H···O-(phosphate) hydrogen bonds (Fig. 3.6.3e).

The hydrogen bonding scheme of the COP-S codeines is the one that significantly differs. As there are two cations in the asymmetric unit, in one of them the protonated amino group and the hydroxy group are both bonded to water molecules, whereas in the other cation the same groups are bonded to the oxygen atoms of the phosphate anions (Fig. 3.6.3f). Plots of the Hirshfeld surface analyses for the two codeine cations in COP-S and COP-H are presented in Fig. 3.6.4, featuring the differences in the bonding and contacts with the surrounding constituents of the unit cell.

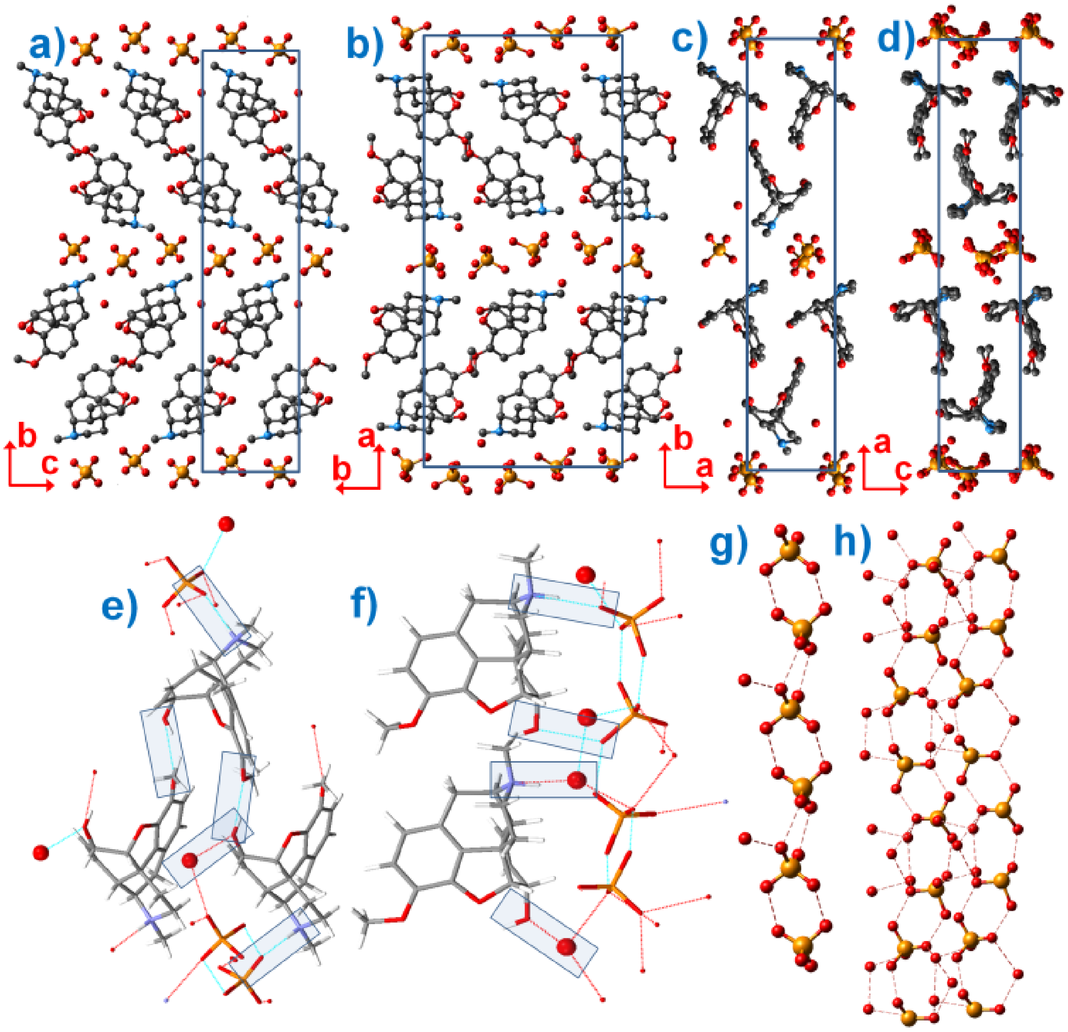

Figure 3.6.3. *Crystal packing of COP-H shown in a) and c) and COP-S in b) and d). Hydrogen bonding of the codeine cations of e) COP-H and f) COP-S. Extended hydrogen bonding network of phosphate anions and water molecules of g) COP-H and h) COP-S.*

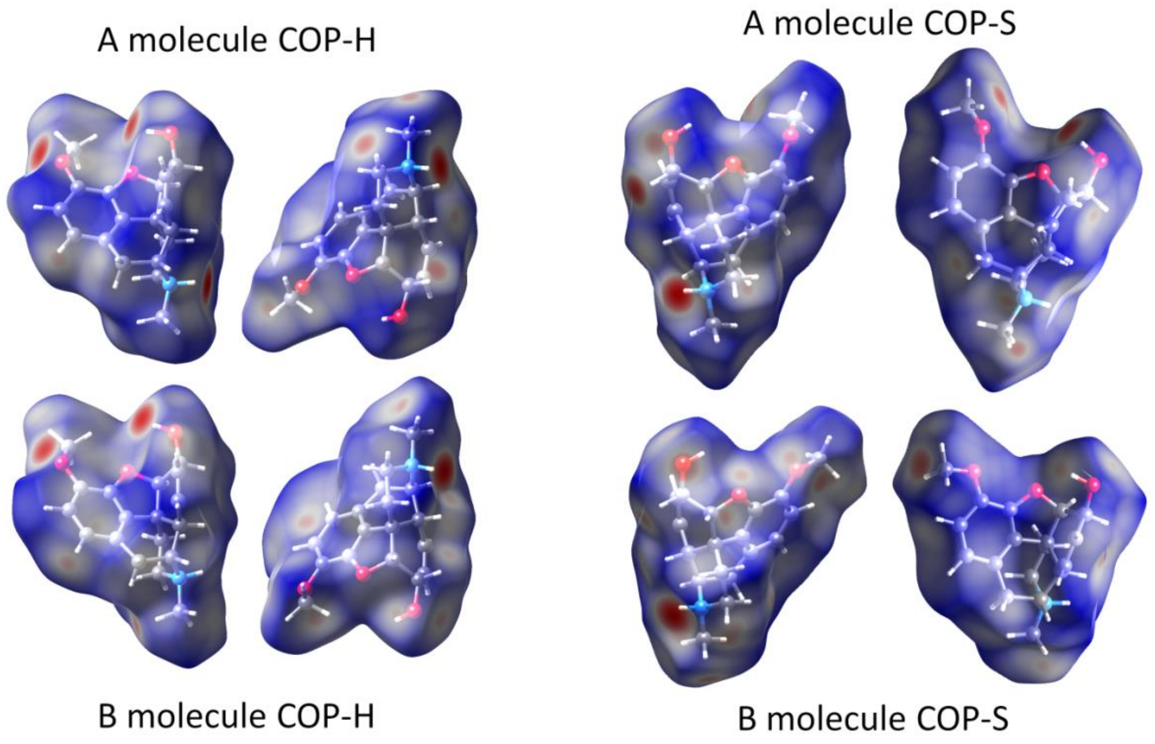

Figure 3.6.4. *Plots of the Hirshfeld surface analyses for the two codeine cations, presented in two different projections in the COP-S and COP-H structures. The red-colored surfaces indicate intermolecular bonding.*

The crucial difference within the COP-H and COP-S crystal structures is the hydrogen bonding network of the phosphate anions and water molecules. Neighboring phosphate anions of COP-H are pairwise joined together by hydrogen bonds to give an extended ribbon chain on which the water molecules and codeine cations are attached (Fig. 3.6.3g). The presence of an additional water molecule leads to a completely different hydrogen bonding scheme in COP-S, forming a complicated 2D network (Fig. 3.6.3h). The phosphate anions are pairwise joined, additionally linking water molecules, and hydroxy and protonated amino groups from the codeine cations. There are three crystallographically different water molecules in the 2D layer, two of them bonded to codeine cations and one participating solely in the phosphate-water layer.

The differences in the hydrogen bonding motives are clearly reflected in the high-frequency region of the IR spectra (4000 cm^{-1} to 2700 cm^{-1}). In the spectrum of COP-H, the mixed N–H and O–H stretching vibrations region exhibits two sharp bands (3503 cm^{-1} and 3460 cm^{-1}) and two shoulders (3540 cm^{-1} and 3401 cm^{-1}). The extensive hydrogen bonding in COP-S causes a large redshift, resulting in one broad band on which three shoulders are superimposed (~3270 cm^{-1}, 3457 cm^{-1} and 3500 cm^{-1}).

The differences in the crystal structures of COP-H and COP-S can be related to the differences in their crystallization behavior and crystal size and shape. Systematic comparison of the phosphates ribbon chain motive in COP-H with chemically related structures indicates that this simple synthon is favored in the aggregation of hydrogen phosphate anions in many single crystals. (3) With the propagation of the chain and attaching codeine cations from the surrounding solution, druses of single crystals with prismatic habit are formed. With careful evaporation of the solvent, crystals with lengths larger than 500 μm can be easily grown (Fig. 3.6.2a). COP-S, on the contrary, crystalizes in extensively cracked prismatic crystals rarely exceeding few micrometers in size (Fig. 3.6.2b-d). The Rietveld refinement indicated average domain sizes range within 0.1 and 0.15 μm. It is known that the crystal growth is heavily affected by the presence of defects in the structure, which often cause growth termination. Introducing of such defects in the simple ribbon phosphate chains in COP-H is less likely compared to the complicated 2D layered network in COP-S, where the absence and/or displacement of (e.g.) one single water molecule can severely defect the 2D layer, possibly causing growth termination. Interestingly, this 2D layer is packed perpendicularly to the largest unit cell axis (Fig. 3.6.3b,d), which possibly correlates to the cracks in the microcrystals, perpendicular to the largest crystal axis (Fig. 3.6.3c,d).

To inspect the solid-state phase transitions within COP-S and COP-H at RT, a hygroscopic study was performed. (2) The hygroscopic water sorption mass gain curve of COP-H shows ~4% mass gain, as a result of water uptake during the all-solid-phase transformation to COP-S (Fig. 3.6.5a). The ~0.4% water uptake of COP-S is attributed to surface absorption (as minimum 2% are needed to form the dihydrate). Accordingly, COP-S is found to be the most stable hydrate at RT and its stability is obviously ensured by the intense hydrogen bonding network. In the presented work, attempts were made to describe the course of the hydration phase transformation (COP-H + H_2O → COP-S) by two physical models; those are the JMAK and the Austin-Rickett (AR) formalisms (Fig. 3.6.5b). (6) Applying the JMAK model leads to a rate of reaction constant of k = 2.83(7) x 10^{-4} min^{-1} and an Avrami constant of n = 1.3(6), which is indicative for homogeneous nucleation. Fitting the curve by the AR model (preferred for diffusion-controlled reactions) gave a k value of 3.95(10) x 10^{-4} min^{-1} and a n constant of 2.1(1). The R^2 values of the curve fits by the two models are the same (0.995) and both gave comparable rate constants. The Avrami coefficients, however, differ significantly, making the elucidations of the physics of the transformation a challenging task.

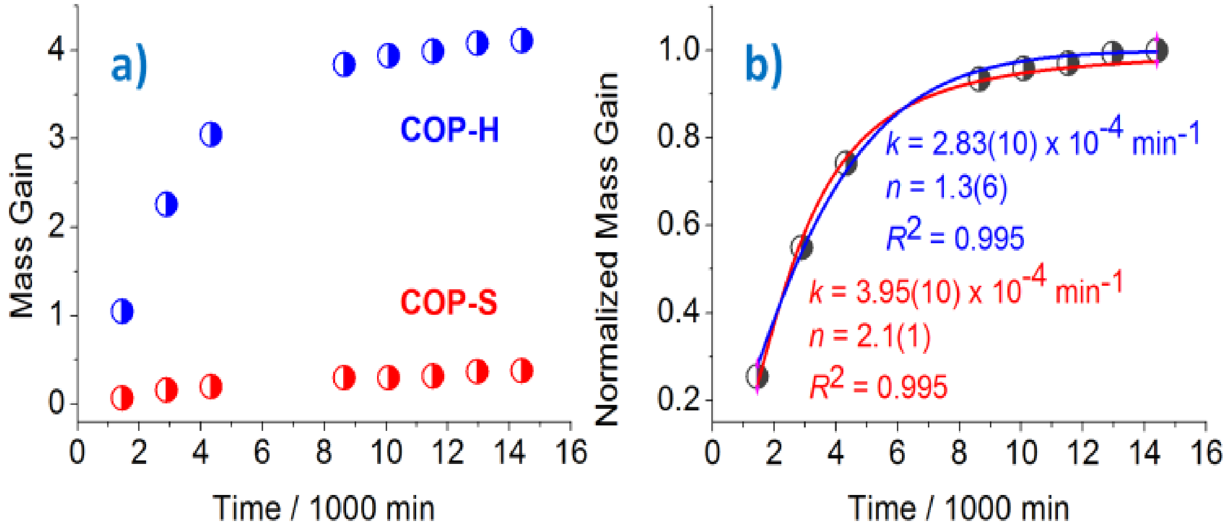

Figure 3.6.5. *a) Hygroscopic water sorption mass gain of COP-H and COP-S as a function of time. b) Explanation of the COP-H + H_2O → COP-S reaction by the JMAK equation (blue line) and the AR equation (red line).*

COP-S was proved to be the highest hydrate, with its 1.5 water molecules per codeine cation. The study of its thermally-induced process was revisited with the aim of detecting the unstable COP-M and the anhydrates, and establishing the dehydration scheme of this pharmaceutically important compound. The DSC curve, given in Fig. 3.6.6a, indicates four endothermic transitions before thermal decomposition (starting at ~240 ^{0}C, as shown by the TG and DTG curves). The second peak (or “shoulder”) visible on the DSC curve (at 99.9 ^{0}C) was not detected in the DTG and *c*-DTA analyses. To confirm that this low-energy effect is not due to an experimental mistake or an artefact, temperature-resolved XRPD data were collected *in situ* (Fig. 3.6.6b).

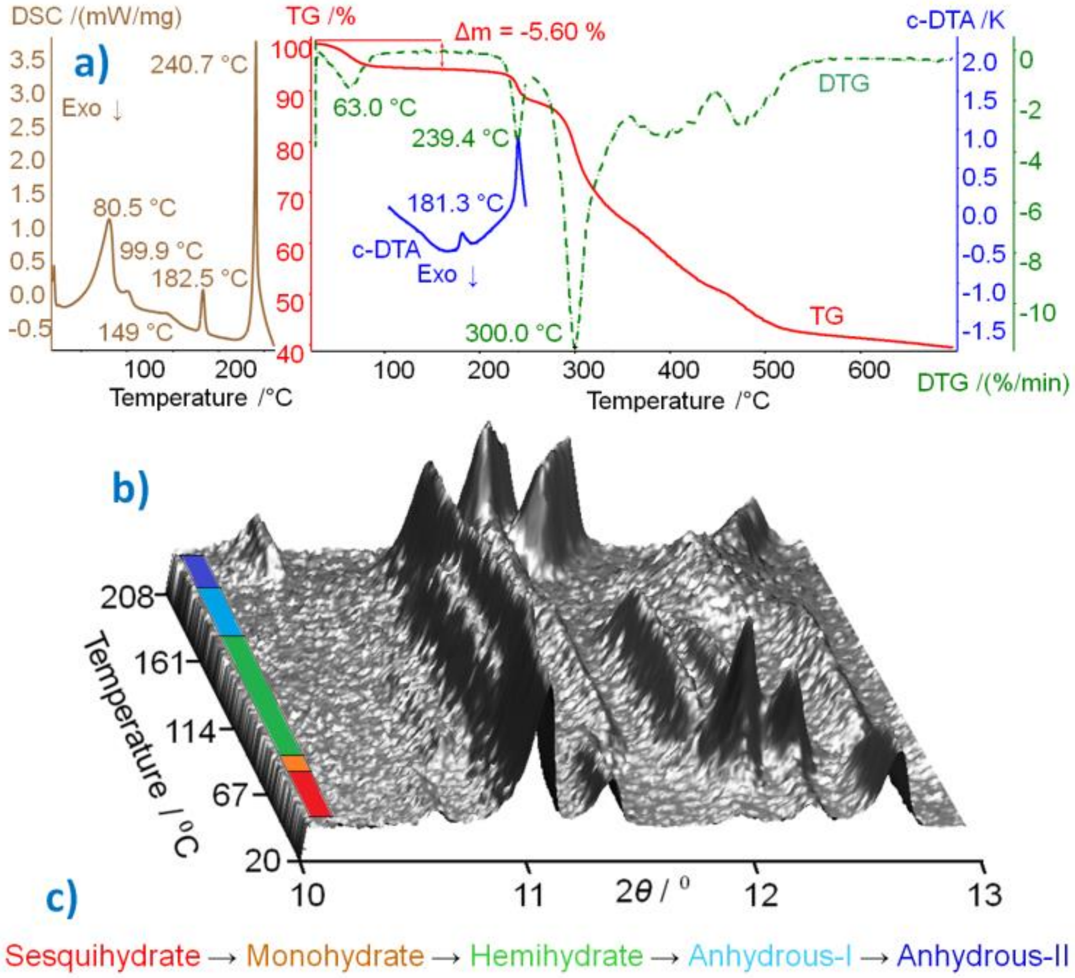

Figure 3.6.6. *a) Thermoanalytical characterization of COP-S. b) 3D projection of scattered X-ray intensity of COP-S as a function of diffraction angle and temperature, the different phases are colour coded according to the c) dehydration/polymorphism sequence.*

The changes of the scattered X-ray intensity of COP-S, as a function of diffraction angle and temperature nicely complement the DSC results, showing four transitions below 210 ^{0}C. The first three thermal effects are assigned to the dehydration sequence: COP-S → COP-M → → COP-H → COP-AI, followed by one polymorphic transition, COP-AI → COP-AII, and finally decomposition (Fig. 3.6.6c). It is an interesting observation that on heating, unlikely to all other forms, COP-AII shows large and continuous diffraction peak shifts towards higher angles, indicating significant unit cell thermal expansion.

3.6.3 Conclusions

In summary, COP crystallizes in two hydrates stable at RT, COP-S (1.5 H_2O) and COP-H (0.5 H_2O), whether their intermediate COP-M (1 H_2O) is unstable. At high temperatures, two anhydrous polymorphs are produced (COP-AI and COP-AII). The dehydration/polymorphism scheme of COP was obtained using *in situ* XRPD. The presence of 1.5 H_2O molecules (per codeine cation) leads to the thermodynamically stable form at RT. Losing 0.5 H_2O molecule per codeine equivalent results in instability but further loss of 0.5 H_2O molecule again stabilizes the crystal structure. COP-S and COP-H have similarly packed codeine cations and differ only in one water molecule per cation. Nonetheless, that single water molecule makes a huge difference in how the hydrogen bonding network is build. This detail of the crystal structure highly influences the external crystal shape and stability. COP-H forms single crystals, whether COP-S crystallizes in cracked microcrystals with domain sizes as small as 0.1 μm.

3.6.4 Experimental Section

Instrumentation

High-resolution XRPD patterns were collected on a laboratory powder diffractometer Stoe Stadi-P, with Cu$K\alpha_1$ radiation from primary Ge(111)-Johannson-type monochromator and Dectris-MYTHEN 1K strip PSD with an opening angle of 12º in 2θ, in Debye-Scherrer geometry, with data collection time of one day (Fig. 3.6.7). For the temperature-resolved measurements, hot/cold air blower (Oxford Cryosystems) was used. XRPD patterns were collected *in situ* at each degree on heating, in 2θ range of 10–13°, with data collection time of 2 min.

Sample Purity and Preparation

The commercial hydrates of codeine phosphate (hemihydrate and sesquihydrate) are routinely produced by a reaction of pure codeine with stoichiometric portions of phosphoric acid and water in ethanol solution. The sample of COP-S was carefully ground and sealed in a borosilicate glass capillary of 0.5 mm diameter (Hilgenberg glass No. 50), which was spun during the measurement for better particle statistics.

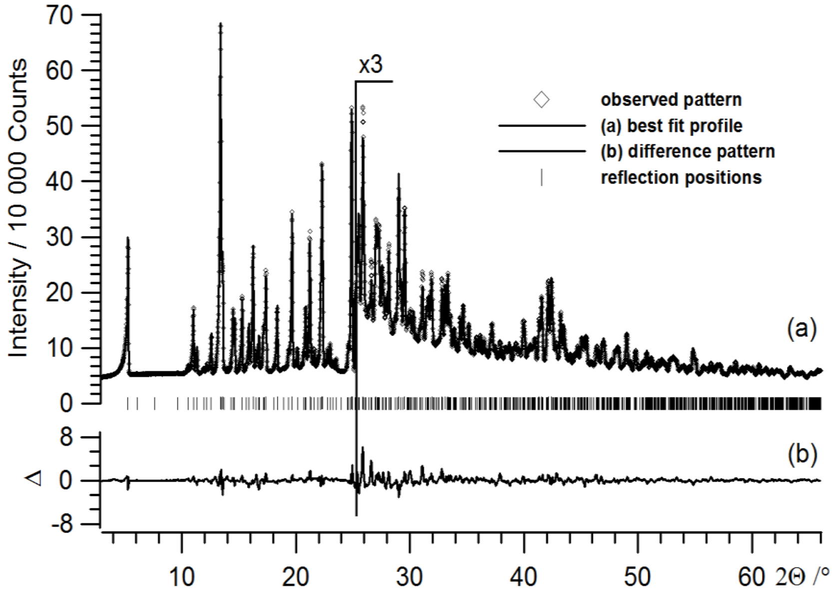

Figure 3.6.7. *Rietveld plot of the scattered X-ray intensities of COP-S as a function of diffraction angle at ambient conditions.*

Structure Solution and Rietveld Refinement

The powder data analyses (pattern indexing, profile fitting, crystal structure solution and refinement) were performed with the program TOPAS 4.2. (7a) The pattern of COP-S was indexed with the singular value decomposition method, resulting in orthorhombic unit cells (the most probable space group was found to be $P2_12_12_1$). Precise lattice parameters were determined by Pawley fit, (7b) using the fundamental parameter approach for peak fitting. During the full profile decomposition, the lattice parameters, stain and crystal size contributions were refined. In addition, Chebyshev polynomials were used to model the background.

The crystal structure of COP-S was solved by the global optimization method of simulated annealing (SA) in real space. (7c) The structure solution was performed in the $P2_12_12_1$ space group using two rigid bodies in the asymmetric unit. For definition of the connectivity between the atoms within the rigid bodies, the *z*-matrix notation was used. The rigid bodies were built based on the related crystal structure of COP-H (3). During the SA runs, three rotations, three translations for each rigid body together with all possible torsion angles were set flexible. An overall temperature factor for each atom type was included in the SA process.

Table 3.6.1. *Crystallographic and Rietveld refinement data for COP-S.*

	COP-S
Sum formula	$C_{18}H_{27}NO_{8.50}P$
Wavelength (Å)	1.540596
Starting angle (° 2θ)	4.00
Final angle (° 2θ)	65.00
Data collection time (h)	24
Temperature (°C)	25
Space group, Z	$P2_12_12_1$, 4
a (Å), b (Å), c (Å)	33.4761(7), 16.0612(3), 7.1921(2)
α (°), β (°), γ (°), V (Å^3)	90, 90, 90, 3866.95(15)
R−Bragg (%) (a)	2.25
R–exp (%) (a)	0.99
R–p (%) (a)	2.85
R–wp (%) (a)	3.48

(a) The figures of merit are as defined in TOPAS 4.2.

Once a global minimum was found, the crystal structure was subjected to Rietveld refinement. (7d) Free refinement of all profile and lattice parameters was used. Unconstrained and unrestrained refinement lead to longer P–O bonds than expected, without significant influence on the overall hydrogen bonding scheme. The anisotropy of width and asymmetry of the Bragg reflections was successfully modelled by applying symmetry adapted spherical harmonics of low order to Gaussian, Lorentzian and exponential distributions, which were then convoluted with geometrical and instrumental contributions to the final peak profile. Despite the use of capillaries in Debye-Scherrer geometry, a small amount of preferred orientation originating from the plate-like crystals was detected and was adequately described by the use of symmetry adapted spherical harmonics (affecting the R_{wp} value for less than 0.5%). The final Rietveld plot is given in Fig. 3.6.7 and plot of the molecular structure in the solid state is presented in Fig. 3.6.8.

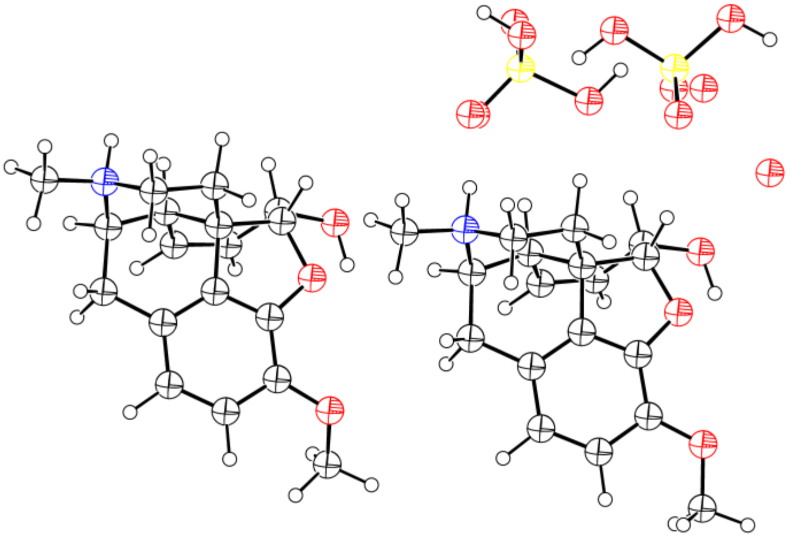

***Figure 3.6.8.** Refined structures of the COP-S molecules in the solid state.*

References

(1) a) A. J. Atkinson, H. F. Adler, A. C. Ivy, *J. Am. Med. Soc*. 1943, **121**, 646; b) N. B. Eddy, H. Friebel, K. –J. Hahn, H. Halbach, *Bull. World Health Organ.* 1968, **38**, 673; c) N. B. Eddy, H. Friebel, K. –J. Hahn, H. Halbach, *Bull. World Health Organ.* 1969, **40**, 425.

(2) a) G. Petruševski, S. Ugarkovic, P. Makreski, *J. Mol. Struct.* 2011, **993**, 328; b) G. Petruševski, M. Kajdžanoska, S. Ugarkovic, I. Micovski, G. Bogoeva-Gaceva, G. Jovanovski, P. Makreski, *Vib. Spectrosc.* 2012, **63**, 60.

(3) C. Langes, T. Gelbrich, U. J. Griesser, V. Kahlenberg, *Acta. Crystallog.* 2009, **C65**, 419.

(4) a) J. Bernstein, *Polymorphism in Molecular Crystals*, Oxford University Press, Oxford, 2002; b) G. R. Desiraju, *Angew. Chem. Int. Ed.* 1995, **34**, 2311; c) M. Wenger, J. Bernstein, *Cryst. Growth Des.* 2008, **8**, 1595; d) C. Näther, I. Jess, P. G. Jones, C.

Taouss, N. Teschmit, *Cryst. Growth Des.* 2013, **13**, 1676; e) D. Braga, F. Grepioni, L. Maini, *Chem. Commun.* 2010, **46**, 6232.

(5) a) S. R Byrn, R. R. Pfeiffer, J. G. Stowell, *Solid State Chemistry of Drugs*, SSCI Inc.: West Lafayette, 2nd ed., IN, 1999. b) S. L. Morissette, Ö. Almarsson, M. L. Peterson, J. F. Remenar, M. J. Read, A. V. Lemmo, S. Ellis, M. J. Cima, C. R. Gardner, *Adv. Drug Delivery Rev*. 2004, **56**, 275; c) N. Shan, M. J. Zaworotko, *Drug Discovery Today* 2008, **13**, 440; d) J. Chen, B. Sarma, J. M. B. Evans, A. S. Myerson, *Cryst. Growth Des.* 2011, **11**, 887; e) Ö. Almarsson, M. J. Zaworotko, *Chem. Commun*. 2004, 1889.

(6) a) M. Avrami, *J. Chem. Phys*. 1939, **7**, 1103; b) W. A. Johnson, P. A. Mehl, *Trans. AIME* 1939, **135**, 416; c) A. N. Kolmogorov, *Bull. Acad. Sci. USSR Phys. Ser.* 1937, **1**, 355; d) J. B. Austin, R. L. Rickett, *Trans. Am. Inst. Min. Eng*. 1939, **135**, 396; e) M. J. Starink, *J. Mater. Sci.* 1997, **32**, 4061.

(7) a) TOPAS version 4.2, 2007, Bruker-AXS, Karlsruhe, Germany; b) G. S. Pawley, *J. Appl. Cryst.*, 1981, **14**, 357; c) Y. G. Andreev, G. S. MacGlashan, P. G. Bruce, *Phys. Rev.*, 1997, **B55**, 12011; d) H. M. Rietveld, *J. Appl. Cryst.*, 1969, **2**, 65.

The presented work is published under the reference:

On the Hydrates of Codeine Phosphate: the Remarkable Influence of Hydrogen Bonding on the Crystal Size

Chemical Communications, accepted

Tomče Runčevski,* Gjorgji Petruševski, Petre Makreski, Sonja Ugarkovic and Robert E. Dinnebier.

Author contributions: T. R. initiated and coordinated the project, did the experimental work, analysed the XRPD data, solved the crystal structure, performed the kinetics analyses and wrote the article.

G. P. and S. U. co-initiated the project, provided the sample and performed the thermal and hygroscopic analyses, P. M. recoded the IR spectra. R. E. D. monitored the work.

The article was featured on the back cover of the journal

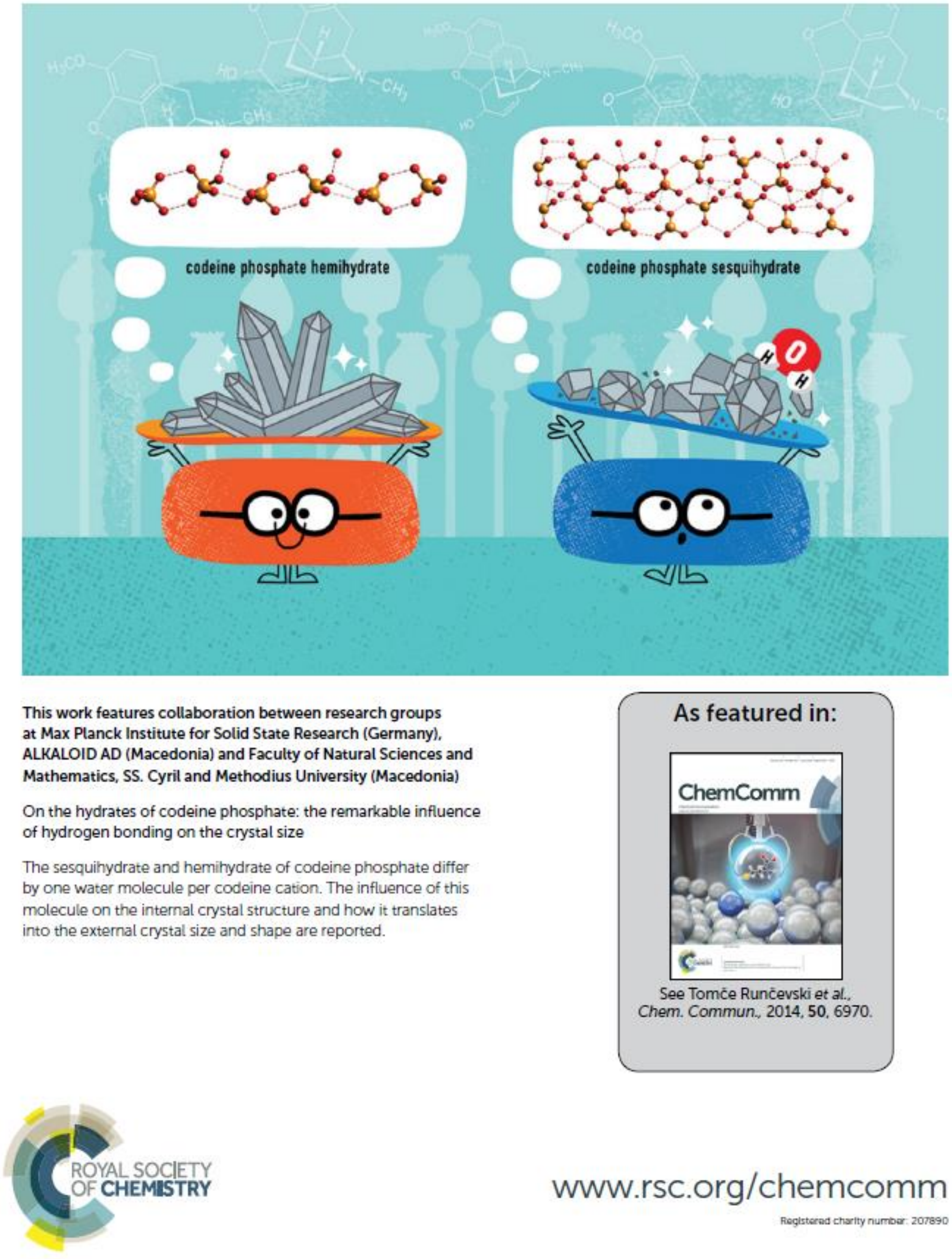

This work features collaboration between research groups at Max Planck Institute for Solid State Research (Germany), ALKALOID AD (Macedonia) and Faculty of Natural Sciences and Mathematics, SS. Cyril and Methodius University (Macedonia)

On the hydrates of codeine phosphate: the remarkable influence of hydrogen bonding on the crystal size

The sesquihydrate and hemihydrate of codeine phosphate differ by one water molecule per codeine cation. The influence of this molecule on the internal crystal structure and how it translates into the external crystal size and shape are reported.

As featured in:

See Tomče Runčevski *et al.*, *Chem. Commun.*, 2014, **50**, 6970.

www.rsc.org/chemcomm

4. Conclusions

This work demonstrates how the recent technological advances of XRPD helped to solve crystal structures of novel materials from powder diffraction data, and to observe their changes under different conditions, such as temperature, pressure, photoirradiation, etc.

The power of powder diffraction in structural studies of polycrystalline materials was recognized readily after its discovery, one century ago. Its applicability, however, was thwarted by an intrinsic problem – systematic and accidental overlap of reflections. In the second chapter of the thesis, the major developments (or milestones) of XRPD are overviewed. 1) Starting from 1940s unit present, new, advanced laboratory diffractometers and synchrotron facilities are constructed, providing collection of high-quality diffraction data. 2) The Rietveld method introduced in 1969 made the refinement of crystal structures a relatively easy task. 3) Starting from the 1990s, effective algorithms were developed and realized into user-friendly software packages, which eased the processes of crystal structure solution and refinement. Only thereafter, XRPD evolved to a very powerful method, which can be effectively used in solid state research. Moreover, powder diffraction data can be collected at ambient but also at non-ambient conditions (with varying the temperature, atmosphere, pressure, irradiation, among others), thus it can be successfully turned into an *in situ* technique – a convenient method to "see" the structure changing. Within the scope of the thesis, it is proven that this advantage of XRPD comes nicely at hand in performing state-of-the-art, frontier solid state research, and number of solid state processes were *in situ* monitored, visualized and elucidated.

From the results obtained in each of the six independent case studies presented in the third chapter, it is evidenced that various types of chemical reactions and/or physical processes can be studied in the solid state. From experimental point of view, it is concluded that close attention must be paid on how an *in situ* experiment is planned and executed. Namely, the following criteria should be met during collection of the powder patterns. 1) The time of data collection must be at the same time-scale (or preferably lower), compared to the time-scale of the chemical reaction or physical process which is studied. Therefore, high-intensity X-ray radiation is needed, as it directly translates to the scanning speed. 2) The collected diffraction data should contain sufficient amount of experimental information to reveal details of the structure, thus high-resolution data is a necessity. 3) To initiate the process or reaction, often, the samples should be placed in specially designed chambers (enabling heating/cooling, irradiation, etc.). Accordingly, high-energy radiation is crucial to permit sufficient X-rays penetration depth. As shown in the first, second and fourth case study, it can be concluded that all of these conditions are fulfilled using synchrotron X-ray radiation, having high brilliance and excellent vertical beam collimation. An important conclusion from the third, fourth, fifth and sixth case study, is that with the recent advances in X-ray radiation sources, laboratory XRPD is also a suitable choice for performing frontier *in situ* experiments, “in house”. Regardless whether a synchrotron or a laboratory source is used, a suitable and highly sensitive X-ray detector must be employed. 1D and 2D point sensitive detectors (PSDs) enable very fast and effective detection of scattered intensity, thus are great asset for an *in situ* measurement.

Vast amount of information on the solid state structure of materials can be extracted from (*in situ*) collected diffraction patterns. Firstly, from the presented 9 crystal structures, newly solved and refined from powder diffraction data, it can be stated that XRPD is a very good alternative to single crystal X-ray diffraction for elucidating the atomic scale geometrical structure of mater that crystallize (only) in form of polycrystalline bulk. Secondly, XRPD reveals the microstructure of materials, providing information of the domain size, presence of strain, stacking faults, etc. Thirdly, as it probes the bulk of the sample, rather than one single crystal, XRPD is a very suitable method for performing qualitative and quantitative structural studies on phase mixtures. Accordingly, it will not be an exaggeration to say that powder diffraction truly is among the most powerful analytical methods in solid state science, as the data collection is performed in a relatively easy and convenient way, yet at the same time it provides information on the crystal structure, microstructure and phase composition.

When data are collected *in situ* as the physical process or chemical reaction proceeds, each diffraction pattern contains information on the crystal structure, microstructure and phase composition at that particular point (on the scale of time, temperature, irradiation, among others). This information can be extensively used in gaining deeper knowledge about the systems studied. For example, in the first presented case study, processes of carbonation reactions and dehydrations were monitored and explained in details. In the second and third case, the dehydration behaviours of cementitious phases were comprehensively described and helped rationalizing the results obtained by thermoanalytical analyses. In the fourth case study, *in situ* XRPD provided crucial structural insights which enabled elucidation of the physical basis for jumping of crystals for distances thousand times of their size when taken over a phase transition. In the fifth experiment a photoinduced reconstructive phase transformation was followed and its influence on the microstructure and (single) crystal integrity was elucidated. Moreover, the photoinduced reaction rate constants were obtained directly from *in situ* XRPD, and they were correlated to the phase transitions. In the last case study, the thermally-induced dehydration/polymorphism/degradation sequence of the important pharmaceutically active ingredient, codeine phosphate hydrate, was visualized.

It is clear that nowadays (*in situ*) XRPD is a technique that still evidences continuous developments in instrumentation for scattered intensity collection, and data visualization and manipulation. It can be assumed that most of the structural studies undertaken in the scope of this thesis would have been far beyond the capabilities of the method until very recently, today they might be at the limits of performance and feasibility, but most certainty in the future they will present several more examples of routine practices. Therefore, it can be concluded that *in situ* XRPD, in the future, will inevitability take an even more significant role in revealing deeper knowledge on the solid state.

5. Zusammenfassung

Diese Arbeit demonstriert, inwieweit die technologischen Entwicklungen der letzten Jahre dazu beigetragen haben, um Kristallstrukturen neuartiger Materialien in-situ, also unter Variation externer Variablen wie Temperatur, Druck, Photonenanzahl etc., aus Röntgenbeugungsdaten an Pulvern bestimmen zu können. Bereits kurz nach ihrer Entdeckung vor einem Jahrhundert wurde das Potenzial der Röntgenpulverdiffraktometrie (XRPD) als Methode für strukturelle Studien von polykristallinem Material erkannt. Ihre Anwendbarkeit birgt jedoch ein intrinsisches Problem das in den systematischen und zufälligen Überlappungen der Beugungsreflexe besteht. Das zweite Kapitel dieser Arbeit liefert einen Überblick über die wichtigsten Entwicklungsschritte (Meilensteine) in der XRPD: 1) Seit den 1940er Jahren werden immer neuere, fortschrittlichere Labor- und Synchrotrondiffraktometer entwickelt und gebaut, welche es ermöglichen qualitativ hochwertige Beugungsdaten zu sammeln. 2) 1969 erleichterte die Einführung der Rietveld-Methode die Verfeinerung von Kristallstrukturen maßgeblich. 3) Seit den 1990er Jahre werden effektive Algorithmen entwickelt und benutzerfreundliche Softwarepakte realisiert, welche nicht nur die Verfeinerung sondern auch die Bestimmung von Kristallstrukturen aus Beugungsdaten an Pulvern ermöglichen. Erst nach diesen Fortschritten entwickelte sich die XRPD zu eine wirklich wirkungsvollen Methode, die vor allem in der Festkörperforschung ihre Anwendung findet. Darüber hinaus besteht bei diesem Verfahren die Möglichkeit Pulverbeugungsdaten sowohl bei Umgebungsbedingungen, als auch unter kontrollierten Bedingungen (zum Beispiel in Abhängigkeit von Temperatur, Atmosphäre, Druck, Bestrahlung, etc.) aufzunehmen. Durch diese kontrollierte Probenbehandlung bietet sich die XRPD als in-situ Technik an - eine geeignete Methode, um Strukturveränderungen zu "sehen".

Anhand von sechs unabhängigen Fallstudien zeigt diese Arbeit den Vorteil der in-situ XRPD Methode bei der Untersuchung von Festkörperprozessen nach dem aktuellen Stand der Technik. Die Ergebnisse, die im dritten Kapitel für jede der sechs Fallstudien aufgezeigt sind, beweisen, dass mit dieser Methode unterschiedlichste Arten von chemischen Reaktionen und/oder physikalischen Prozessen in Festkörpern untersucht werden können. Dabei ist eine sorgfältige Planung und Durchführung der in-situ Experimente von wesentlicher Bedeutung. Insbesondere die folgenden Kriterien müssen bei der Aufnahme von in-situ Pulverdiagrammen beachtet werden. 1) Die Messdauer eines Datensatzes muss im gleichen zeitlichen Rahmen (oder vorzugsweise kürzer) liegen wie die chemischen Reaktion oder der physikalische Prozesses, welcher untersucht werden soll. Hierfür ist eine Bestrahlung mit möglichst hoher Intensität nötig, da diese in direktem Zusammenhang mit der Datenaufnahmegeschwindigkeit steht. 2) Die aufgenommen Beugungsdaten sollten hochauflösend sein und möglichst wenig Überlappungen von Beugungsreflexen aufweisen, um genügend strukturelle Details für die Analyse der Kristallstruktur liefern zu können. 3) Um die zu untersuchende Reaktion oder den Prozess einzuleiten, müssen die Proben meistens in einer speziell gestalteten Kammer (mit der Möglichkeit zur Heizung/Kühlung, Bestrahlung, etc.) platziert werden. Dementsprechend ist hochenergetische Strahlung erforderlich, um eine ausreichende Durchstrahlung zu gewährleisten. Die erste, zweite und vierte Fallstudie zeigen, dass alle hier aufgeführten Kriterien durch die Verwendung von Synchrotron-Röntgenstrahlung mit hoher Brillanz und exzellenter vertikaler Strahlkollimation erfüllt werden können. Komplementär dazu wird in der dritten, vierten, fünften und sechsten Fallstudie herausgearbeitet, dass bedingt durch die jüngsten technologischen Entwicklungen, Labor-Diffraktometer ebenso im Stande sind neuartige in-situ Experimente “in-house” durchzuführen zu können. Unabhängig davon, ob eine Synchrotron- oder Laborquelle genutzt wird, muss ein geeigneter und hoch-sensitiver Röntgendetektor verwendet werden. 1D und 2D ortsemfindliche Detektoren (PSDs) erlauben eine sehr schnelle und effektive Detektion der gestreuten Intensität, weshalb diese sich für in-situ Messungen besonders anbieten.

Umfangreiche Informationsmengen über die Festkörperstruktur von Materialien können aus (in-situ) gesammelten Diffraktionsaufnahmen extrahiert werden. Zum einen verdeutlichen die Ergebnisse der neun in dieser Arbeit gelösten, verfeinerten und dargestellten Kristallstrukturen, dass XRPD eine gute Alternative zur Einkristallröntgendiffraktion darstellt. Dies ist vor allem für Materialien, welche (nur) in polykristalliner Form vorkommen, von Bedeutung, um deren Kristallstruktur auf atomarer Ebene bestimmen zu können. Zum anderen kann mittels XRPD die Mikrostruktur von Materialien untersucht werden, wobei Informationen über die Domänengröße, das Vorhandensein von inneren Spannungen, Stapelfehler, etc. gewonnen werden können. Des Weiteren stellt die XRPD im Gegensatz zur Einkristallröntgendiffraktion eine geeignete Methode dar, um qualitative und quantitative strukturelle Studien an Mischphasen durchzuführen, da XRPD die Probe als Ganzes untersucht. Ohne Übertreibung kann die Pulverdiffraktion als eine der mächtigsten Analysemethoden in der

Festkörperwissenschaft angesehen werden, da die Datenaufnahme auf relativ einfache und bequeme Art und Weise geschieht, und gleichzeitig Informationen über die Kristallstruktur, die Mikrostruktur und die Phasenkomposition erhalten werden können. Hauptanliegen dieser Arbeit ist die „state-of-the-art“ Anwendung der XRPD auf dynamische Reaktionen und Prozesse. Die in-situ Datenaufnahme währen einer chemischen Reaktion oder eines physikalischen Prozessen führt zu Beugungsdaten in denen jedes Beugungsdiagramm Informationen über die Kristallstruktur, die Mikrostruktur und die Phasenkomposition an diesem speziellen Punkt der Zeitskala (gleichbedeutend mit einer bestimmten Temperatur, Bestrahlungsstärke, etc.) enthält.

Diese Informationen sind Grundlage für die strukturelle Charakterisierung der untersuchten Systeme. Zum Beispiel werden in der ersten Fallstudie Karbonisierungsprozesse und Dehydrierungsprozesse beobachtet und im Detail erklärt. In der zweiten und dritten Studie wird das Dehydrierungsverhalten von zementartigen Phasen umfassend beschrieben. Die dabei erlangten Erkenntnisse konnten dabei mit Ergebnissen der thermoanalytische Analyse in Einklang gebracht werden. In der vierten Fallstudie liefert XRPD die entscheidenden strukturellen Informationen und die physikalischen Gründe für das Sprungverhalten von Kristallen. Dabei springen diese Kristalle über Distanzen, die das tausendfacher ihrer Größe übersteigen, sobald sie die Phasengrenze überschreiten. In der fünften Fallstudie wird eine photoinduzierte rekonstruktive Phasenumwandlung verfolgt und ihr Einfluss auf die Mikrostruktur erforscht. Überdies hinaus konnten die photoinduzierten Reaktionsratenkonstanten direkt durch in-situ XRPD bestimmt und mit den Phasenübergängen korreliert werden. In der letzten Fallstudie wird die thermisch induzierte Dehydrierung/Polymorphisierung/Degeneration von dem pharmazeutisch wichtigen Inhaltsstoff Kodeinphosphathydrat detailliert untersucht.

Im Wesentlichen ist (in-situ) XRPD eine Technik, welche einer permanenten Weiterentwicklung unterliegt, was Detektoren, Auswerteverfahren und -Software betrifft. Es kann angenommen werden, dass die meisten im Rahmen dieser Arbeit angefertigten Strukturstudien, die momentan an der Grenze des Realisierbaren liegen, in der Zukunft Beispiele der Routinepraxis darstellen werden. Es ist daher zu erwarten, dass in-situ XRPD in der Zukunft eine noch größere Rolle beim Erlangen eines tiefergehenden Verständnisses von Festkörpern spielen wird.

List of Figures

List of Tables

TOMČE RUNČEVSKI

Working Experience and Education

Postdoctoral Researcher with Prof. Robert E. Dinnebier — Aug. 2014 – Jun. 2015
Max Planck Institute for Solid State Research (Germany)

Doctoral Studies in Solid State Chemistry with Prof. Robert E. Dinnebier — Oct. 2011 – Jul. 2014
Max Planck Institute for Solid State Research (Germany) — 2 years and 10 months
PhD Dissertation at Stuttgart University, *Summa cum Laude* in Chemistry

Undergraduate and Master Studies in Applied Chemistry — Sep. 2006 – Jun. 2011
Ss. Cyril and Methodius University (Macedonia)
Including one semester at **Leipzig University** (Germany)
Bachelor of Science (2010) *Summa cum Laude* and **Master of Science** (2011) *Summa cum Laude*

Awards and Fellowships/Scholarships

Nominee for the **Otto Hahn Medal** for outstanding scientific achievements — 2014
Nominated by the Max Planck Institute for Solid State Research

Golden Medal of Ss. Cyril and Methodius for excellence in studies — 2011
Ss. Cyril and Methodius University (awarded to 20 out of ca. 10 000 students)

Award for Best Student at the Faculty of Natural Sciences and Mathematics — 2010
Ss. Cyril and Methodius University

Max Planck Institute for Solid State Research	Postdoctoral Fellowship	Aug. 2014 – Jun. 2015
International Max Planck Research School	Doctoral Scholarship	Sep. 2011 – Aug. 2014
Deutscher Akademischer Austausch Dienst	Exchange Scholarship	Sep. 2010 – Mar. 2011
Ministry of Education of Republic of Macedonia	Undergraduate Scholarship	Sep. 2004 – Jun. 2010

Research and Training

SOLID STATE CHEMISTRY, MATERIALS, CRYSTALLOGRAPHY, SPECTROSCOPY

Working experience with: metal-organic framework materials, inorganics, organics, organometallics, jumping (thermo/photosalient) crystals, photodimerisations, phase transformations, pharmaceuticals, cements and minerals, molecular magnets

Laboratory: X-ray powder diffraction (*ab initio* structure solutions and refinements), vibrational spectroscopy (infrared and Raman), reaction kinetics analyses, thermal expansion analyses, thermoanalytical methods, scanning electron microscopy, monitoring gas-loading reactions

Experiments at large scale facilities:

Diamond Light Source, Oxfordshire (UK)	1x Principal Investigator
European Synchrotron Radiation Facility, Grenoble (France)	1x Principal and 3x Co-Investigator
Deutsches Elektronen-Synchrotron, Hamburg (Germany)	1x Principal and 2x Co-Investigator
National Synchrotron Light Source - BNL, New York (USA)	1x Co-Investigator

Reviewing Activities

Crystal Engineering Communications, Current Organic Chemistry, Journal of the American Ceramic Society, Zeitschrift für Anorganische und Allgemeine Chemie, Spectrochimica Acta Part A: Molecular and Biomolecular Spectroscopy, Macedonian Journal of Chemistry and Chemical Engineering

Full List of Publications

19. *In situ X-ray Powder Diffraction*
Tomče Runčevski, Martin Etter, Robert E. Dinnebier*
Handbook of Solid State Chemistry (Eds. Dronskowski and Kikkawa) published by Wiley-VCH
In preparation

18. *On the Solid-State Structure of a Metal Organic Framework Frequently Observed on Historic Objects Made of Metal*
Robert E. Dinnebier,* **Tomče Runčevski**, Andrea Fischer, Gerhard Eggert
Inorganic Chemistry*, Submitted*

16. *Synthesis, Structure and Magnetic Properties of a Thermodynamically Metastable Thiocyanato Coordination Polymer that shows Slow Relaxations of the Magnetization*
Julia Werner, Stefan Suckert, Michał Rams, Zbigniew Tomkowicz, **Tomče Runčevski**, Robert E. Dinnebier, Christian Näther*
Inorganic Chemistry*, Submitted*

17. *Perpetually Self-Propelling Chiral Single Crystals*
Manas K. Panda, **Tomče Runčevski**,* Robert E. Dinnebier, Panče Naumov*
Journal of the American Chemical Society*, Accepted*

15. *Preparation, Structural, Thermogravimetric and Spectroscopic Study of Magnesium Potassium Arsenate Hexahydrate*
Zuldzevat Abdija, Medorija Najdoski, Violetka Koleva, **Tomče Runčevski**, Robert E. Dinnebier, Bojan Šoptrajanov, Vikotr Stefov*
Zeitschrift für Anorganische und Allgemeine Chemie*, Accepted*

14. *Colossal Positive and Negative Thermal Expansion and Thermosalient Effect in a Pentamorphic Organometallic Martensite*
Manas K. Panda, **Tomče Runčevski**,* Subash Chandra Sahoo, Alexei Belik, Naba K. Nath, Robert E. Dinnebier, Panče Naumov*
Nature Communications, DOI: 10.1038/ncomms5811, **2014**.
Highlighted by *Analytik-news, Pro-physik, Chemie, Neue Zürcher Zeitung, Max-Planck-Gesellschaft, ESRF*
Chosen as a *"Spotlight of Science" by the European Synchrotron Radiation Facility*

13. *Single Crystals Popping under UV Light: A Photosalient Effect Triggered by a [2+2] Cycloaddition Reaction*
Raghavender Medishetty, Zhaozhi Bai, Ahmad Husain, **Tomče Runčevski**, Robert E. Dinnebier, Panče Naumov,* Jagadese J. Vittal*
Angewandte Chemie International Edition, 53, 5907-5911, **2014**.
Highlighted by *Nature Middle East, Chemistry World, ScienceDaily, EEtimes Europe, Solar Daily, Wireless Design & Development, Red Orbit, E&T Magazine, Nano Werk, Science Newsline* and *Phys.org*

12. *Following a Photoinduced Reconstructive Phase Transformation and its Influence to the Crystal Integrity: Powder Diffraction and Theoretical Study*
Tomče Runčevski,* Marina Blanco-Lomas, Mario Marazzi, Marcos Cejuela, Diego Sampedro,* Robert E. Dinnebier
Angewandte Chemie International Edition, 53, 6738-6742, **2014**.
Highlighted by *Analytik-news, Pro-physik, Chemie, Max-Planck-Gesellschaft*

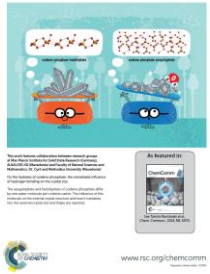

11. *On the Hydrates of Codeine Phosphate: the Remarkable Influence of Hydrogen Bonding on the Crystal Size*
Tomče Runčevski,* Gjorgji Petruševski, Petre Makreski, Sonja Ugarkovik, Robert E. Dinnebier
Chemical Communications, 50, 6970-6972, **2014**.

10. *Synthesis, Structures, Polymorphism and Magnetic Properties of Transition Metal Thiocyanato Coordination Compounds*
Susanne Wöhlert, **Tomče Runčevski**, Robert E. Dinnebier, Stefan Ebbinghaus, Christian Näther*
Crystal Growth & Design, 14, 1902-1913, **2014**.

9. *Dehydration of the Sorel cement phase $3Mg(OH)_2\cdot MgCl_2\cdot 8H_2O$ studied by in situ Synchrotron X-ray Powder Diffraction and Thermal Analyses*
Tomče Runčevski, Robert E. Dinnebier*, Daniela Freyer*
Zeitschrift für Anorganische und Allgemeine Chemie, 640, 100-105, **2014**.
Most Accessed Paper 9/2013–8/2014

8. *Synthesis, Thermal and Magnetic Properties of New Coordination Compounds based on Mn(NCS)$_2$ with 2-Chloropyrazine and 2-Methylpyrazine as neutral Co-Ligan*
Susanne Wöhlert, **Tomče Rünčevski**, Robert E. Dinnebier, Christian Näther*
Zeitschrift für Anorganische und Allgemeine Chemie, 639, 2648-2656*,* **2013**.

7. *Structural Characterization of a new Magnesium Oxysulphate Hydrate Cement Phase and its Surface Reactions with Atmospheric Carbon Dioxide*
Tomče Runčevski, Chengyou Wu,* Hongfa Yu, Bo Yang, Robert E. Dinnebier*
Journal of the American Ceramic Society*,* 96, 3609-3616*,* **2013***.*

6. *Infrared and Raman spectra of magnesium ammonium phosphate hexahydrate (struvite) and its isomorphous analogues. IX. Spectra of protiated and partially deuterated cubic magnesium caesium phosphate hexahydrate*
Viktor Stefov,* Zuldzevat Abdija, Medorija Najdoski, Violetka Koleva, Vladimir M. Petruševski,
Tomče Runčevski, Robert E. Dinnebier, Bojan Šoptrajanov
Vibrational Spectroscopy, 68, 122-128, **2013**.

5. *Dehydration of Magnesium Bromide Hexahydrate Studied by in situ X-ray Powder Diffraction*
Robert E. Dinnebier,* **Tomče Runčevski,** Kunihisa Sugimoto
Zeitschrift für Anorganische und Allgemeine Chemie, 639, 59-64, **2013**.

4. *Crystal Structures of Calcium Hemicarboaluminate and Carbonated Calcium Hemicarboaluminate from Synchrotron Powder Diffraction Data*
Tomče Runčevski, Robert E. Dinnebier,* Oxana V. Magdysyuk, Herbert Pöllmann
Acta Crystallographica Section B: Structural Science, 68, 493-500, **2012**.
Highlighted by *Anions*

3. *Minerals from Macedonia XXVI. Characterization and spectra-structure correlations for grossular and uvarovite. Raman study supported by IR spectroscopy*
Petre Makreski,* **Tomče Runčevski**, Gligor Jovanovski
Journal of Raman Spectroscopy, 42, 72-77, **2011**.

2. *Simple and Efficient Method for Detection of Rare Earth Elements in Traces by Raman Spectroscopy Instrumentation*
Petre Makreski, Gligor Jovanovski,* **Tomče Runčevski**, Radojko Jaćimović
Macedonian Journal of Chemistry and Chemical Engineering, 30, 241-250, **2011**.

1. *Visualization of a Discrete Solid-State Process with Steady-State X-ray Diffraction: Observation of Hopping of Sulfur Atoms in Single Crystals of Realgar*
Panče Naumov,* Petre Makreski, Gjorgji Petruševski, **Tomče Runčevski**, Gligor Jovanovski
Journal of the American Chemical Society, 123, 11398-11401, **2010**.